Louisiana State University

LSU Digital Commons

2014

Image-Based Pore-Scale Modeling of Inertial Flow in Porous Media and Propped Fractures

Yijie Shen
Louisiana State University and Agricultural and Mechanical College

Follow this and additional works at: https://digitalcommons.lsu.edu/gradschool_dissertations

Part of the Chemical Engineering Commons

Recommended Citation

Shen, Yijie, "Image-Based Pore-Scale Modeling of Inertial Flow in Porous Media and Propped Fractures" (2014). *LSU Doctoral Dissertations*. 1000.
https://digitalcommons.lsu.edu/gradschool_dissertations/1000

IMAGE-BASED PORE-SCALE MODELING OF INERTIAL FLOW IN POROUS MEDIA
AND PROPPED FRACTURES

A Dissertation

Submitted to the Graduate Faculty of the
Louisiana State University and
Agricultural and Mechanical College
in partial fulfillment of the
requirements for the degree of
Doctor in Philosophy

in

The Department of Chemical Engineering

by
Yijie Shen
B.S., Zhejiang University of Technology, 2008
December 2014

Acknowledgements

First of all, I would like to thank my advisor Dr. Karsten Thompson for his great patience, encouragement and support to help me grow up quickly in research work. It is not possible to finish my study without his guidance and time spending with me.

Next, I greatly appreciate Dr. Erik Thompson for providing invaluable guidance and great insights in developing finite element models. And especially thanks to Dr. Nathan Lane for his in-house code of finite element simulations and generous help in the beginning of my project. Thanks to Dr. Stephen Sears, Dr. Clinton Willson, Dr. Krishnaswamy Nandakumar and Dr. Mayank Tyagi for offering suggestions in my project. Thanks to the financial support of Exxon Mobil Upstream Research Company and Advanced Energy Consortium.

Thanks also to Paula Sanematsu for providing XCT image data and valuable help in programming and paper editing. I would also like to thank Dr. Ali Takbiri Borujeni for great collaboration in comparison of lattice-Boltzmann and finite element results. Thanks to my colleague Dr. Qiang Sheng for offering knowledge in network modeling. Also Thanks to my colleague Timothy Thibodeaux for offering help in AVIZO visualization.

To many friends I have built long term friendship in LSU, thanks my colleagues Amin, Pradeep and Tejaswini, also best friends Yajun, Nan, Bing, Fei, Dongxing, Danielle, Kezhen and Wenhao. Thanks for bringing so much fun and love in my graduate school life.

Finally, many thanks go to my parents for their unconditional love and support. I cannot imagine to finish this academic journey without their always trust and encouragement.

Table of Contents

List of Tables

List of Figures

Abstract

Non-Darcy flow is often observed near wellbores and in hydraulic fractures where relatively high velocities occur. Quantifying additional pressure drop caused by non-Darcy flow and fundamentally understanding the pore-scale inertial flow is important to oil and gas production in hydraulic fractures.

Image-based pore-scale modeling is a powerful approach to obtain macroscopic transport properties of porous media, which are traditionally obtained from experiments and understand the relationship between fluid dynamics with complex pore geometries. In image-based modeling, flow simulations are conducted based on pore structures of real porous media from X-ray computed tomographic images. Rigorous pore-scale finite element modeling using unstructured mesh is developed and implemented in proppant fractures. The macroscopic parameters permeability and non-Darcy coefficient are obtained from simulations. The inertial effects on microscopic velocity fields are also discussed.

The pore-scale network modeling of non-Darcy flow is also developed based on simulation results from rigorous model (FEM). Network modeling is an appealing approach to study porous media. Because of the approximation introduced in both pore structures and fluid dynamics, network modeling requires much smaller computational cost than rigorous model and can increase the computational domain size by orders of magnitude. The network is validated by comparing pore-scale flowrate distribution calculated from network and FEM. Throat flowrates and hydraulic conductance values in pore structures with a range of geometries are compared to assess whether network modeling can capture the shifts in flow pattern due to inertial effects. This provides insights about predicting hydraulic conductance using the tortuosity of flow paths,

which is a significant factor for inertial flow as well as other network pore and throat geometric

parameters.

1. Introduction

Transport through porous media has gained considerable attention in recent decades due to its relevance in a wide range of applications such as biological processes, water movement in geothermal reservoirs, flow in packed bed reactors, underground spreading of chemical waste, and enhanced recovery of petroleum reservoirs.

In order to understand and quantify transport processes in porous media, models for flow in porous media have been developed over many years. They occur over a vast range of length scales depending on the transport problem of interest. Two distinct length scales are used in flow modeling of porous media: the continuum scale and the pore scale. The continuum-scale approach assumes a porous material is continuous and homogeneous and macroscopic properties such as porosity, permeability and saturation are used to describe porous media. The continuum scale in porous media can range from mm to meters or kilometers in scale. In the oil and gas industry, for example, continuum scale flow models are used to predict recovery rates by numerically solving mass conservation equations with macroscopic properties over large subsurface reservoirs. Darcy's law, which describes the linear relationship between pressure drop and flow rate, is widely used in the governing equation of reservoir simulation. However, there exist some cases where Darcy's law fails to be valid because inertial effects becomes significant. Researchers have observed non-Darcy flow behavior (additional pressure drop) in many scenarios, especially in the near wellbore area of gas reservoirs and in hydraulic fractures. The Forchheimer equation is used to describe the non-Darcy flow behavior, by adding a quadratic term to Darcy's law to account for additional pressure drop. The non-Darcy coefficient in the Forchheimer equation is a parameter that quantifies non-Darcy flow behavior. Similar to permeability, the non-Darcy coefficient is a pore-structure-dependent parameter. Macroscopic

parameters such as porosity, permeability, non-Darcy coefficient are required as input for reservoir simulations. Traditionally, experiments or empirical correlations are used to obtain these properties. However, experiments are generally time-consuming and expensive, and empirical correlations are not always general enough to represent various ranges of porous media with different topologies.

Pore scale models, on the other hand, provide an alternative way to determine macroscopic parameters for input to reservoir simulations. The flow and transport process is solved in the void structure (order of micrometer or millimeter scale) of a porous media. Because permeability and the non-Darcy coefficient are ultimately affected by the pore-scale fluid dynamics, another important motivation is to fundamentally study how pore structure affects pore-scale flow behavior in addition to macroscopic properties.

The development of 3D imaging techniques as well as increasing computational capacity has opened up tremendous interest in image-based pore-scale modeling of flow in porous media. 3D imaging technology provides a detailed and accurate description of pore structures of real porous materials. The workflow for image-based pore-scale modeling involves four steps: Image acquisition, image processing (e.g. filtering and segmentation), pore-scale flow modeling and simulation and macroscopic parameter calculations.

Two different approaches are widely used in pore-scale modeling: network modeling and direct simulation. In network modeling, void structures in digital images are approximated as pores connected by throats. Pore size, pore-center location, throat radius and pore-throat connectivity are geometric information from network models to account for pore-level heterogeneity and interconnectivity in the porous media. Using network models significantly reduce the size of the image structure data; therefore network modeling is very computationally

efficient. The mass conservation equation is imposed in each pore of a network model, and the hydraulic conductance value in the mass conservation equation is approximated based on pore-throat geometries and fluid dynamics. Because of the approximations introduced in the pore geometry and hydraulic conductance, network modeling is less rigorous than direct simulation models, which are based on basic principles (e.g. the Navier-Stokes equations).

Direct simulation techniques including Lattice Boltzmann modeling (LBM) or traditional computational fluid dynamics (CFD) modeling provide a more rigorous approach but with with larger computational cost. Lattice Boltzmann modeling is a widely used method for pore-scale modeling in complex geometries. LBM directly operates on voxel grids from digital images. This, in turn, results in a direct correlation between computational cost and image resolution (higher image resolution results in more voxel grid number). There is always a tradeoff between computational cost and image resolution in LBM. Computational fluid dynamics modeling, which directly solves the Navier-Stokes equations using finite difference, finite volume or the finite element method, is a traditional approach for solving engineering problems that involve fluid flow. It is a powerful tool for engineering design and analysis, but few researchers have applied this technique to pore-scale modeling until recently. The work of this dissertation is mainly focused on finite element modeling. Since one challenge of using structured grids (e.g., directly from voxel images) is the high computational cost of high-resolution images, the finite element method offers the option of using unstructured meshes to represent the domain geometry. It is important to point out several advantages of unstructured meshing in porous media flow modeling. First, the number of elements in the unstructured mesh can be decoupled from image resolution. Multiple meshes of different refinements can be generated from the structure of a specific image resolution. The numerical accuracy of flow simulation is dependent

on mesh refinement assuming the image resolution captures the pore structure accurately. Second, unstructured meshes better conform to complex geometries and offer flexible local mesh refinement. Using multiple mesh refinement levels in the same domain allows efficient and accurate simulation. This is significant for the study of non-Darcy flow where the mesh can be refined in regions of interest that show strong inertial effects.

Understanding the pore structure effects on pore-level flow behavior and flow parameters (permeability, non-Darcy coefficient) is important in order to accurately predict non-Darcy flow. In the current pore-scale modeling efforts, simplified geometries of porous media are mostly used, which are not representative enough to capture flow behavior in the 3D real porous media. The consequence of coarsening pore space in the network modeling is that sub-pore level transport phenomena cannot be simulated, therefore a rigorous pore-scale model (direct simulation) is critical to solve the pore-level non-Darcy (inertial) flow behavior. In order to study the non-Darcy flow in real porous materials, we develop a new image-based pore-scale finite element model using unstructured meshing. This model is applied to proppant packings and propped hydraulic fractures under different loading stresses. Hydraulic fracturing is a process in which liquid mixed with proppants and chemicals is injected into wellbore at high pressure and a network of fractures are created in the rock formation to enhance the production of oil and gas. Proppants are injected because they remain in the formation to hold (or "prop") the fracture open. This technique is widely used in low permeability reservoirs to increase production rate. Hydraulic fractures are paths of high flow rate, which mean that non-Darcy flow has a significant effect on the productivity rate of these fractures. Although there are experiments reporting the effects of loading stress on fracture conductivity and non-Darcy flow coefficient as well as non-Darcy flow effects on the fracture conductivity (C. E. Cooke, 1973; Fredd, McConnell, Boney, &

England, 2001; Much & Penny, 1987), a fundamental understanding of stress effects on pore structure and flow dynamics is still unknown. Image-based pore-scale modeling provides details of the proppant structure change as a function of stress and also inertial flow behavior in different pore space geometries.

The outline of this dissertation is the following:

Chapter 2 introduces the different continuum flow regimes within laminar flow in porous media. Research work evaluating non-Darcy coefficients and non-Darcy flow behavior at the pore scale is reviewed. Background on image-based pore-scale modeling is presented, including image acquisition, image processing and numerical modeling.

In chapter 3, the method of image-based finite element modeling and network modeling is presented in detail. It includes micro-tomography X-ray image processing, unstructured mesh generation based on digital images and the solution of the governing equations. The calculation of macroscopic parameters for porous media are also presented.

Chapter 4 compares pore-scale LBM and FEM simulations of Stokes flow in random consolidated sphere packings. The accuracy of both simulations with various image resolutions is studied. The difference between these two numerical methods is discussed based on comparison of transport properties and pore-level velocity fields obtained from the simulations.

In chapter 5, image-based pore-scale FEM modeling is applied in proppant packings and propped fractures under various loading stresses to predict non-Darcy flow behavior. The loading stress effect on permeability, non-Darcy coefficient, void space geometry, and pore-level flow behavior are investigated.

In chapter 6, methods that can be used to improve network modeling of non-Darcy flow are developed and analyzed.

Chapter 7 summarizes the major conclusions of this dissertation and future work is discussed.

2. Background

2.1 Flow Regimes in Porous Media at the Macroscopic Scale

Numerous experimental and theoretical studies have been conducted on single-phase flow through porous media. Within the laminar regime, it is widely accepted that a linear Darcy flow is valid at low Reynolds number while a quadratic Forchheimer flow appears at larger Reynolds number. A cubic or weak inertial regime has been proposed to exist between the Darcy and Forchheimer regime. In addition, flow behavior beyond the Forchheimer regime has been studied (Barree & Conway, 2004). In all, four regimes exist within laminar flow: (1) Darcy regime (2) Weak inertia regime (3) Forchheimer regime (4) Beyond Forchheimer regime.

2.1.1 Darcy Regime

Darcy's law was proposed (Darcy) through a series of experiments on fluid flow through a packed gravel bed. Darcy's law is a linear relationship between flow rate and applied pressure gradient and it was formulated through this equation:

$$-\frac{dp}{dx} = \frac{\mu v}{k} \tag{2-1}$$

where $-\dfrac{dp}{dx}$ is the pressure drop across the sample, v is the superficial velocity, μ is the fluid viscosity, and k is the permeability. Permeability is a property of the structure of the porous media and it is independent of the nature of the fluid. Darcy's law has been validated by theoretically deriving the Stokes equations from volume averaging (Whitaker, 1986). Theoretically, Darcy's law is strictly valid for Stokes flow, but usually it is applicable for flow with a Reynolds number of less than one. Some experimental results show that flows with a Reynolds number higher than one is still Darcy's flow regime (Comiti, Sabiri, & Montillet,

2000; Scheidegger, 1958). Darcy's law is usually a valid assumption for flow in reservoirs and aquifers, because the combination of pressure gradient, fluid viscosity, and permeability.

2.1.2 Weak Inertia Regime

As velocity increases, a nonlinear deviation from Darcy's law begins to occur. Numerical simulations (Hill, Koch, & Ladd, 2001) and theoretical analyses (Mei & Auriault, 1991) have shown that the cubic law that occurs at the onset of nonlinear behavior is formulated as:

$$-\frac{dp}{dx} = \frac{\mu v}{k} + \frac{\gamma \rho^2}{\mu} v^3 \qquad (2\text{-}2)$$

It only appears as a narrow flow regime in the velocity beyond the Darcy regime and is termed as the weak inertia regime. It is important to point out that most of the numerical simulations which prove the existence of cubic law are performed in 2D periodic porous media. Fourar, Radilla, Lenormand, and Moyne (2004) present numerical simulation results in both 2D and 3D periodic porous media and conclude that this weak inertia regime in 3D-flow is not significant compared to 2D-flow, so it can be ignored in practical cases.

2.1.3 Non-Darcy (Forchheimer) Regime

With further increase in flow velocity, inertial effects become more important and the nonlinear deviation between pressure drop and flow rate is more significant. This phenomenon is often observed in hydraulic fractures and near the wellbore of gas reservoirs. Forchheimer (1901) discovered from experiments while flowing gas through a coal bed that the relationship between pressure gradient and flow rate is non-linear at sufficiently high velocity. He proposed an equation by adding a quadratic term to Darcy's equation:

$$-\frac{dp}{dx} = \frac{\mu v}{k} + \rho \beta v^2 \qquad (2\text{-}3)$$

where β is referred as the non-Darcy coefficient. The quadratic term is small compared to the linear term at low velocities and Darcy's law is still valid. The Forchheimer equation is generally considered to be a good description of non-Darcy flow in 3D-flow and many researchers have theoretically derived the Forchheimer equation from the Navier-Stokes equations using averaging theorem (Ruth & Ma, 1992) and homogenization (Marušić-Paloka & Mikelić, 2000). Different opinions existed about the source of non-Darcy effects. Hassanizadeh and Gray (1987) explained that interfacial viscous drag forces were the source of this nonlinearity. However, Ma and Ruth (1993) argued that microscopic inertial forces leaded to distorted velocity and pressure fields with the consequence of non-Darcy effects.

2.1.4   Beyond Forchheimer Regime

This regime is referred to as an unsteady laminar regime, the transition regime from the laminar flow to turbulent flow regimes. Local experimental measurement within the pore space, to detect flow fluctuations, has been used to determine the upper limit of the Forchheimer regime. The onset of fluctuations usually happens at a Reynolds number around 100 in packed bed (Jolls & Hanratty, 1966). Few researchers have studied the flow behavior in this regime. Barree and Conway (2004) proposed that velocity fluctuation can cause a permeability plateau at high Reynolds number, and Huang and Ayoub (2008) showed that the Forchheimer equation is still valid in this regime but the permeability and non-Darcy coefficient is different than in the Forchheimer regime.

2.2   Non-Darcy Flow

Non-Darcy flow has been a popular subject in the oil and gas industry. In subsurface applications such as oil and gas production or groundwater transport, the vast majority of a domain can be governed by Darcy flow. However, the regions where inertial flow occurs can

have a disproportionate effect on the system behavior. One example is the near-wellbore region, where radial flow patterns can increase the fluid velocity significantly, and where most of pressure loss occurs. A second example is in hydraulic fractures, which are held open by proppant and are designed to carry high flowrates of oil or gas toward the wellbore. Understanding and predicting flow in propped fractures has taken on extra importance in recent years due to the increased use of hydraulic fracturing in both conventional and unconventional oil and gas operations. Quantifying the additional pressure drop caused by non-Darcy effects is part of this overall problem, especially as it can have adverse effects on production.

Many research works have demonstrated the significant reduction on production rate caused by non-Darcy effects. Friedel and Voigt (2006) predicted cumulative productions of fractured wells in tight-gas reservoir from reservoir simulators and showed that the production was reduced by as much as 33% when considering non-Darcy flow effects. Mohan, Pope, and Sharma (2009) showed the production of gas condensate in the Darcy flow regime was 10 to 100 times higher than in the non-Darcy flow regime. Vincent, Pearson, and John (1999) also demonstrated the significant overestimation of production rate from deep gas wells, shallow gas wells, moderate depth oil wells and lower rate oil wells, caused by disregarding non-Darcy effects.

One aspect of this problem is optimal fracture design and proppant selection. Handren et al. (2001) compared production rates of lightweight ceramic proppants (LWC), resin coated sand proppants (RCS) and sand proppants using the Darcy flow model and little difference was shown. However, numerical flow modeling that included non-Darcy effects indicated that LWC proppants led to significantly increased production rates compared to sand and RCS proppants. Lopez-Hernandez, Valko, and Pham (2004) illustrated that the non-Darcy flow coefficient was

critical to calculate the optimum fracture width and length. An optimal fracture geometry design helped to reduce the additional pressure drops caused by non-Darcy effects. Both of these studies proved that fracture designs and proppant selections including non-Darcy effects increased the production rates up to 30% compared to the design based on the Darcy flow model.

Non-Darcy effects also impact well testing in fractured systems. Alvarez, Holditch, and McVay (2002) showed effects of analyzing pressure build up and draw down test data without considering non-Darcy effects, which resulted in wrong estimation of fracture conductivity and fracture half-length. Umnuayponwiwat, Ozkan, Pearson, and Vincent (2000) showed that using traditional pressure transient analysis neglecting non-Darcy flow leads to errors of up to 78% and 54% in the fracture conductivity and half-length.

2.2.1 Non-Darcy Coefficient

In the Forchheimer equation, the non-Darcy coefficient β quantifies the extent of deviation from the Darcy's flow regime. Similar to the permeability, non-Darcy coefficient is a property related to porous media structures. For the calculation of β, the Forchheimer equation is rearranged as follows:

$$\frac{\Delta p}{L\mu v} = \frac{1}{k_{app}} = \frac{1}{k} + \beta(\frac{\rho v}{\mu}) \tag{2-4}$$

The value of β and k are calculated from a linear regression of a plot of $1/k_{app}$ versus $\rho v/\mu$ in the Forchheimer flow regime. The fit has a slope β and intercept $1/k$. Based on this regression calculation, van Batenburg and Milton-Tayler (2005) and Barree and Conway (2004) debated whether β is constant or not. Huang and Ayoub (2008) proposed that the cause of debate is that large portions of their data are in turbulent regimes where the Forchheimer equation is not valid. Therefore, in order to get accurate values of the non-Darcy coefficient, it is important to investigate the limit of the Darcy and Forchheimer regimes.

A lot of research has been performed to determine how to predict the non-Darcy coefficient, which has generated numerous correlations relating the non-Darcy coefficient to porous media properties such as permeability, porosity and tortuosity. Irmay (1958) assumed a porous medium that was made up of a bundle of straight, parallel capillaries with uniform diameters, and theoretically derived and equation for β from the Navier-Stokes equations:

$$\beta = \frac{C}{k^{0.5}\varphi^{1.5}}$$ (2-5)

The parallel capillaries model proposed by Irmay (1958) oversimplifies the pore geometries of porous media, Scheidegger (1958) developed a serial model in which capillaries of different diameter were aligned in series and the correlation he derived was:

$$\beta = \frac{C_1\tau}{k\varphi}$$ (2-6)

There are also many different empirical expressions of β derived from experiments of various porous media. Pascal and Quillian (1980), based on mathematical analyses of experimental data from multi-rate wells in hydraulically fractured reservoirs, proposed a correlation given by:

$$\beta = \frac{4.8\times10^{12}}{k^{1.176}}$$ (2-7)

Jones (1987) conducted core analysis experiments on 355 sandstone and 29 limestone cores with various core types and the correlation he proposed from experimental data analysis was:

$$\beta = \frac{6.5\times10^{10}}{k^{1.55}}$$ (2-8)

Microscopic models were used in simplified porous media structures to derive the non-Darcy correlation. Thauvin and Mohanty (1998) develop a pore-level cubic lattice network model which incorporates converging-diverging of pore throat, multiple connectedness of pore

and distribution of pore sizes to describe the non-Darcy flow. By analyzing all data, they obtained a correlation which includes tortuosity and porosity inside

$$\beta = \frac{1.55 \times 10^4 \tau^{3.35}}{k^{0.98} \varphi^{0.29}} \tag{2-9}$$

Cooper, Wang, and Mohanty (1999) added anisotropy into the previous cubic lattice network model and derived a new correlation:

$$\beta = \frac{10^{-3.25} \tau^{1.943}}{k^{1.023}} \tag{2-10}$$

Only a few studies have applied pore-scale models in porous media with more complex geometries to study non-Darcy flow (M. S. Newman & Yin, 2013).

It is interesting to notice that the non-Darcy coefficient is generally directly proportional with tortuosity, but inversely proportional with permeability and porosity. Although most proposed correlations have similar functional relationships with permeability, porosity, and tortuosity, a general correlation to characterize inertial flow in real porous media with complex geometries has not been developed.

2.2.2 Microscopic Inertial Flow Behavior

In order to estimate the non-Darcy flow coefficient accurately, according to Hassanizadeh and Gray (1987) and Ma and Ruth (1993), the source of non-Darcy flow behavior is the microscopic inertial force, therefore analysis of the microscopic flow is important to fully understand the onset of non-Darcy flow. Numerical simulations and experimental methods were investigated in literatures to study the microscopic flow at both high and low Reynolds number (*Re*) in porous media. Costa, Andrade, Makse, and Stanley (1999) used finite difference methods to solve the Navier-Stokes equation in the pore space of 2D disordered porous media. Results indicated that, in the Darcy flow regime, the flow field was very heterogeneous because the

dominant viscous force caused the flow to pass through the large void space. As the inertial force started to increase at higher *Re*, the flow field became more homogeneous. Chai, Shi, Lu, and Guo (2010) implemented Lattice Boltzmann methods in 2D disordered porous media composed of random cylinders and similar flow field patterns were observed as the *Re* increases. Also, inertial forces caused some vortexes to appear behind cylinders. Fourar et al. (2004) closely examined the streamline field in porous media and indicated that eddies were formed around solids at higher *Re*. Eddies become larger and longer and also occupied the whole region between two grains with increasing *Re*. Suekane, Yokouchi, and Hirai (2003) used magnetic resonance imaging (MRI) methods to quantify velocity fields in a uniform packed bed of spheres. The flow moved along sphere surfaces in the low *Re* and velocity decreased with the increase of the cross sectional area of pore space. However, at higher *Re*, the velocity did not depend on the cross sectional area and fluid penetrated through the pore space like a jet without changing velocity. The inertial force caused the fluid to flow fast as it passed the maximum cross sectional before it slowed down. Most studies mainly applied models on highly simplified porous media structures made up by rectangular post, cylinders and spheres, only a few studies are focused on complex geometries. LBM simulations were conducted in a stochastically generated 2D porous media with complex geometries (M. S. Newman & Yin, 2013). In the Darcy flow regime, the velocity field showed that as the fluid moves from a pore throat to a pore body, the fluid spreads evenly to fill the pore space. As the Reynolds number increased, vortexes developed first in larger pore space and then spread into smaller pore spaces. Also flow in a pore channel perpendicular to the imposed pressure gradient can reverse direction. Also the viscous dissipation in the Darcy flow regime is localized in the pore throats and near the walls, however,

in the Forchheimer flow regime, it is distributed evenly in pore throats but focused along the streamlines.

2.3   3D Imaging of Porous Media

The first step of image-based pore-scale modeling is to construct a 3D digital image to represent the pore space geometry of porous media and then pore-scale modeling is performed to predict pore-scale flow behavior and macroscopic transport properties. Two different methods were used to characterize 3D pore structures, which can be classified as direct imaging methods and indirect methods. For direct imaging methods, the 3D digital image is obtained directly from X-ray computed tomography. In contrast, indirect methods create the 3D image stochastically from high resolution 2D thin sections.

2.3.1   3D X-ray Computed Tomography Imaging

X-ray CT imaging is an important tool to visualize the micro-scale pore structures of porous media. One of its most important attributes is the ability to non-invasively describe the interior structure of a porous media. A grayscale image with intensity values assigned at each voxel is the output from X-ray CT imaging. The size of voxel is one way of defining spatial resolution. The intensity value is related to the X-ray attenuation coefficient of chemical species present in the phase and the density of the phase dictate the X-ray absorption. The solid phase in the porous media typically has high X-ray attenuation, resulting in good contrast between the solid and void space. In order to quantitatively describe the pore structure and perform pore-scale modeling, grayscale images need to be segmented, which assigns the voxels to either solid or void space. This is a crucial step to accurately characterize and analyze the pore structures. Segmentation often involves noise removal as a first step followed by assignment of voxel tags

to the respective phases based on threshold values. The quality of segmentation depends on the initial image resolution, removal of noise and the method for selecting binary voxel values.

Typically, the spatial resolution of an image is the order of microns and the sample size of porous media is a few millimeters. There is a trade-off between image resolution and sample size. Images with lower resolution can cover a larger size sample which is more representative in terms of reservoir scale. However, it fails to capture details of pore structures smaller than the image resolution.

The first high-resolution tomography image of porous media was generated by Flannery, Deckman, Roberge, and D'amico (1987) with resolution approaching 1 microns. Later on, numerous research work has used X-ray CT image techniques to study porous media, including characterizing high resolution 3D pore structure, measuring pore-scale fluid distributions and saturations during immiscible displacement and drainage/imbibition process, and calculating transport properties including permeability, relative permeability and capillary pressure (Coker, Torquato, & Dunsmuir, 1996; Hazlett, 1995; Turner et al., 2004; Youssef, Bauer, Bekri, Rosenberg, & Vizika, 2009). Image-based analysis and modeling provides a link between geometric structures of porous media and their transport properties.

2.3.2 Stochastically Generated Imaging

An alternative way to obtain 3D digital images is based on stochastic methods. This approach allows combination of images with different resolutions and offers a greater spatial range than direct imaging methods (Sok et al., 2010). Several techniques have been proposed to statistically generate 3D pore structures from spatial information derived from 2D thin section images. These methods measured statistical properties such as correlation and linear path functions from 2D images using two-point (or multiple-point) correlation functions (Okabe &

16

Blunt, 2004), and Markov Chain Monte Carlo simulation (Wu et al., 2006). Another approach for stochastic generation of 3D pore structures is a process-based reconstruction procedure which models particle sedimentation processes. Øren and Bakke (2002) used this method and incorporated grain size distributions and other petrographical data from 2D slices to reconstruct 3D sandstone.

2.4 Pore-Scale Modeling in Porous Media

Based on digital images that represent the 3D pore structure, pore-scale modeling provides microscopic descriptions of flow behavior in the pore space. Two different modeling approaches used in pore-scale modeling are network modeling and direct simulation modeling. Direct simulation modeling includes lattice Boltzmann Modeling and traditional Computational Fluid Dynamics techniques such as finite element methods. This technique provides the preservation of the pore space geometry and usually requires high computational cost. In network modeling, pore structures are approximated as pores connected by throats and flow simulations are conducted by applying a mass balance to each pore in the network. The network geometry characterizes the pore geometry (pore size or volume, pore shape) as well as connectivity. Compared to direction simulation, network modeling allows flow to be modeled over orders-of-magnitude larger physical domains, because of its computational efficiency.

2.4.1 Network Modeling

Network modeling has been used to study a wide range of physical processes in porous media including drainage/imbibition process (Fenwick & Blunt, 1998), capillary pressure behavior (Al-Kharusi & Blunt, 2008), non-Newtonian flow (Lopez, Valvatne, & Blunt, 2003) and non-Darcy flow (Balhoff & Wheeler, 2009).

The first network model developed by Fatt (1956) consisted of a simplified 2D network of tubes on square or hexagonal lattices. The pore-size distributions obtained from experiments were assigned to networks via the tube size distribution. This highly simplified network model lacks a resemblance to the pore structures of real porous media. Blunt, King, and Scher (1992) used 3D networks of tube to compute relative permeability and capillary pressures in drainage and imbibition. To build a more realistic tube networks, Wardlaw, Li, and Forbes (1987) measured the real rock properties including pore and throat size, number of throats connected with each pore, degree of pore-throat size correlation and correlate these information to 3D network of tubes. The relative permeability curves are compared between correlated pore-throat models and uncorrelated pore-throat models.

The second generation network models were developed by Bryant, Mellor, and Cade (1993) who used the term "physically representative network models". Physically representative network models are directly mapped from void structure of a real three-dimensional packing. The advantage of physically representative network models compared to the first generation networks are that spatial correlation is preserved, which is a crucial effect for many transport processes in porous media. Furthermore, transport phenomena can be modeled directly without any adjustable parameters, allowing the models to become more predictive, rather than qualitative.

Recently, techniques that directly map digital images of porous media to network models have been investigated by numerous researchers due to the development of X-ray computed tomography techniques. This approach allows imaging and modeling of more-or-less arbitrary structures. The challenging part of extracting a representative network from digital images is to identify the pore bodies to properly connect them with pore throats. Two main algorithms have

been used, including medial axis based method (e.g. (Lindquist, Lee, Coker, Jones, & Spanne, 1996)) and maximal ball method (e.g. (Silin & Patzek, 2006)). The medial axis method transforms the pore space into a medial axis (skeleton) to define a graph of the pore space. Pore locations and pore-throat geometries are then added to the skeleton to define the network model. Sok et al. (2002) used this method to generate networks from XCT image of sandstone to simulate immiscible process. The maximal ball method finds the largest inscribed spheres in the pore space to define pore locations. These are then connected through the remaining constrictions to form the complete network. Dong and Blunt (2009) used this method to extract networks from sandstone, carbonate and sand-pack samples. The single phase permeability, formation factors and two phase relative permeability calculated from networks were compared to direct calculations on voxel-based images.

In network models, mass conservation of flow rate are imposed for each pore i equation (2-11) and the flow rate between pore i and j are described by equation (2-12):

$$\sum_{j=1}^{N} q_{i,j} = 0 \qquad (2\text{-}11)$$

$$q_{i,j} = \frac{g_{i,j}}{\mu}(p_j - p_i) \qquad (2\text{-}12)$$

where p_i and p_j are pressures at pore i and j, respectively, q_{ij} is the flowrate between them, μ is the viscosity, and g_{ij} is throat conductance that describes the flow dynamics between pores. Equation (2-11) and (2-12) creates a system of linear system that solves for pressure value in each pore and boundary condition are imposed as constant pressure gradient at inlet and outlet pores.

The parameter g_{ij} is critical for the validity of network models and it is a physical quantity associated with pore structures and flow behavior in pore spaces. Much research has been carried out to determine throat conductance values using correlation to pore and pore-throat radius, pore and pore-throat surface area, throat lengths etc. The single-parameter model

developed by Ewing and Gupta (1993) defined conductance as a cubic function of throat radius. In their model, throats are assumed as ideal square cross sections and the resistance between adjacent pore bodies is only concentrated in the throat. Later on, two-parameter models developed by Bryant, King, and Mellor (1993) derived throat conductance as a function of pore-throat radius and length. Pore throat shapes were approximated as cylinders and conductance equation was given by Hagen-Poiseuille equation. Thompson and Fogler (1997) mapped pore throat shape to a more realistic Venturi shape with converging-diverging geometry. Direct numerical simulations were conducted to solve the Stokes equation in pore throat and conductance was derived as a function of pore-throat radius, length and pore to pore-throat aspect ratio. Conductance was solved for noncircular throat shapes by incorporating shape functions (Bakke & Øren, 1997; Patzek & Silin, 2001).

Although network models were originally developed to study Darcy flow, and the research summarized above was mainly restricted to the Darcy flow, some studies have extended network modeling to predict the non-Darcy flow. Thauvin and Mohanty (1998) used qualitative 2D networks to produce a macroscopic relationship of pressure drop to describe non-Darcy flow. However, empirical correlations for turbulent flow in bends and pipes are utilized; therefore this model is not ideal to describe non-Darcy flow in the laminar flow regime. The hydraulic conductance used for Darcy flow can be found by solving the Stokes equation in pore-throat geometries; likewise, Balhoff and Wheeler (2009) solved the Navier-Stokes equation in the geometries representative of pore throat to quantify the non-Darcy flow behavior. 3D asymmetric diverging-converging ducts with varying diameters, length and aspect ratio were used to represent pore throat geometries. After solving the Navier-Stokes equation using the finite element method in a wide range and combination of diameters, length and aspect ratio, a

nonlinear empirical equation was derived to describe the relationship between pore pressure drop and throat flow rate with coefficients dependent on throat geometries. However, only the effect of individual pore-throats with divergence/convergence was considered to predict inertial behavior in this work, whereas both experiments and simulations have shown that tortuosity has significant effects on inertial flow. The network structures generated from real porous material are comprised of tortuous connected flow paths characteristic of real materials, which suggests that this effect could be taken into account using network modeling.

2.4.2 Lattice-Boltzmann Method

The lattice-Boltzmann Method (LBM) has been a popular method to simulate fluid flow in porous media. Unlike traditional CFD methods that solve the Navier-Stokes equations, LBM is based on microscopic models and mesoscopic kinetic equations for fluids. This is a particle-based technique that simulates the motion and collision of particles on grids. The kinetic nature of LBM enables it very suitable for fluid systems involving microscopic interactions (Guo & Zhao, 2002). Furthermore, this method is relatively easy to code and suited for parallel computing platforms.

The LBM algorithm consists of two steps: particle streaming and collision. Particle streaming involves a collection of molecules that travel with a particular velocity between nodes and particle collision is described as momentum exchange happens between particles due to particle collision at a certain node. The equation described these two processes is:

$$f_a(\vec{x}+\vec{e_a}\partial t, t+\partial t) = f_a(\vec{x}+\vec{e_a}\partial t) + \Omega \tag{2-13}$$

Where $\vec{x}$ is the node location, $\vec{e_a}$ is the velocity and Ω is the collision operator.

Succi, Foti, and Higuera (1989) was one of the first groups to utilize LBM to estimate the permeability of a 3D porous media with complex geometries and their results demonstrate the

adherence of LBM to Darcy's law. LBM simulations of single-phase flow have been applied to evaluate the permeability of various types of porous media (Bosl, Dvorkin, & Nur, 1998; Jin, Patzek, & Silin, 2004; Schure, Maier, Kroll, & Ted Davis, 2004). It has also been used to investigate effects of geometric features of solid structures, such as particle shape and size, tortuosity and porosity, on fluid transport in porous media (A Koponen, Kataja, Timonen, & Kandhai, 1998).

LBM has also been applied to study multiphase flow in porous media. In 2001, LBM multiphase flow simulations were conducted by Langaas and Papatzacos (2001) in a porous media with uniform pore-space. They showed how steady-state relative permeability depends on phase saturation, wettability, driving force and viscosity ratio were studied. LBM simulations were successfully validated by Sukop et al. (2008) against micro-x-ray tomography data on the distribution of oil, water and air phases in a porous media. M. S. Newman, & Yin, X. (2013) used LBM simulation of multiphase flow in glass beads porous media to investigate the relationship between capillary pressure, wetting phase saturation and nonwetting-wetting interfacial area. Compared to experimental results, simulation results are reliable and capture the important physical process in experiments.

2.4.3 Traditional CFD Method

Traditional CFD methods such as the finite difference method (FDM), finite volume method (FVM) and finite element method (FEM) have been applied to predict transport, elastic and electric properties of the porous media. Most studies using CFD methods are based on voxels from digital image, which eliminate the need for the mesh generation. In this case, voxels in images are treated as structural grids. Zhan, Schwartz, Toksöz, Smith, and Morgan (2010) applied the FDM to solve the Laplace equation for electrical conductivity and the Stokes

equation for the permeability of Berea sandstone. The grid size in the FDM is exactly the same as the voxel grid of the XCT image. FEM was utilized to calculate elastic properties and electrical conductivity of the sandstones; in this method, each voxel in image was taken to be a trilinear element (Arns, Knackstedt, Pinczewski, & Garboczi, 2002; Knackstedt et al., 2007).

Very few studies of CFD simulations based on unstructured meshes in porous media have been performed. Unstructured meshing can offer a more accurate and efficient representation of pore structures of porous media and also allows local mesh refinement to be used, which is valuable for heterogeneous systems. Generating unstructured meshes from 3D digital images of porous media with complex geometries is challenging. A reliable and efficient mesh generator is an essential prerequisite for CFD simulation.

Two main approaches exist for tetrahedral mesh generation: methods based on Delaunay triangulations (e.g.(Marcum & Weatherill, 1995)) and advancing front technique (e.g.(Ito, Shih, & Soni, 2004)). Delaunay triangulation involves two steps: point insertion and Delaunay construction. Inserting points in the domain provides flexibility for the mesh refinement. In this technique, points can be connected using a geometrical criterion to form a topologically valid non-intersecting set of tetrahedrons. Although the Delaunay geometrical construction provides a well-defined method with which to connect points it does not guarantee the mesh to be boundary conforming. The use of local transformations (Borouchaki, Hecht, Saltel, & George, 1995), mesh refinement (Du & Wang, 2006), and constrained Delaunay triangulations (Shewchuk, 2002) have helped address the problem of conformance to the boundary discretization.

For the advancing front technique, a surface grid is first constructed on the surface boundaries and then tetrahedral mesh in the void space is generated bounded by the surface mesh using advancing front techniques. The most common algorithm to extract the initial isosurface is

the marching cube algorithm (Lorensen & Cline, 1987). This algorithm uses a divide-and-conquer approach to create surface in a logical cube created from eight pixels (four each from two adjacent slices) to create triangle models of constant density surfaces from 3D digital image. Usually surface simplification algorithms are used to provide a way to reduce the number of triangles in the isosurface mesh while maintaining the topology of the image. The surface simplification significantly reduces the demand for larger element numbers and thus saves computational costs and memory usage. Various techniques have been proposed to simply surface meshes: edge collapse (Guéziec, 1996; Ronfard & Rossignac, 1996), which iteratively eliminates edges into vertices based upon local geometric optimality criteria and vertex clustering (Rossignac & Borrel, 1993), which groups vertices into clusters and for each cluster it computes a new representative vertex. However, neither topology nor small-scale shape details can be preserved with this method.

It is important to point out that the number of elements in unstructured meshes can be decoupled from the number of voxels in the digital image. In other words, the pore structure of the high-resolution images can be accurately described by a suitable number of elements. This feature of unstructured meshing makes it a superior tool compared to structured-grid methods to conduct pore-scale simulations in large representative porous media domains. Furthermore, there are other features of unstructured meshes that make them well suited for pore-scale studies. The additional topological freedom offered by unstructured meshes enables the mesh to conform to complicated geometries (Maddison, Marshall, Pain, & Piggott, 2011). Also the ability to vary mesh resolution enables local mesh refinement. This is especially important for porous media because applying higher mesh refinement in some smaller pores is critical to accurately predict the transport phenomena without increasing the mesh refinement of the whole domain.

Few studies have used FEM modeling with unstructured meshes to perform pore-scale simulation in porous media. Akanji and Matthai (2010) presented a finite element method to solve the Stokes equation of single-phase incompressible flow within the pore space. This numerical model is verified with analytical solutions and permeability is estimated from the computed velocity field and compared with experimental results. The pore structures of porous media from XCT image are changed for mesh generation. Interconnected pores are resolved into surfaces with six side boundaries and unstructured mesh is generated by using hybrids of tetrahedral and hexahedral elements with adaptive refinement. Lane (2011) also performed the Stokes flow simulation using finite element method in real porous media with complex geometries based on XCT image. A rigorous unstructured tetrahedral mesh generation method was developed. This thesis work is the extension work of this model.

3. Modeling and Simulation Technology

3.1 Image Acquisition and Processing

X-ray micro-tomography technology can be used to image the pore structure of real porous material. XCT images in this work were acquired at the Louisiana State University Center for Advanced Microstructures and Devices (CAMD) and the Advanced Photon Source (APS) at the Argonne National Laboratory.

Data from XCT images are voxel maps with each voxel assigned a grayscale value proportional to x-ray absorbance of the material at that location. Grayscale images are typically segmented in order to quantify pore structure and perform image-based pore-scale flow simulations, which consists of transforming the grayscale values to two or more labels that denote material phases. In this work, segmentation is performed using a two-step process: nonlinear anisotropic diffusion to remove noise followed by threshold indictor kriging for phase identification. The removal of noise in homogenous regions reduces the variance of grayscale values and this leads to narrowing of the peaks in image intensity histogram. The thresolding process converts grayscale values to material tags. In this work, thresholding converts to a binary image where labels correspond to the solid or void phase. If different material phases have good contrast in grayscale values, it is easy to perform threshold segmentation to separate the solid and void space. In many real images, however, there are overlapping peaks in the grayscale value and a simple thresholding value will either lead to errors in phase assignment or allow unassigned voxels to remain. Indictor kriging thresholding helps to address this problem by assigning probability to the voxels in the unassigned group (Oh & Lindquist, 1999). Refer to a separate paper (P Bhattad, Willson, & Thompson, 2010) for more details of image processing algorithm.

3.2   Finite Element Modeling Using Unstructured Mesh

Unstructured meshes are used to discretize the pore space of porous media prior to finite element modeling. Mesh quality is critical for the accuracy of the flow simulation. Generating unstructured meshes with an accurate representation of the complex topology of the pore space in porous media is challenging. Two unstructured mesh generation strategy will be explained in detail in this section. Both of these methods have been applied to various types of porous media including cubic packings, random sphere packings, sandstone rocks, and proppant packs.

The finite element method is one of many numerical methods to simulate fluid flow in computational fluid dynamics. In this work, single-phase incompressible viscous flow in the laminar flow regime is solved. Details of finite element discretization of the Stokes equations and the Navier-Stokes equations are described below.

3.2.1   Unstructured Mesh Generation

3.2.1.1 AVIZO Mesh Generation

The commercial software package AVIZO is an industrial application for data visualization and analysis including 3D image data processing, mesh generation, and post-processing of simulations. AVIZO can be used to generate unstructured tetrahedral meshes from 3D digital image data. The workflow is as follows:

1. Import 3D segmented (binary) images into the software with specific dimensions and voxel size assigned. Segmented image data contains solid/void assignment information for each voxel (voxels in the solid phase are assigned as 0 and in the void phase are assigned as 1).

2. Select *Image* and use *Convert Image Type Editor* to convert image to *8-bit label* image type.

3. Select *8-bit label* and use *Generate Surface Editor* to extract the isosurface of the geometry boundary with triangles.

4. Use *Surface Simplification Editor* to simplify surface mesh by specifying the minimum and maximum triangular size. *Surface View Module* is used to visualize the surface mesh.

5. Select *surface mesh* and use *Generate Tetra Grid Editor* to generate a tetrahedral mesh. *Tetra Grid View Module* is used to visualize the volume mesh.

Figure 3-1 shows the mesh generation workflow in an AVIZO project.
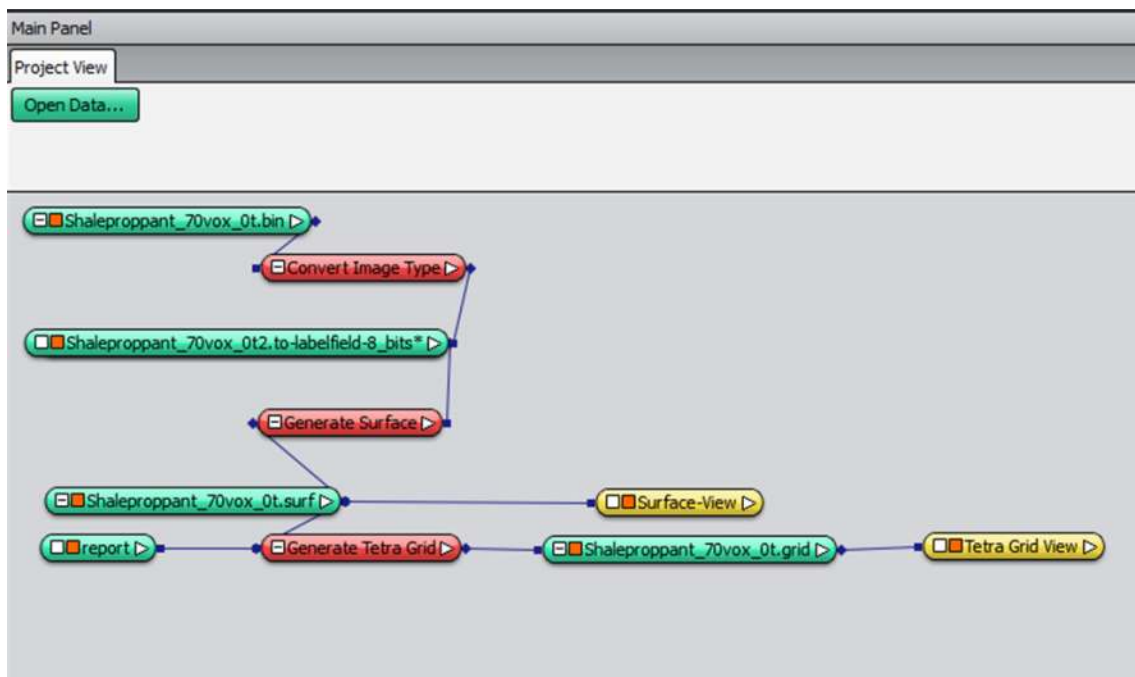
Figure 3-1: The mesh generation workflow in an AVIZO project

The details of each step are the following. Surface generation is based on the marching cube algorithm. Three options exist in the surface generation including no smoothing, constrained smoothing and unconstrained smoothing. Both unconstrained and constrained smoothing use Gaussian smoothing algorithms applied to label weights. In the constrained smoothing, any two voxel centers that have been labeled differently before the smoothing are separated by the generated surface, which is not necessarily the case for the unconstrained

smoothing. The amount of smoothing can be controlled via the smoothing extent. Usually the option *add border* is checked to ensure the resulting surface is closed and *adjust cords* is checked so that the resulting surface appears to be sharply cut off at the boundaries.

The number of triangles resulting from surface mesh generation is usually very large and it is not suitable for visualization and simulation. The *Surface Simplify Editor* uses an edge collapse algorithm to reduce the number of triangles (by controlling the desired number of triangles on surface as well as minimum and maximum triangle edge length). Choosing different values for these parameters provides flexibility to generate a variety of mesh resolutions. It is important to choose a suitable maximum edge length value. If it is too large, mesh will be too coarse to preserve the topology of the pore structure. Figure 3-2 shows the surface mesh without simplifying and after simplifying using the maximum/minimum triangle length 3/1 and 5/1 respectively. It shows that original surface mesh from marching cube algorithm is uniform and structured. After simplifying, the elements become unstructured and larger.

After surface mesh generation is completed, several criteria need to be checked for the surface mesh to be ready for tetrahedral mesh generation:

1. Intersection test. The surface should be free of intersection triangles. If intersection triangles are detected, they can be repaired using edge flip.

2. Orientation Test. The orientation test is performed after the intersection test is passed. The orientation of a small number of triangles may be inconsistent, resulting in a partial overlap of the materials bounded by the triangles. In case of such incorrect orientations, there is an automatic repair.
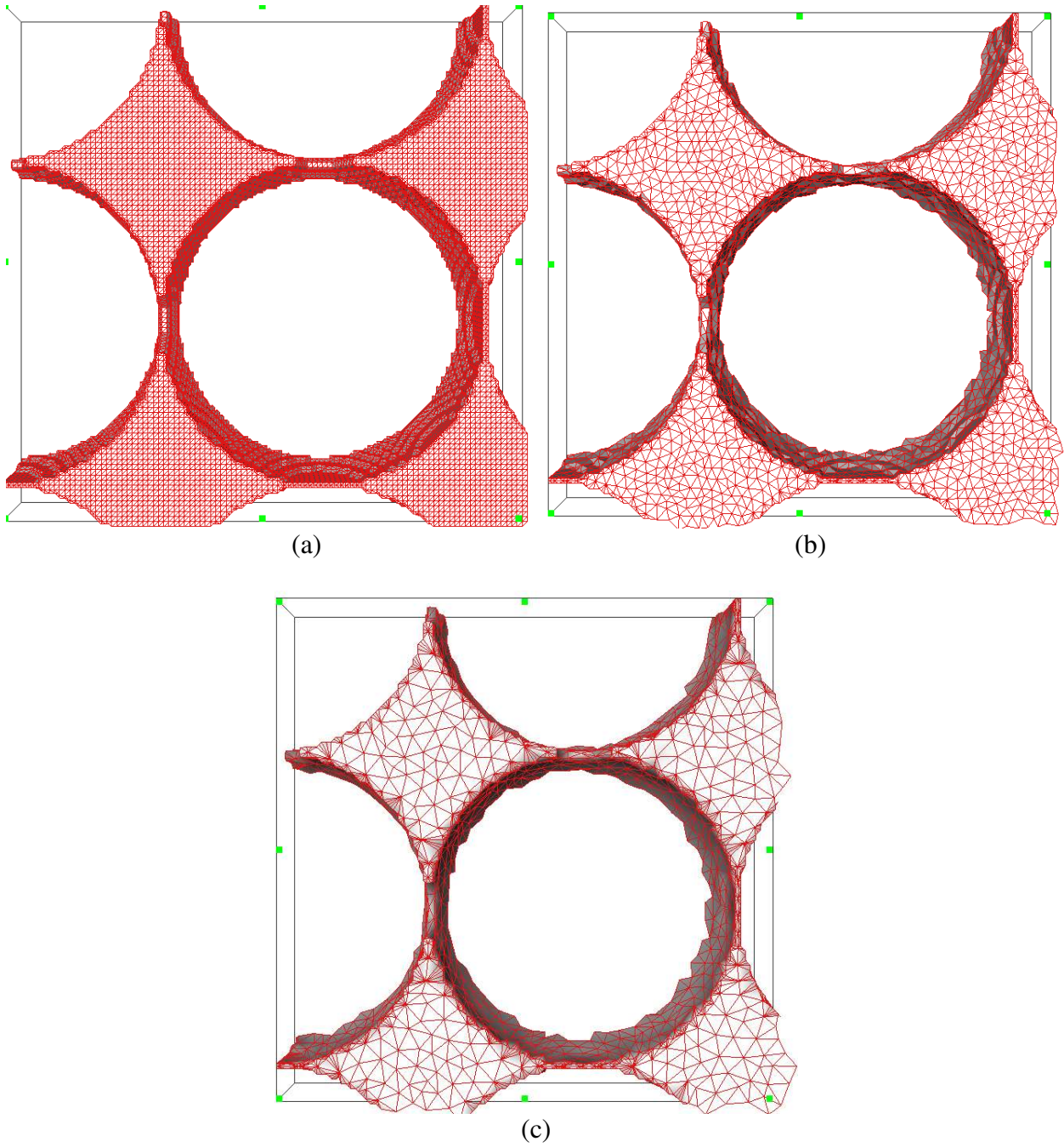
Figure 3-2 : (a) The initial surface mesh without simplify, (b) The surface mesh after simplifying with maximum triangle length 3 voxel and minimum triangle length 1 voxel, (c) The surface mesh after simplifying with maximum triangle length 5 voxel and minimum triangle length 1 voxel of the 312^3-voxel cubic packing sample.

3. Aspect Ratio calculation. This computes the ratio of the radius of the circumcircle and the inscribed circle for each triangle. The largest aspect ratio should be less than 20 (even better if it is less than 10). The aspect ratio can be improved using edge flip.

4. Closedness Test. The surface triangles should form a closed surface.

Once the surface mesh is created, the tetrahedral mesh (bounded by the surface mesh) is generated using the advancing front algorithm. It allows the user to define a desired mesh size (mean length of inner edges). Varying the mesh size provides flexible internal mesh resolution. After tetrahedral elements are generated, the grid is saved as a hypermesh format (hmascii). The mesh file contains information including node locations and connectivity of elements. No boundary condition information is included in the hypermesh.

3.2.1.2 Implicit Voxel Meshing

An in-house mesh generator with a Delaunay-tessellation based algorithm has been developed. The algorithm is summarized as follows:

1. A set of points is distributed into the entire domain (including both the void and solid space) and connected using a Delaunay tessellation. The density of points provides flexibility in mesh refinement. The points are always disordered at the local scale (to prevent a degenerate tessellation). However, they can be either uniform or nonuniform density depending on whether certain regions of the domain are targeted for refined meshing.

2. All elements that are bisected by the solid-void interface are collected.

3. The locations where the void/solid surface cuts through edges of elements are identified. These elements are then split into multiple parts to respect the phase boundary.

4. Collect the subset of elements in the void space and perform smoothing to improve the quality of mesh.

The in-house mesh file includes node locations, node labeling (for the inlet boundary, outlet boundary, solid/void interface, and interior nodes), nodes numbers for each element, and connectivity of elements. Hypermesh files generated from AVIZO are converted to the in-house data format for finite element simulations using the in-house code (details described in section 3.2.2.2). If COMSOL is used to run FEM simulations, the in-house mesh needs to be converted to COMSOL native mesh format. The boundary nodes on the inlet/outlet surface are labeled during the conversion.

3.2.2 Finite Element Modeling

The incompressible Navier-Stokes equation (3-1) for single phase Newtonian fluid flow in the laminar flow regime is solved using the finite element method in the void space of porous media (discretized by mesh generation method described in the previous section).

$$\rho(\frac{\partial \mathbf{v}}{\partial t} + \mathbf{v} \cdot \nabla \mathbf{v}) = -\nabla p + \mu \nabla^2 \mathbf{v} + f$$
$$\nabla \cdot \mathbf{v} = 0$$
(3-1)

In the Darcy flow regime, the inertial term in the Navier-Stokes equation can be neglected and the governing equation is simplified to the steady-state Stokes equation (3-2) :

$$\nabla p = \mu \nabla^2 \mathbf{v}$$
$$\nabla \cdot \mathbf{v} = 0$$
(3-2)

3.2.2.1 Shape Functions

Shape functions interpolate the solution between the discrete values of variables stored or computed at nodes in the mesh. Assume an element e is defined by m number of nodes: the dependent variable u at any point within this element can be approximated as:

$$u = \sum_{i=1}^{m} N_i u_i$$
(3-3)

where N_i is defined as the shape function and u_i are values of variable u at each node.

The tetrahedral P2P1 element (or Taylor-Hood element) is used in both the Stokes and Navier-Stokes flow simulations. This element type has quadratic shape functions used for velocity approximation and linear shape functions for pressure approximation. Each element has ten nodes: four vertexes and six edge nodes are used for velocity while only the four vertexes nodes are used for pressure. Figure 3-3 shows the velocity and pressure nodes in one element. The P2P1 element is a popular element type for the finite element method because it satisfies the LBB criteria (Gresho, Sani, & Engelman, 1998). Any element satisfying this condition will prevent the development of spurious pressure behavior (Gresho et al., 1998). Due to the higher order approximation of velocity in P2P1 elements, more degrees of freedom are introduced, which leads to a larger computational cost. For Navier-Stokes simulations, we also use the P1P1 element. Both velocity and pressure are approximated with linear function in P1P1 elements, using only the four vertexes for both velocity and pressure, as shown in Figure 3-3.
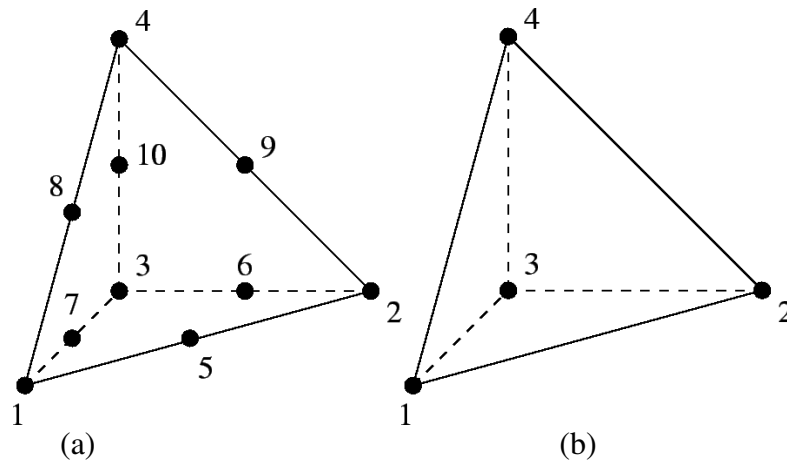
Figure 3-3: (a) P2P1 tetrahedral element, (b) P1P1 tetrahedral element (dots represent nodes)

At any point P (x, y and z) inside one element, the volume coordinates L_1, L_2, L_3 and L_4 for nodes 1, 2, 3 and 4, shown as Figure 3-4, are defined as:

33
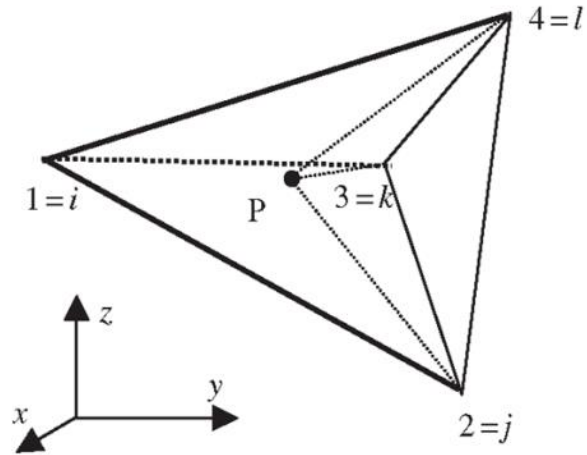
Figure 3-4: A tetrahedral element with any point p inside this element

$$L_1 = \frac{V_{P234}}{V_{1234}}, L_2 = \frac{V_{P134}}{V_{1234}}, L_3 = \frac{V_{P124}}{V_{1234}}, L_4 = \frac{V_{P123}}{V_{1234}} \tag{3-4}$$

where V_{1234} is the volume of tetrahedron 1234; V_{P234} is the volume of tetrahedron P234; V_{P134} is the volume of tetrahedron P134; V_{P124} is the volume of tetrahedron P124; V_{P123} is the volume of tetrahedron P123.

It can easily be confirmed that:

$$L_1 + L_2 + L_3 + L_4 = 1 \tag{3-5}$$

Also it can easily be confirmed that:

$$L_i = \begin{cases} 1 & \text{at the home node } i \\ 0 & \text{at the other nodes } j, k, l \end{cases} \tag{3-6}$$

Therefore, the shape functions for linear approximation of pressure variable in the P2P1 element are given in the volume coordinates as follows:

$$N_i = L_i \text{ for vertexes nodes } i \tag{3-7}$$

The shape functions for the quadratic approximation of the velocity variable in a P2P1 element are given in the volume coordinates as follows:

$$N_i = (2L_i - 1)L_i \quad \text{for vertexes nodes } i$$

$$\left.\begin{array}{l} N_5 = 4L_2L_3 \\ N_6 = 4L_1L_3 \\ N_7 = 4L_1L_2 \\ N_8 = 4L_1L_4 \\ N_9 = 4L_2L_4 \\ N_{10} = 4L_3L_4 \end{array}\right\} \quad \text{for mid-edge nodes} \tag{3-8}$$

3.2.2.2 The Stokes Equation

The stress form of the Stokes equation is used for finite element spatial discretization because it leads to the natural boundary condition (Gresho et al., 1998). This is a suitable boundary condition for porous media.

$$\nabla \cdot \boldsymbol{\sigma} = 0 \tag{3-9}$$

where $\boldsymbol{\sigma}$ is given by:

$$\boldsymbol{\sigma} = \begin{pmatrix} \sigma_{xx} & \tau_{xy} & \tau_{xz} \\ \tau_{yx} & \sigma_{yy} & \tau_{yz} \\ \tau_{zx} & \tau_{zy} & \sigma_{zz} \end{pmatrix} \tag{3-10}$$

The Galerkin method is employed to derive the discrete equations of the Stokes equation. The first step is to obtain the weak form of the governing equations for a given element domain Ω_e bounded by Γ_e, shown as follows:

$$\int_{\Omega_e} W(\nabla \cdot \boldsymbol{\sigma}) d\Omega = 0 \tag{3-11}$$

Here the Bubnov-Galerkin method is applied in which the weighting function W is selected to be identical to the shape function N (Huebner, Dewhirst, Smith, & Byrom, 2008). Utilizing the Gauss theorem and substituting the stress into velocity (u, v and w) and pressure (p) variables, the weak form of the x component is written as:

35

$$\int_{\Omega_e}\left[\left(2\mu\frac{\partial u}{\partial x}-p\right)\frac{dN}{dx}+\mu\left(\frac{\partial u}{\partial y}+\frac{\partial v}{\partial x}\right)\frac{dN}{dy}+\mu\left(\frac{\partial u}{\partial z}+\frac{\partial w}{\partial x}\right)\frac{dN}{dz}\right]d\Omega=\int_{\Gamma_e}\overline{\sigma_x}Nd\Gamma \qquad (3\text{-}12)$$

where,

$$\overline{\sigma_x}=(\sigma_x-p)n_x+\tau_{xy}n_y+\tau_{xz}n_z$$

The surface traction $\overline{\sigma_x}$ in the right hand side of equation (3-12) is a true boundary condition for porous media. Applying inlet and outlet boundary condition in porous media is a challenging problem because usually the computational domain is an arbitrary sub-volume cut from a large porous media sample, so the detailed boundary conditions on this extracted domain is generally not known. The shape equation approximation for variables velocity (u, v and w) and pressure (p) is substituted into equation (3-12) results in:

$$\int_{\Omega_e}\left[\begin{array}{c}\left(2\mu\frac{\partial N}{\partial x}\{u\}-N^p\{p\}\right)\frac{dN}{dx}\\[2mm]+\mu\left(\frac{\partial N}{\partial y}\{u\}+\frac{\partial N}{\partial x}\{v\}\right)\frac{dN}{dy}\\[2mm]+\mu\left(\frac{\partial N}{\partial z}\{u\}+\frac{\partial N}{\partial x}\{w\}\right)\frac{dN}{dz}\end{array}\right]d\Omega=\int_{\Gamma_e}\overline{\sigma_x}Nd\Gamma \qquad (3\text{-}13)$$

where N is the shape function for velocity and N^p is the shape function for pressure.

The x, y and z components of the momentum equation and the continuity equation are combined together and the matrix form of the equation is given as:

$$\begin{bmatrix}2K_{11}+K_{22}+K_{33} & K_{12} & K_{13} & L_1\\ K_{12}{}^T & K_{11}+2K_{22}+K_{33} & K_{23} & L_2\\ K_{13}{}^T & K_{23}{}^T & K_{11}+K_{22}+2K_{33} & L_3\\ L_1{}^T & L_2{}^T & L_3{}^T & 0\end{bmatrix}\begin{Bmatrix}u\\v\\w\\p\end{Bmatrix}=\begin{Bmatrix}R_u\\R_v\\R_w\\0\end{Bmatrix} \qquad (3\text{-}14)$$

where,

$$K_{11}=\int_{\Omega_e}\mu\left\{\frac{\partial N}{\partial x}\right\}\left[\frac{\partial N}{\partial x}\right]d\Omega,\quad K_{22}=\int_{\Omega_e}\mu\left\{\frac{\partial N}{\partial y}\right\}\left[\frac{\partial N}{\partial y}\right]d\Omega,\quad K_{33}=\int_{\Omega_e}\mu\left\{\frac{\partial N}{\partial z}\right\}\left[\frac{\partial N}{\partial z}\right]d\Omega,$$

36

$$K_{12} = \int_{\Omega_e} \mu \left\{ \frac{\partial N}{\partial y} \right\} \left[\frac{\partial N}{\partial x} \right] d\Omega, \quad K_{13} = \int_{\Omega_e} \mu \left\{ \frac{\partial N}{\partial z} \right\} \left[\frac{\partial N}{\partial x} \right] d\Omega,$$

$$L_1 = -\int_{\Omega_e} \left\{ \frac{\partial N}{\partial x} \right\} N^P d\Omega, \quad L_2 = -\int_{\Omega_e} \left\{ \frac{\partial N}{\partial y} \right\} N^P d\Omega, \quad L_3 = -\int_{\Omega_e} \left\{ \frac{\partial N}{\partial z} \right\} N^P d\Omega$$

$$R_w = \int_{\Gamma_e} \overline{\sigma_x} \{N\} d\Gamma, \quad R_w = \int_{\Gamma_e} \overline{\sigma_y} \{N\} d\Gamma, \quad R_w = \int_{\Gamma_e} \overline{\sigma_z} \{N\} d\Gamma$$

Assume the computational domain for finite element simulation consists of N_n number of global velocity nodes, N_p number of global pressure nodes and N_e number of elements, and each node is associated with dependent variables velocity (u, v and w) and pressure (p). The equation derived above is for one elements Ω_e, and this equation for one local element which consists of m number of local nodes needs to map uniquely to the global elements in the mesh. Mesh data including the element connectivity and node numbers in the element provides the mapping information. Assembling the equations for all elements forms a global set of equations with unknown variables velocity vector $\{\mathbf{u}\}$ and pressure vector $\{\mathbf{p}\}$ is given as:

$$\begin{bmatrix} \mathbf{K} & \mathbf{L} \\ \mathbf{L}^T & 0 \end{bmatrix} \begin{Bmatrix} \mathbf{u} \\ \mathbf{p} \end{Bmatrix} = \begin{Bmatrix} \mathbf{R} \\ 0 \end{Bmatrix} \tag{3-15}$$

where,

$$\{\mathbf{u}\} = \begin{Bmatrix} u_1 \\ \dots \\ u_{Nn} \\ v_1 \\ \dots \\ v_{Nn} \\ w_1 \\ \dots \\ w_{Nn} \end{Bmatrix}, \quad \{\mathbf{p}\} = \begin{Bmatrix} p_1 \\ \dots \\ p_{Np} \end{Bmatrix}$$

An in-house code for the Stokes equation developed by Lane (2011) is used for all low-Reynolds number simulations. A constant normal stress force is applied in the inlet and outlet boundary faces. The no-slip boundary condition is applied at the interior solid/void interface as well as the four exterior sides of the domain (i.e., those not specified as inlet or outlet). P2P1 elements are used and the direct solver PARDISO from the Intel MKL library is employed to solve linear systems of equations. Simulations are performed on a high performance computing system with a 37 compute node cluster. Each node has two 2.93 GHz Quad Core Nehalem Xeon 64-bit Processors with maximum memory of 96 GB.

3.2.2.3 The Navier-Stokes Equation

The same Galerkin method used for the Stokes equation discretization is employed to discretize the Navier-Stokes equation and the discrete equation of *x* component for one given element domain Ω_e bounded by Γ_e is given as follows:

$$
\int_{\Omega_e} (\rho N\{u_t\}) N d\Omega + \int_{\Omega_e} (\rho u \frac{\partial N}{\partial x}\{u\} + \rho v \frac{\partial N}{\partial y}\{u\} + \rho w \frac{\partial N}{\partial z}\{u\}) N d\Omega +
$$

$$
\int_{\Omega_e} \left[\begin{array}{l} \left(2\mu\dfrac{\partial N}{\partial x}\{u\} - N^p\{p\}\right)\dfrac{dN}{dx} \\[2mm] +\mu\left(\dfrac{\partial N}{\partial y}\{u\} + \dfrac{\partial N}{\partial x}\{v\}\right)\dfrac{dN}{dy} \\[2mm] +\mu\left(\dfrac{\partial N}{\partial z}\{u\} + \dfrac{\partial N}{\partial x}\{w\}\right)\dfrac{dN}{dz} \end{array} \right] d\Omega = \int_{\Gamma_e} \overline{\sigma_x} N d\Gamma \tag{3-16}
$$

The global matrix equations after assembling equations of all elements in the computational domain are:

$$
\begin{bmatrix} \mathbf{M} & 0 \\ 0 & 0 \end{bmatrix} \begin{Bmatrix} \mathbf{u}_t \\ 0 \end{Bmatrix} + \begin{bmatrix} \mathbf{K} + \mathbf{N(u)} & \mathbf{L} \\ \mathbf{L}^T & 0 \end{bmatrix} \begin{Bmatrix} \mathbf{u} \\ \mathbf{p} \end{Bmatrix} = \begin{Bmatrix} \mathbf{R} \\ 0 \end{Bmatrix} \tag{3-17}
$$

where the mass matrix **M** is associated with the transient term and the matrix **N** is associated with the inertial term.

38

The projection method is a popular numerical method to solve the Navier-Stokes equations. The challenging part of solving the N-S equation is that the pressure and velocity are coupled by the continuity constraints. The attractive feature of projection methods is that, at each time step, one only needs to solve decoupled equations for the velocity and pressure, making it very efficient for large scale numerical simulations. Projection methods reduce the Navier-Stokes equations (a nonlinear partial differential equation) into a set of linear ordinary differential equation (Langtangen, Mardal, & Winther, 2002).

The projection method starts by solving a predicted velocity $\mathbf{u}^*$ at a new time step $t+1$ using the momentum equation.

$$\mathbf{Mu}^* = \mathbf{Mu}^t + \Delta t(-\mathbf{N}(\mathbf{u}^t)\mathbf{u}^t - \mathbf{Lp}^t - \mathbf{Ku}^t + \mathbf{R}^t) \tag{3-18}$$

This predicted velocity does not satisfy the continuity equation, therefore a correction of velocity $\mathbf{u}^{t+1}$ is needed to compute by adding the continuity constraint.

$$\mathbf{u}^{t+1} = \mathbf{u}^* + \mathbf{u}^c \tag{3-19}$$

The correct velocity $\mathbf{u}^{t+1}$ should satisfy the continuity equation at $t+1$:

$$\mathbf{L}^T\mathbf{u}^{t+1} = \mathbf{0} \tag{3-20}$$

The difference between $\mathbf{u}^{t+1}$ and $\mathbf{u}^*$ $\mathbf{u}^c$ satisfy:

$$\mathbf{u}^c = -\Delta t\mathbf{M}^{-1}\mathbf{L}\boldsymbol{\varphi}, \ \boldsymbol{\varphi} = \mathbf{p}^{t+1} - \mathbf{p}^t \tag{3-21}$$

Since $\mathbf{u}^{t+1}$ is needed to satisfy the continuity equation, a Poisson equation needs to be solved for the pressure difference:

$$\mathbf{L}^T\mathbf{M}^{-1}\mathbf{L}\boldsymbol{\varphi} = \frac{1}{\Delta t}\mathbf{L}^T\mathbf{u}^* \tag{3-22}$$

The last step is to update the pressure and velocity for the time step $t+1$:

$$\mathbf{p}^{t+1} = \mathbf{p}^t + \boldsymbol{\varphi}, \ \mathbf{u}^{t+1} = \mathbf{u}^* - \Delta t\mathbf{M}^{-1}\mathbf{L}\boldsymbol{\varphi} \tag{3-23}$$

In this work, the commercial software COMSOL is used to solve flow behavior in the porous media. The single-phase-flow model with laminar flow in fluid-flow module of COMSOL Multiphysics 4.2a is used. The Navier-Stokes equations are solved using the projection method with the finite element method in this module. The first step is to import mesh structures into COMSOL. The hypermesh generated from AVIZO is converted to the in-house mesh format, which contains node locations, element nodes, element connections, and nodes labels for inlet, outlet, no-slip and interior boundaries. The in-house mesh is then converted to the COMSOL native mesh format. In the COMSOL mesh format, element surfaces which belong to the inlet/outlet boundary are grouped together as several faces and this eliminates the process of manually defining each element surface (which are often up to 10^5 faces) as the inlet/outlet boundary. A constant normal stress force is applied in the inlet and outlet boundary faces. The no-slip boundary condition is applied at the interior solid/void interface as well as the four exterior sides of the domain (i.e., those not specified as inlet or outlet). COMSOL provides the options of element type with both P2P1 and P1P1 elements. The direct solver PARDISO with a nested dissection preordering algorithm and the pivoting perturbation parameter set at 10^{-8} is employed to solve the linear systems of equations. The nodal velocity and pressure values are the output of the simulation, and results will be used for post-processing and visualization. Simulations were performed on a computer with 96 GB memory and two quad-core Xeon 64-bit processors with maximum operating cycles of 2.93 GHz.

3.3 Network Modeling

In this work, networks are generated using the voxel-based extraction algorithm describe elsewhere (Pradeep Bhattad, Willson, & Thompson, 2011). The input of this algorithm is a binary image of the porous material with voxel labels for solid or void space. The pore center

seeds are identified from performing a voxel burn to find local maxima in the distance function from the surface. A nonlinear optimization process is used to refine the initial pore seeds so that each pore is identified as a maximal inscribed sphere. The maximal inscribe sphere is a hypothetical sphere constrained by the surrounding solid space such that it cannot move or grow. The voxels belonging to a given pore are collected by moving from the center using a watershed-type algorithm (Thompson, Willson, & Zhang, 2006). Pores are merged if significant overlapping of adjacent pores occurred. Once these two steps are complete, determining the geometric parameters and constructing the pore network connectivity is a straightforward process. The pore volume is obtained by summing the volume of all voxels assigned to this particular pore. The inscribed pore radius is equivalent to the radius of the maximum inscribed sphere in the second step. In network structures, pore throats have no volume and are defined by the faces where two pores have a contact face. The total cross-sectional area of the throat is defined by summing the projected area (along the unit normal of that face) of voxel faces at the interface. The inscribed radius of the throat is calculated by determining the maximum inscribed sphere on the interface between pores.

The governing equation for each pore i in network modeling is given as:

$$\sum_{j=1}^{N} \frac{g_{i,j}}{\mu}(p_j - p_i) = 0 \qquad (3\text{-}24)$$

This equation is equivalent to the continuity equation at the pore scale. Mass conservation is imposed on each pore in the network modeling approach. Throat conductance $g_{i,j}$ characterize flow properties of the pore-throat and usually are estimated based on the geometry of pore-throat. Disconnected pores (no connectivity with other pores) and dead-end pores (no connectivity with other pores and connected to an open boundary) need be removed before assembling the governing equation. Assembling the governing equation of every pore with pore

connectivity information forms the sparse linear systems of equations to solve pressure value of each pore. A constant pressure value is assigned in the inlet and outlet pore. This linear system is stored as a sparse matrix and the direct solver PARDISO from the Intel MKL library is employed. Simulations are performed on the same high performance computer system as the in-house stokes flow code with 37 compute node cluster. Each node has two 2.93 GHz Quad Core Nehalem Xeon 64-bit Processors with maximum memory is 96 GB.

3.4   Porous Media Parameters Calculation

3.4.1   Porosity and Surface Area

Porosity calculation from XCT images is direct and easy. For a given volume of interest in 3D digital images, porosity is the ratio of the volume of void voxels to the total volume.

However, computing surface area from digital images is difficult. Specific surface area is the ratio of solid-void surface area and the total volume. The solid-void surface area is calculated using the algorithm described by Thompson (2007).

3.4.2   Intrinsic Permeability

Intrinsic permeability is a continuum-scale property that quantifies how easily a fluid can flow through the pore space. It is generally related to the pore structure, including parameters such as porosity, tortuosity and hydraulic radius. It is defined by Darcy's law:

$$k = \frac{\mu v}{\nabla P} \tag{3-25}$$

To determine the intrinsic permeability from pore-scale flow simulations, we first calculate the inlet/outlet flow rate by integrating the surface velocity (obtained from the pore scale simulation of the Stokes flow) and the surface area over elements on the inlet or outlet boundary using:

$$Q = \iint \mathbf{v} \cdot d\mathbf{A} \tag{3-26}$$

The superficial velocity v is then computed from flow rate Q divided by the inlet/outlet area of the computational domain.

3.4.3 Reynolds Number

The characteristic length used for the Reynolds number for porous media is generally defined as the particle diameter, and then the Reynolds number is defined as:

$$Re = \frac{\rho d_P Q}{\mu A} \qquad (3\text{-}27)$$

where d_p is particle diameter and ρ is the fluid density.

3.4.4 Non-Darcy Coefficient

The non-Darcy flow coefficient is calculated by rearranging the Forchheimer equation:

$$\frac{\nabla P}{v\mu} = \frac{1}{k_{app}} = \frac{1}{k} + \beta\left(\frac{\rho v}{\mu}\right) \qquad (3\text{-}28)$$

where k_{app} is the apparent permeability calculated from Darcy's law. The intrinsic permeability is only related to pore structure and it is calculated under the condition of the Stokes flow. The apparent permeability decreases as the velocity increase since the pressure drop is not linearly related with velocity at higher Reynolds numbers. The terms $1/k_{app}$ and $\rho v/\mu$ are obtained for a range of flow rates by assigning different normal stress force at the inlet/outlet boundary in each simulation. A straight line with slope β and intercept $1/k$ is fit from the plot of $1/k_{app}$ versus $\rho v/\mu$.

4.　　FEM and LBM Comparison

Pore-scale LBM and FEM modeling are two powerful approaches for direct simulation of flow in porous media. However, few studies exist in the literature that compare LBM and other computational fluid dynamics numerical methods such as FDM, FVM and FEM. Breuer, Bernsdorf, Zeiser, and Durst (2000) studied confined laminar flow past a square cylinder using FVM and LBM. They found good agreement between the two methods for both steady and unsteady flows. Geller, Krafczyk, Tölke, Turek, and Hron (2006) compared the efficiency of LBM and CFD solvers. Based on their results, they found LBM comparable to CFD methods (FVM and FEM) but asymptotically slower for the steady-state Stokes flow because the asymptotic algorithmic complexity of LBM is not optimal compared to multi-grid solvers incorporated in the FEM and FVM codes that were used. They observed that for the weakly compressible case, the LBM approach has a substantial wall clock time advantage compared to the FVM. Kandhai et al. (1999) performed a detailed comparison between FEM and LBM for three-dimensional fluid flow simulations in a SMRX static mixer. They found excellent agreement between results of two simulation methods. Manwart, Aaltosalmi, Koponen, Hilfer, and Timonen (2002) performed a quantitative comparison of the LBM and FDM for flow simulations of four three-dimensional samples of porous media. They mentioned that time requirements of two methods are quite similar, while the memory requirements of LBM are higher.

Details of FEM modeling are described in Chapter 3. LBM simulations in this work were conducted by Ali Takbiri Borujeni. Please refer to (Borujeni, 2013) for more details of LBM modeling.

In the work, the term image resolution for 3D digital images is used to define the size of each voxel. Higher image resolution means smaller voxel size and generally implies a more detailed description of pore geometries. For a fixed sample size, higher image resolution results in larger number of voxels in the digital image. Usually, LBM modeling operates directly on the voxels in a digital image, so higher image resolution dictates a larger computational cost. As expected, poor image resolution affects the accuracy of LBM simulations. This effect can be minimized by increasing lattice resolution (decreasing voxel size) (Chukwudozie, 2011). There is always a trade-off between the image resolution and computational power.

FEM modeling in this work uses unstructured tetrahedral meshes to represent the pore structure. A major advantage of this approach is that it allows the numerical (mesh) resolution to be selected independently of the image resolution (provided the mesh-generation algorithm enables this choice). Coarse meshes usually fail to preserve pore geometry, which in turn can have a large effect on the accuracy of simulations. A convergence study of different element resolutions on pore structure and/or transport properties is important to quantify numerical errors in FEM modeling.

In this chapter, artificial (computer generated) 3D consolidated random sphere packing with image resolutions between 2-10 microns are generated. Different image resolutions result in different pore structures because of the inability of the voxel structure to capture the spherical surfaces exactly. Both LBM and FEM simulations of Stokes flow are performed on samples with all image resolutions. Macroscopic permeability is calculated and microscopic velocity fields in the pore space are analyzed for these two approaches. This work studies how simulated permeability is affected by image resolution in both LBM and FEM simulations. Permeability

values of all image resolutions are compared between LBM and FEM. The microscopic velocity fields from LBM and FEM in highest image resolution sample are compared quantitatively.

4.1 Materials

A computer-generated three-dimensional sphere packing is used for flow simulations in this study. Computer-generated images provide flexibility in image resolution. They can be discretized to any desired image resolution without any segmentation errors, which are inherent in digitizing real porous media images. In order to mimic consolidated porous media, spherical particles are allowed to overlap by increasing the sphere radius (starting from dense but non-overlapping packing). A cubic domain consisting of 1000 spheres and dimension one millimeter on each size is used. The size distribution of the spheres is 25% of the mean, which is 100 microns. In the process of increase the sphere radii, the porosity decreases from approximately 36.5 % to 14.5 %.

The sphere packing is discretized to digital (voxel) images having five different resolutions. The range is from 2 microns (a 500^3-voxel image) to 10 microns (a 100^3-voxel image). Figure 4-1 shows 2D slices from the lowest and highest resolution images. As Figure 4-1 shows, the high resolution image has significantly smoother solid and void interfaces compared to the low-resolution image. Some pore connectivity is lost in the low-resolution image. Porosity and specific surface area values for the five different images are listed in the Table 4-1. Variations in porosity are very small for different image resolutions, but surface area increases as the image resolution improves.

4.2 Results and Discussions

4.2.1 Macroscopic Permeability Comparison

A feature of using unstructured meshes for the FEM simulations is that the number of
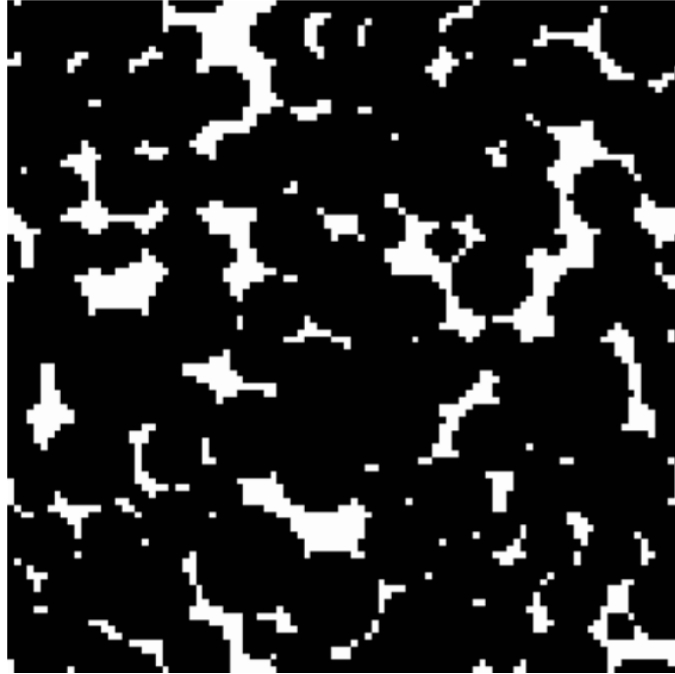
(a)
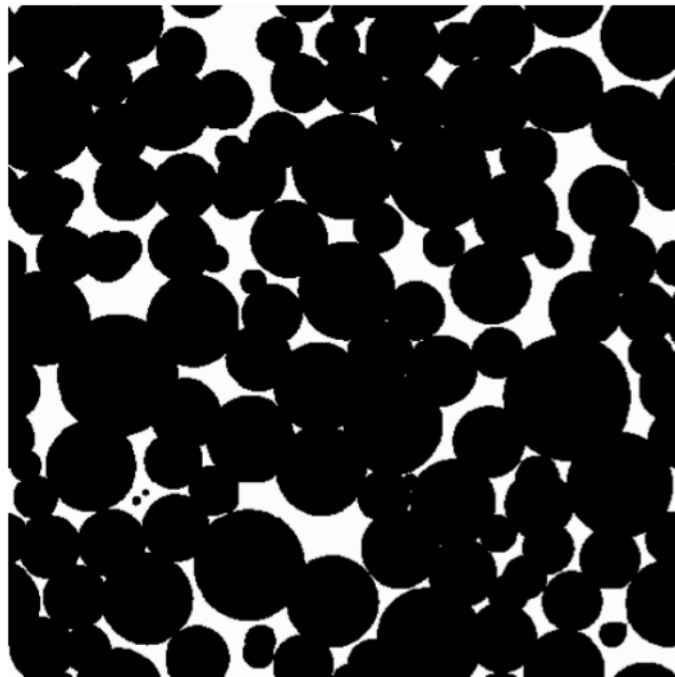
(b)

Figure 4-1: Images of the random sphere pack with two different resolutions: (a) 10 microns, (b) 2 microns.

Table 4-1: Image porosity (φ) and image specific surface areas (S_v) for different image resolutions

Image Size (voxel)	Image Resolution(μm)	φ (%)	S_v (1/m)
100	10	14.33	18374.80
200	5	14.34	19808.62
300	3.3333	14.34	20298.41
400	2.5	14.34	20554.09
500	2	14.34	20705.89

elements can be decoupled from the image resolution (voxel size); therefore, meshes with similar numbers of elements can be obtained from different image resolutions. This allows us to study the impact of image resolution more independently of numerical resolution than when the two are directly related.

In order to find an optimal number of elements for FEM simulations, a study on numerical convergence is carried out. Comparisons of mesh porosity versus image porosity, mesh surface area versus image surface area, and permeability values are calculated for various numbers of elements. Mesh porosity and mesh surface area values reported here are based on the pore structure that is mapped out the complete set of tetrahedrons (Mesh porosity is calculated as the ratio of total elements volume to total sample volume). Mesh surface area is calculated as total area of element faces that are part of the void-solid interface. Figure 4-2 shows the effect of the number of elements on structural and transport properties for 100^3 and 500^3-voxel images. It can be seen in Figure 4-2(a) that permeability increases as the number of elements increases. The permeability value starts to converge to a constant value at a certain element number. However, the permeability values for the two image resolutions are different. Figure 4-2(b) depicts the change of the mesh porosity relative to the image porosity as the number of elements increases. For the 500^3-voxel image, relative porosity estimates are almost constant with changes in number of elements, which suggests that the smaller number of elements is sufficient to preserve the pore
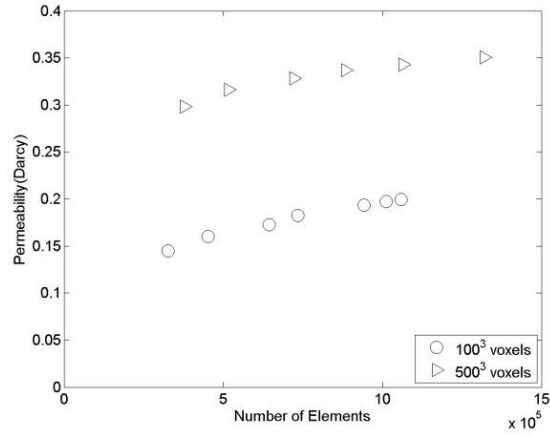
(a)
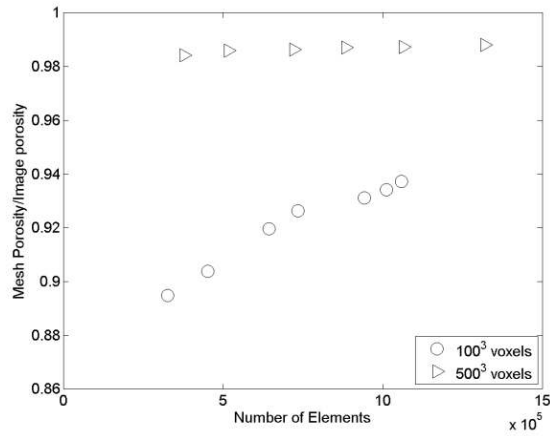
(b)
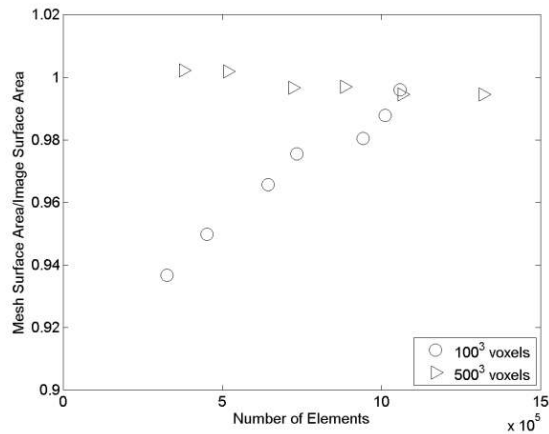
(c)

Figure 4-2: Structural and transport properties of the meshed packing for the 100^3 and 500^3 voxel images: (a) the permeability versus number of elements, (b) the porosities of the meshed structures to the image porosities versus number of elements, (c) the surface areas of the meshed structures relative to the image surface areas versus number of elements.

49

structure of this image. For the 100^3-voxel image, this is not the case and values are more sensitive to the number of elements. It can be also seen that even with a very large number of elements, we do not reach to the porosity of the original image. This is more severe for the 100^3-voxel image than for the 500^3-voxel image. Figure 4-2(c) depicts the calculated surface area of the mesh relative to the surface of the 100^3 and 500^3-voxel images. Relative surface area shows similar behavior as the relative porosity of the images. Therefore, unstructured meshes with around 1300K elements are used for all image resolutions to perform FEM simulations.

Permeability from LBM simulations using four different relaxation times and FEM simulations at all image resolutions are plotted in Figure 4-3. As can be seen from this figure, for the lower image resolutions, there are significant discrepancies among the permeability values between two approaches. The change in permeability with image resolution has opposite trends for these two approaches. FEM simulations show an increasing trend in permeability with increasing image resolution while LBM simulations are showing a decreasing trend. In LBM simulations, relaxation time affects the permeability results. Lower relaxation time results in higher permeability. Moreover, the rate of change of permeability is higher for the lower relaxation times. Both FEM and LBM simulations predict similar permeability values for the highest image resolution (two micron voxel size).

In order to quantify the effect of voxel size on LBM results, each voxel in the image with ten-micron resolution is divided by 2, 3, 4 and 5 times, so voxel sizes are 5, 3.333, 2.5 and 2 microns, and images are 200^3, 300^3, 400^3 and 500^3 voxels. It is important to point out this revoxlization process keeps pore structure fixed exactly as it is in the low-resolution image, which the grid resolution varies as it does when the image resolution is changed. The permeability value predicted from LBM simulations of all revoxelization images are plotted in
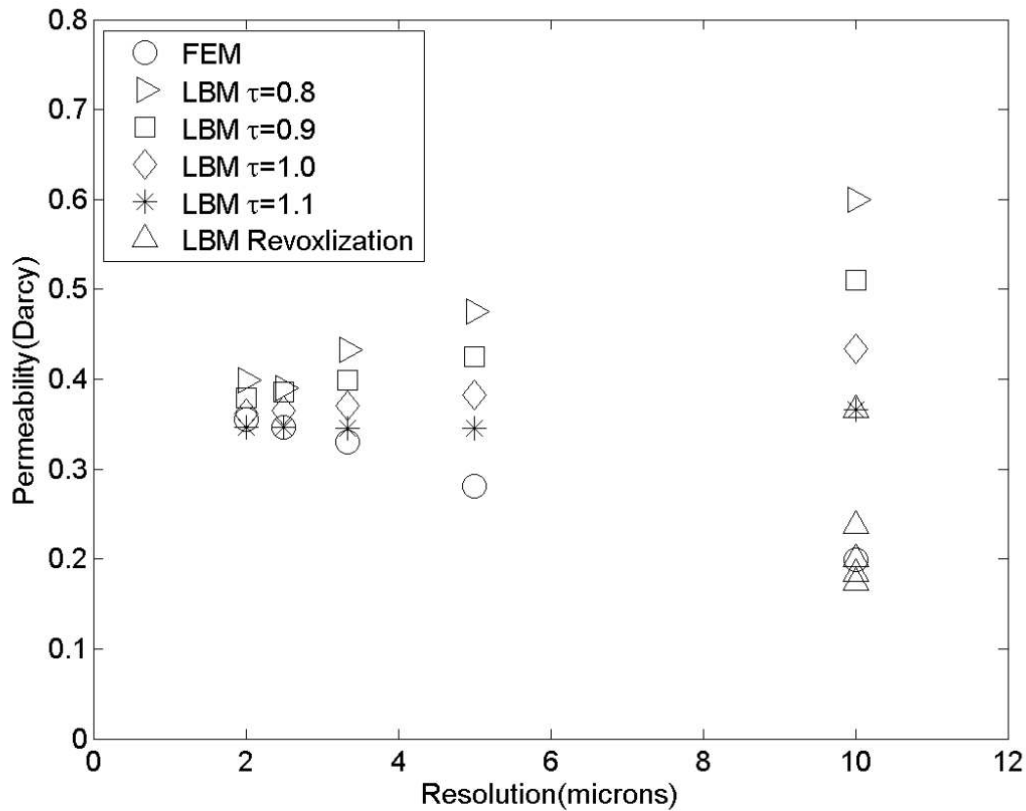
Figure 4-3: Permeability results of FEM and LBM for different image resolutions.

Figure 4-3. Reducing the voxel size decreases the predicted permeability. The rate of change of permeability is the highest when the voxel size is reduced from 10 to 5 microns. The variation of permeability is very small when the voxel size changed to 3.333, 2.5 and 2 microns, and these permeability values are very close to the one predicted from FEM simulations. Revoxlization helps to reduce the numerical errors associated with the voxel size in LBM simulations.

Figure 4-4 shows the pore structures of a sub-region in the 100^3 and 500^3-voxel images of packing. Due to the poor resolution in the 100^3-voxel image, there are lost pore connections that can reduce the estimated value of permeability. One can observe the differences in the numerical domain (characterized by the mesh) for these two images. The mesh conforms better to pores in

51
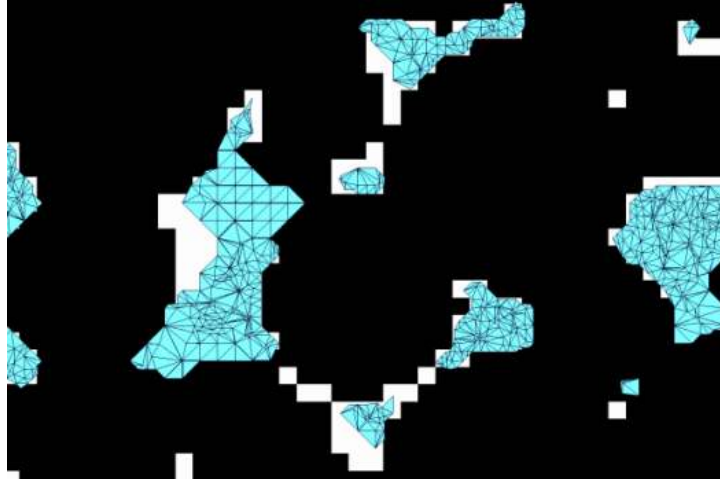
(a)
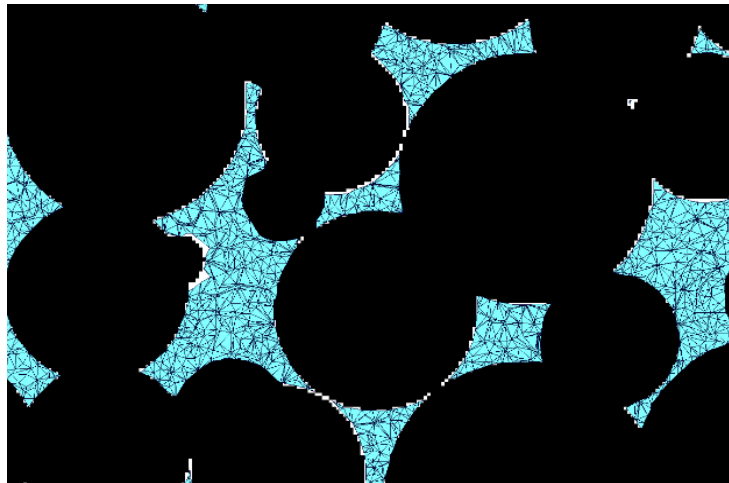
(b)

Figure 4-4: Two-dimensional cross-sections of the mesh with (a) 110K elements for100^3-voxel image and (b) 110K elements for 500^3-voxel image (white regions are the void space and black regions are the solid phase).

the high-resolution image (which also has smoother pore-grain interfaces compared to the lower-resolution image). It can also be seen that numerical domain in FEM underestimates the volume of the pores and the meshing is more likely to fail to preserve pore connectivity in poor resolution image. It can be seen that in the poor-resolution image, the number of the pores that

are connected to their neighboring pores with merely a single node is larger. LBM allows the flow of fluids through these shared nodes. In contrast, for FEM there cannot be flow between neighboring elements if the connect only at a node (no shared face). This may partly explain why permeability values predicted from these two methods have a large discrepancy for the low-resolution image.

4.2.2 Microscopic Velocity Field Comparison

Even though similar permeability values are predicted from FEM and LBM simulations in the 500^3-voxel image, the microscopic velocity field predicted from these two numerical approaches is compared. A point-by-point comparison of the pore-scale velocity fields from FEM and LBM is performed to quantify whether differences exist at the pore scale that may be averaged out in a continuum parameter such as permeability. FEM simulations produce velocity value at nodes in the tetrahedral elements; therefore velocity values from FEM simulations are interpolated using the shape functions to evaluate velocities at each lattice point in the LBM grid (or voxel in the image). Velocities at each point are then normalized by the average velocity in the domain. The normalized difference in the z-direction velocity at each lattice point (between LBM and FEM simulations) for the 500^3-voxel is calculated using:

$$\Delta v_{z,i} = \frac{v_{z,i}^{LBM}}{\left\langle v_z^{LBM} \right\rangle} - \frac{v_{z,i}^{FEM}}{\left\langle v_z^{FEM} \right\rangle} \tag{4-1}$$

where $\Delta v_{z,i}$ is the difference between the normalized calculated z-direction velocity of LBM and FEM for the grid i, $v_{z,i}^{LBM}$ and $v_{z,i}^{FEM}$ are the calculated z-direction velocities of LBM and FEM for the grid i, respectively, and $<v_z^{LBM}>$ and $<v_z^{FEM}>$ are the calculated average z-direction velocities for LBM and FEM, respectively. Figure 4-5 shows a plot of the z-direction velocity from FEM simulations, visualized on a xy cross-section of the 500^3-voxel image. Also shown is
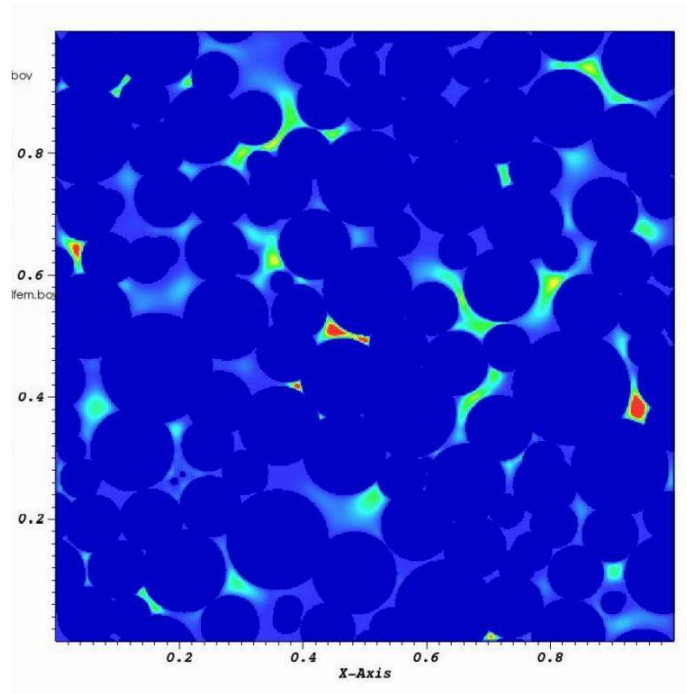
(a)
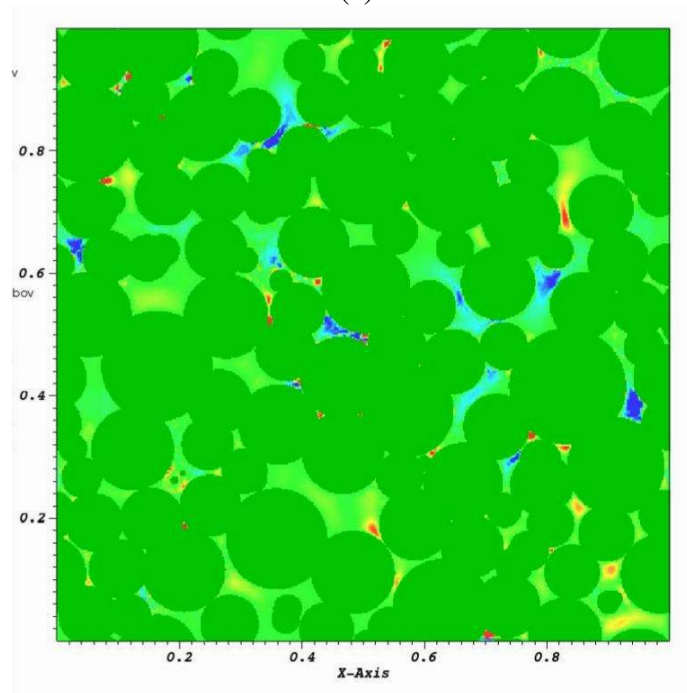
(b)

Figure 4-5: (a) *z*-direction velocity plot of the FEM simulations in a *xy* cross-section of the 500^3-voxel image and (b) its corresponding normalized difference values plot between the two numerical approaches LBM and FEM.

the normalized difference calculated from equation (4-1) plot. By inspecting these two plots, one can see that FEM calculates higher velocity values than LBM in regions with higher velocities.

Two pore areas in the 2D *xy* cross-section shown in Figure 4-6 are chosen to in order to compare the calculated velocity fields of FEM and LBM quantitatively. In the first area, normalized *z*-direction velocities of FEM and LBM along a horizontal line are plotted in Figure 4-6b. It shows that the differences between the velocities are higher at the regions away from the void-grain interfaces. At the center of the line where velocity reaches to its maximum value, predicted velocities of FEM are almost 11% higher than LBM. In the Figure 4-6d, normalized *z*-direction velocities of the two approaches are plotted along the vertical line shown in the Figure 4-6c. Contrary to Figure 4-6b, Figure 4-6d shows that LBM velocities are slightly higher than FEM. At the mid points on the line, predicted velocities of LBM are around 16% higher than FEM. It should be noted that the normalized velocity range in Figure 4-6b is higher than in Figure 4-6d. Figure 4-6b is in the high-velocity region where the velocity difference plot (Figure 4-5b) shows higher FEM values than LBM values. In studies with a focus on high velocity studies in porous media (such as non-Darcy flow) these regions may play a more significant role.

A more quantitative investigation of the velocity and difference fields is done in Figure 4-7 and Figure 4-8. Figure 4-7 is the histogram of difference values. The mean value of difference is zero and the standard deviation is 74%. The frequency of difference values between -0.75 and 0.75 is more than 96% of the total number of the nodes (it should be pointed out that more than 85% of the nodes are located in the solid phase). Histograms of the normalized *z*-direction velocities predicted from two methods for the 500^3-voxel image are shown in the Figure 4-8. FEM seems to predict higher velocity magnitudes (both in positive and negative directions) and shows a wider range of velocity values compared to LBM results. Permeability

values predicted from both approaches for this image are close to one another. Although the leading direction velocity ranges and magnitudes are different, they sum up to give similar values (since their summations are used for permeability calculations).

(a)

(b)

(c)

(d)
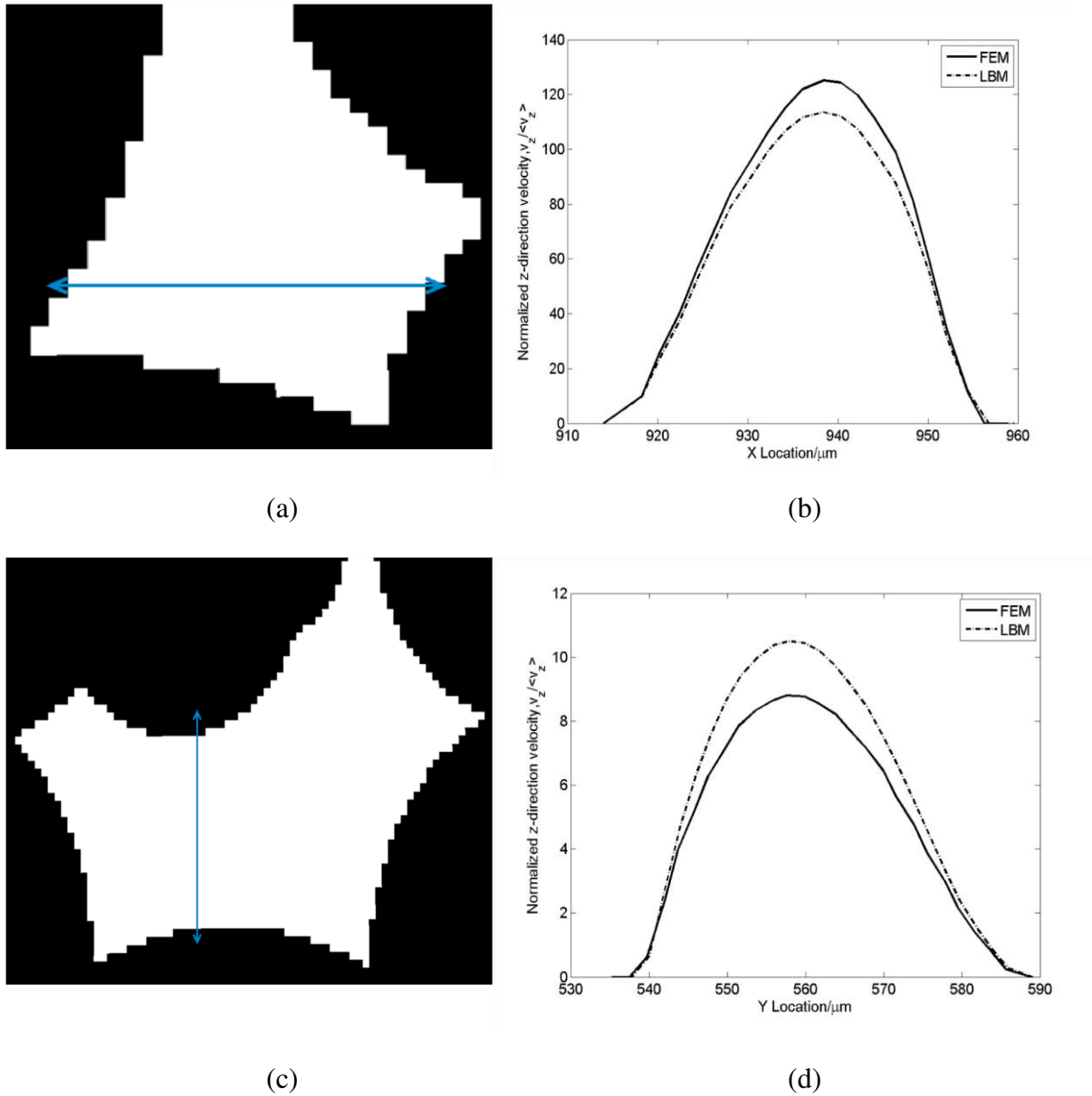
Figure 4-6: The predicted velocity profiles from LBM and FEM along the blue lines in two regions: (a) shows a region along with a horizontal blue line, (b) The velocity profile predicted from FEM and LBM along with blue line in (a), (c) shows a region along with a vertical line, (d) The velocity profile predicted from FEM and LBM along with blue line in (c).

56
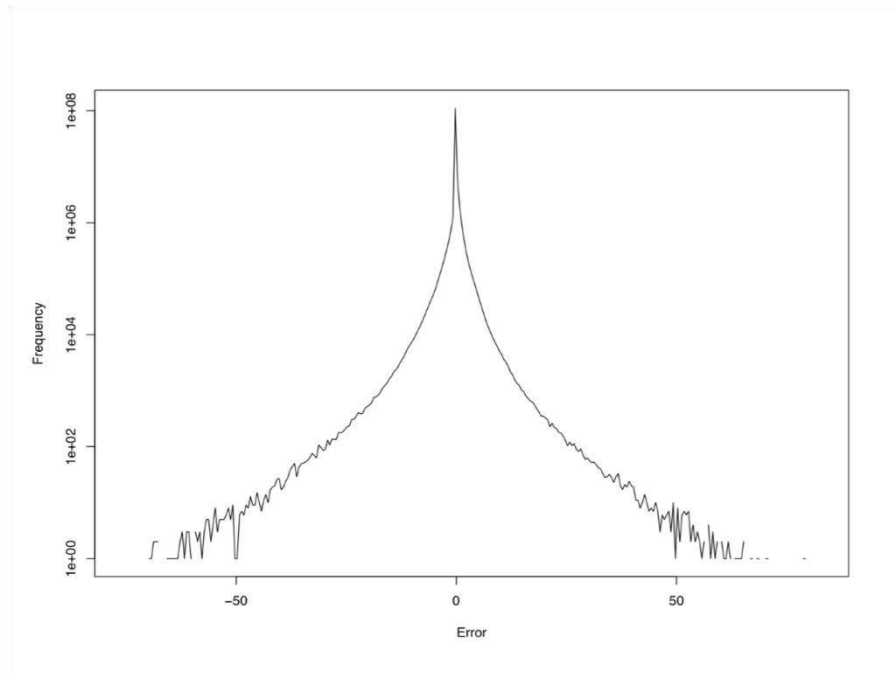
Figure 4-7: Histogram of difference of the normalized *z*-direction velocities between LBM and FEM in the 500^3-voxel image.
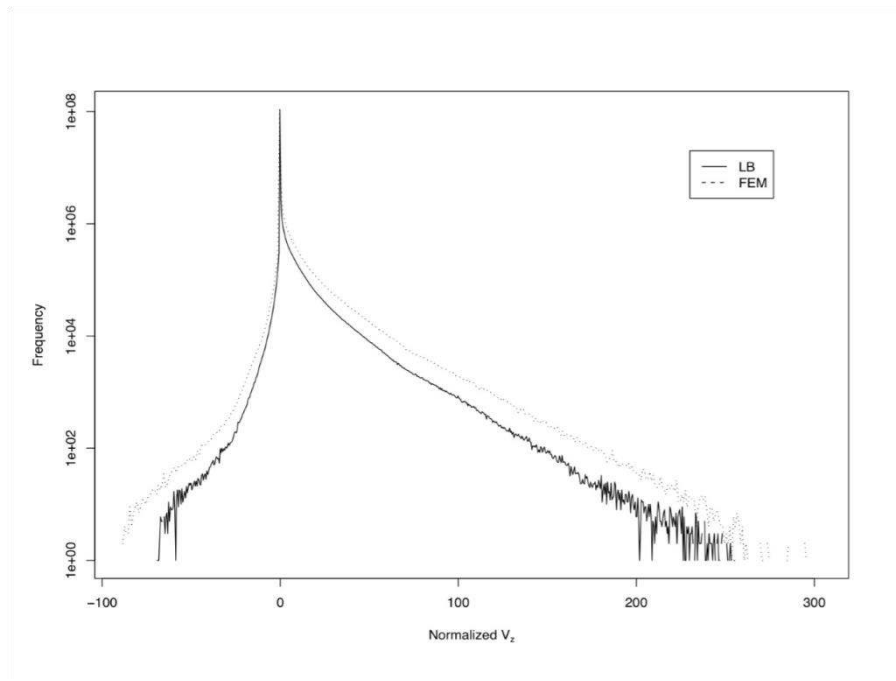
Figure 4-8: Predicted *z*-direction velocity histograms predicted from LBM and FEM in the 500^3-voxel image

5.   FEM Modeling of Non-Darcy Flow

Hydraulic fracturing with proppants has been used for many years to enhance extraction of oil and gas (C. Cooke, 1973; Graham & Kiel, 1968). In the past decade, advances in hydraulic fracturing and horizontal well techniques have enabled dramatic expansion of commercial shale gas production in North America (Hart, Sayers, & Jackson, 2011; Sondergeld, Newsham, Comisky, Rice, & Rai, 2010). Hydraulic fracturing is the process of injecting fluids at high pressure to fracture the producing rock and create high-conductivity flow paths from the source rock or reservoir to the well (Cipolla, 2009). Proppants are added to the fracturing fluid to prop the fracture open after the fracturing pressure is reduced. For the proppants to be effective it is essential that they maintain paths of high conductivity (Brannon, Wood, & Wheeler, 2006; Kaufman, Penny, & Paktinat, 2008; Warpinski, Mayerhofer, Vincent, Cipolla, & Lolon, 2008). Despite its widespread use, many aspects of the hydraulic fracturing process remain poorly understood. Research work has reported the adverse effects of neglecting non-Darcy flow on production prediction, fracture design, proppant selection, and well testing of hydraulic fractures. Quantifying the additional pressure drop caused by non-Darcy effects and understanding the inertial effects on flow behavior in hydraulic fracture is important.

Traditionally, flow experiments are conducted in a cell that contained proppants and rock to measure the permeability and non-Darcy flow coefficient. As loading stress increases in reservoirs, propped fractures are expected to have decreased permeability and increased non-Darcy coefficients. Different proppant materials have showed different behavior (rearrangement, embedment and particle crushing). The sieve analysis of proppants under stress by Stephen and David (2004) indicated that ceramic proppants tend to crush into larger pieces while sand crushed into smaller pieces. β was measured using proppants with various sizes and loading

stresses; results were correlated with standard deviation of sieve size distribution. C. E. Cooke (1973) developed a conductivity cell to measure the permeability of sand proppants. Loads were applied to the piston of a stainless steel cell that contained proppants. In the pressure range investigated (1k to 10k psi), permeability was reduced two orders of magnitude for 8-12 sand proppants and by around 80% for 20-40 sand proppants. Different sizes of sand with equal permeability had different non-Darcy coefficients and this was attributed to the larger proppants being more heterogeneous after crushing. Much and Penny (1987) used a similar setup to measure the conductivity of sand proppants and intermediate strength ceramic proppants (ISP). The same pressure range (1k to 10k psi) was studied and results showed a significant decrease in conductivity (>50%) for Jordan sand proppants, whereas the conductivity of ISP decreased by approximately 30%. Fredd et al. (2001) observed that Jordan sand proppants started to crush after 2k psi whereas sintered bauxite proppants kept intact until 5k psi. The bauxite conductivity decreased from 2000 mD·ft to 10 mD·ft and Jordan sand had a reduction from 400 mD·ft to 0.35 mD·ft in the stress range of 1k to 7k psi.

In addition to proppant characteristics, the type of column wall used in conductivity cells is also important. Much and Penny (1987) showed different conductivity using steel pistons and sandstone cores. At lower loading stress, no crushing and embedding happened and proppant conductivity for the steel pistons was higher. This was attributed to the steel which caused an overestimate of proppant conductivity. Embedding becomes important for loading stress of 8k psi and higher for sandstone cores. Research done by Wen, Zhang, Wang, Liu, and Li (2007) showed that conductivity stayed the same for steel and sandstone boundaries at loading less than 5k psi, while the conductivity using sandstone cores declined more rapidly than with steel

pistons at larger pressures. The use of rocks as column walls better represents the actual fracture-proppant system and allows one to observe any potential wall effects.

In this work, image-based pore-scale models is used to evaluate the permeability, non-Darcy flow coefficient, and microscopic flow behavior in bulk proppants between berea walls and single-layer proppants between shale walls. Multilayer proppants packing sandwiched by berea sandstone is composed of the berea system and monolayer proppant sandwiched by shale is composed of the shale system.3D microCT images of berea-proppant-berea and shale-proppant-shale system are acquired and segmented by Paula Sanematsu and Clinton S. Willson. Different loading stresses are applied on two systems while imaged. Pore-Scale FEM simulations at the both Darcy flow and non-Darcy flow regime are conducted using the segmented images of proppant systems. Two elements type P1P1 and P2P1 are compared in FEM simulations. The loading stress effects on pore structures as well as transport properties tortuosity, permeability and non-Darcy coefficient are studied. The pore-scale flow fields from images at different loading stresses are visualized. Inertial effects on pore-scale velocity fields are also investigated to improve fundamental understanding of non-Darcy flow behavior.

5.1 Materials

5.1.1 Image Acquisition

Two different rocks are used for this study: Berea sandstone and Pierre shale. Small cores, 6 mm in diameter, and various heights, are extracted from 1-in Berea sandstone and Pierre shale cores. Proppants used in the imaging were CarboHPS® high-strength sintered bauxite proppants from Carbo Ceramics. 20-40 sieve proppants with a median particle diameter of 697 μm are used with the Berea samples and 30-60 sieve proppants with a mean particle diameter of 430 μm are used with the shale. The material used to contain the system is a plastic that is

transparent to x-ray and not susceptible to deformations for the loadings applied in this study. In the following we will refer to the two different setups: either the Berea system, which is bulk proppant (multiple particle diameters) sandwiched between the Berea cores, or the shale system, which is a monolayer of proppant particles sandwiched between shale cores.

The sample holder consists of an outer cylindrical plastic sleeve that is transparent to x-rays and strong enough to support the stresses with little or no deformation (Figure 5-1). For the Berea system (Figure 5-1a), only one sleeve (inner diameter: 6 mm, outer diameter: 10 mm) is used. Steel anvils, used to apply the load to the rock-proppant-rock sample, are 6 mm in diameter, 2 mm in height. For the shale system (Figure 5-1b), two sleeves are used (inner diameters: 6, 10 mm; outer diameter: 10, 20 mm, respectively) to allow more stability for the stepped anvils. The rocks and proppant are packed by first placing a layer of rock on the lower anvil, then the proppants are placed while using a microscope to ensure a monolayer (i.e. proppants are not sitting on top of proppants) and finally another layer of rock is inserted on top.
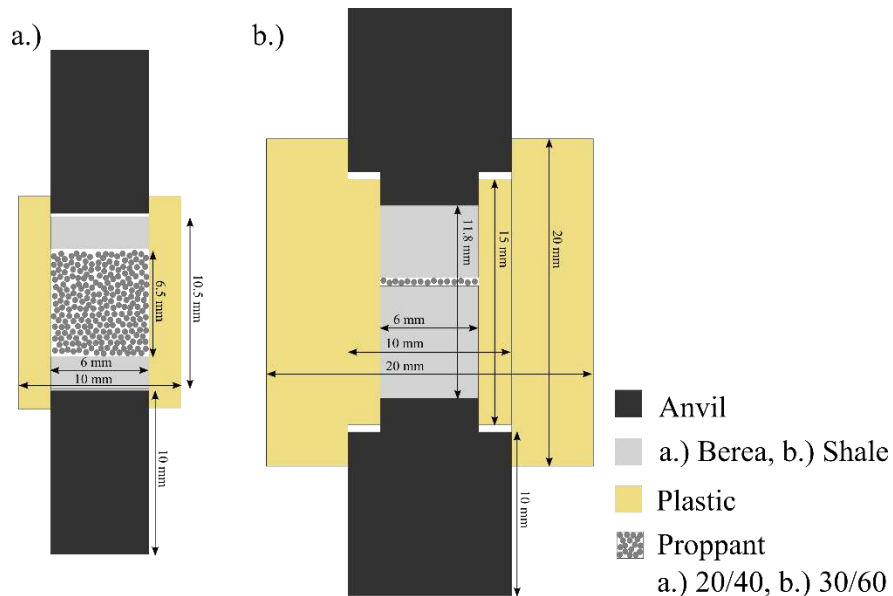
Figure 5-1: Schematic drawing of X-ray CT imaging experiment setup for (a) Berea and (b) Shale.

The samples are placed at the Advanced Photon Source GSECARS Large Volume Press (Wang et al., 2005) in the 13-BMD beamline. Table 5-1 reports imaging details for all loading stresses. For each system, the first image is obtained at zero applied stress on the proppants. Then, a load is applied and, once stabilized, the entire system is imaged again. Both systems are imaged at 0, 4k, 8k, and 12k psi. The Berea system is also imaged at 20k psi.

Table 5-1: X-ray Micro-CT imaging details

Imaging Details	Berea	Shale
Voxel Resolution (μm)	11.08	12.00
Energy (keV)	37.00	35
Exposure (s)	0.3	0.2
Rotations	720	720
Subvolumes scanned per load	2	3

5.1.2 Image Segmentation

Image reconstruction, the process of converting 2D projection images into a 3D volumetric file, is performed using filtered back-projection algorithms developed by GSECARS (Rivers, http://cars9.uchicago.edu/gsecars/index.html). Each voxel in the 3D volumetric data file (695x695x520 voxels) contains a linear attenuation value that depends upon the composition of the phases within the voxel and the x-ray energy. The voxel sizes of the reconstructed images were 11.8 μm for the Berea system and 12.0 μm for the shale system.

The resulting 3D datasets are first converted to 8 bit data and then smoothed by anisotropic diffusion (AD) filter (P. Bhattad, 2010) then segmented using an indicator kriging (IK) based technique first developed by Oh and Lindquist (1999) and then modified as described in (P. Bhattad, 2010). Each segmentation trial is evaluated both quantitatively (e.g., porosity) and qualitatively (i.e., comparison of segmented image to the original grayscale) to select the final segmented image to be used for further analysis. Finally, an algorithm (remove islands and

holes) was applied to remove isolated specks of noise. This process is illustrated for the Berea system at 0 psi loading in Figure 5-2.
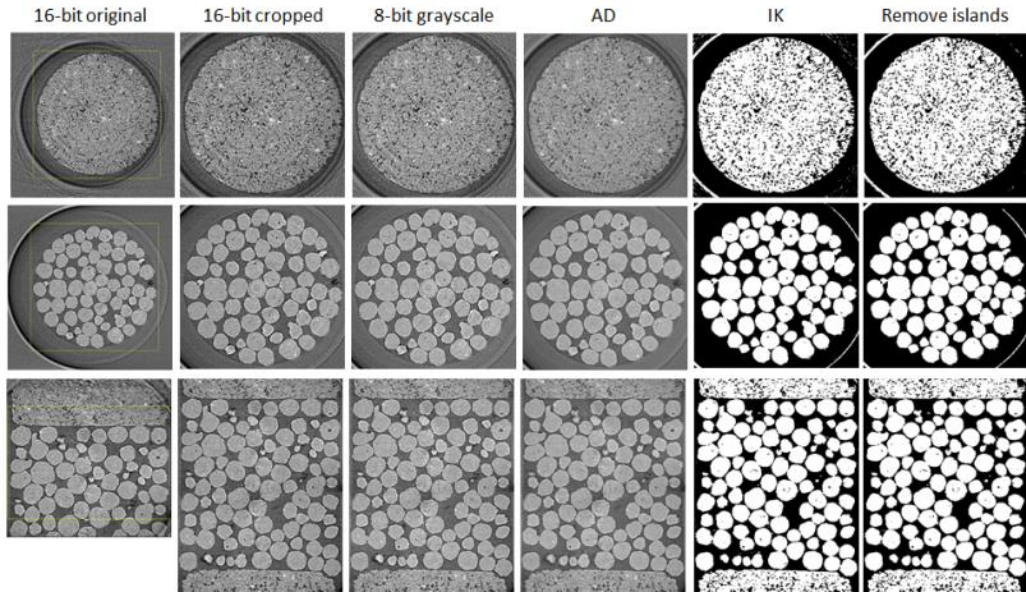
Figure 5-2: Image processing steps of the berea system at 0-psi loading stress

5.2 Results and Discussions

5.2.1 Stress Effects on Pore Structures

2D slices of segmented images of the berea and shale system are shown in Figure 5-3 and Figure 5-4 respectively at all loading stresses. Segmented images of the berea system (Figure 5-3) show that as loading stress increases, proppants rearrange, embed into the rock and eventually crush at the highest stresses. The rearrangement of proppants particles causes changes in the pore space, which in turn modifies flow pathways and increases the number of grain-grain contacts and tortuosity. Crushing occurs at 12k and 20k psi, thus increasing the number of particles, creating more surface area and reducing porosity. Embedment is first observed at 8k psi and embedment of proppants into the rock reduces the impact of near-wall packing structures that occur in rigid-wall systems.

Segmented images of the shale system (Figure 5-4) shows rock walls change little from 0 to 4k psi, however, these is considerable embedment of proppants happens from 4k to 12k psi. The pathways between proppants and the wall are narrowed or closed after embedment. Another important consequence of embedding is the reduction of fracture width, which decreases the fracture conductivity.
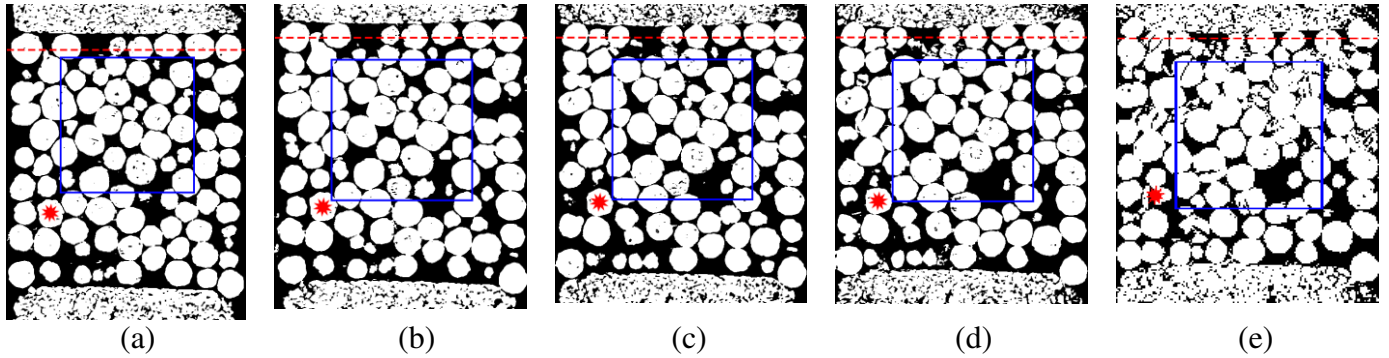
Figure 5-3: *yz* slice of the berea system segmented XCT image at loading stresses: (a) 0 psi, (b) 4k psi, (c) 8k psi, (d) 12k psi, (e) 20k psi.
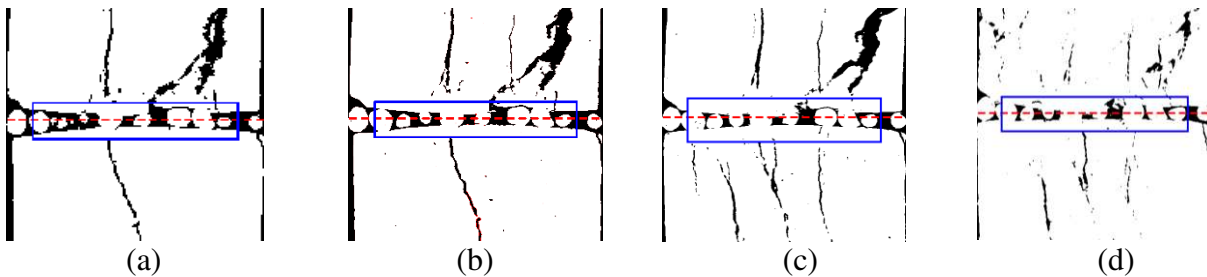
Figure 5-4: *yz* slices of the shale system segmented XCT image at loading stresses: (a) 0 psi, (b) 4k psi, (c) 8k psi, (d) 12k psi.

5.2.2 Elements Type Effects

Two different types of tetrahedral elements P2P1 and P1P1 are compared in FEM simulations using commercial software COMSOL. FEM simulations using P2P1 and P1P1 element are performed in the bulk proppants packing domain from the berea system with *z-*

direction flow. A 300^3-voxel subsection of the bulk proppant is extracted and the cutout can be seen for each loading in Figure 5-3, where the blue squares indicate the cubic cutouts of berea system.

In the FEM algorithm, the most time-consuming and memory-demanding step is solution of the linear system of equations for velocity and pressure. Therefore, the performance scales strongly with the number of equations in the linear system, which in turn is affected by element type. Compared to P1P1 elements, the P2P1 elements contain middle nodes that are additional velocity nodes. This significantly increases the degrees of freedom in the linear system of equations, thus affecting memory requirements and computational time. Table 5-2 lists number of equations and associated memory for P1P1 and P2P1 formulations for two different meshes. For the same number of elements, the degrees of freedom for the P2P1 elements is roughly five times larger and the memory requirements are approximately 8 times larger than with P1P1.

Table 5-2: Computational cost of P2P1 and P1P1 elements

Elements Number	Elements per Voxel	Elements Type	Degrees of Freedom	Memory Usage (GB)
351762	0.013	P1P1	368300	1.7
351762	0.013	P2P1	1905719	13.5
519849	0.019	P1P1	525668	2.5
519849	0.019	P2P1	2752757	22.1

To make efficient use of computational resources, it is important to minimize the number of elements while still capturing the void structure and maintaining accuracy, especially for P2P1 elements. Around 0.02 elements per voxel were used in P2P1 simulations of samples for all loadings based on numerical convergence with additional mesh refinement. For P1P1 simulations around 0.06 elements per voxel were used. As expected, results showed that fewer elements (for the same void structure) are required for convergence with P2P1 elements compared with P1P1 elements.

The comparison of element type is shown using the zero stress loading as an example. Figure 5-5 is a plot of apparent permeability as a function of Reynolds number obtained from P2P1 and P1P1 simulations. The characteristic length used to calculate Reynolds number is $d_p = 697$ μm in the proppant packing from Berea system and $d_p = 430$ μm in the shale system. Both values are reported by the manufacturer. It indicates that both the P2P1 and P1P1 results predict the onset of the non-Darcy flow regime at $Re \approx 1$, which is in agreement with the work reported by Huang and Ayoub (2008). The apparent permeability predicted from P2P1 results is approximately 30% higher compared to P1P1. Furthermore, the P2P1 results failed to converge at $Re \approx 20$, which is significant lower than the limit for P1P1 simulations ($Re \approx 100$).

Figure 5-5: Apparent permeability at different Reynolds number obtained from FEM P2P1 and P1P1 of 300^3-voxel bulk proppants from Berea system at zero loading stress.

Figure 5-6 contains the Forchheimer results from both P2P1 and P1P1simulations. The value of β predicted from P2P1 results is approximately half of what is predicted from P1P1

results, suggesting that the numerical differences associated with element type are more pronounced in the inertial flow regime than for Darcy permeability.
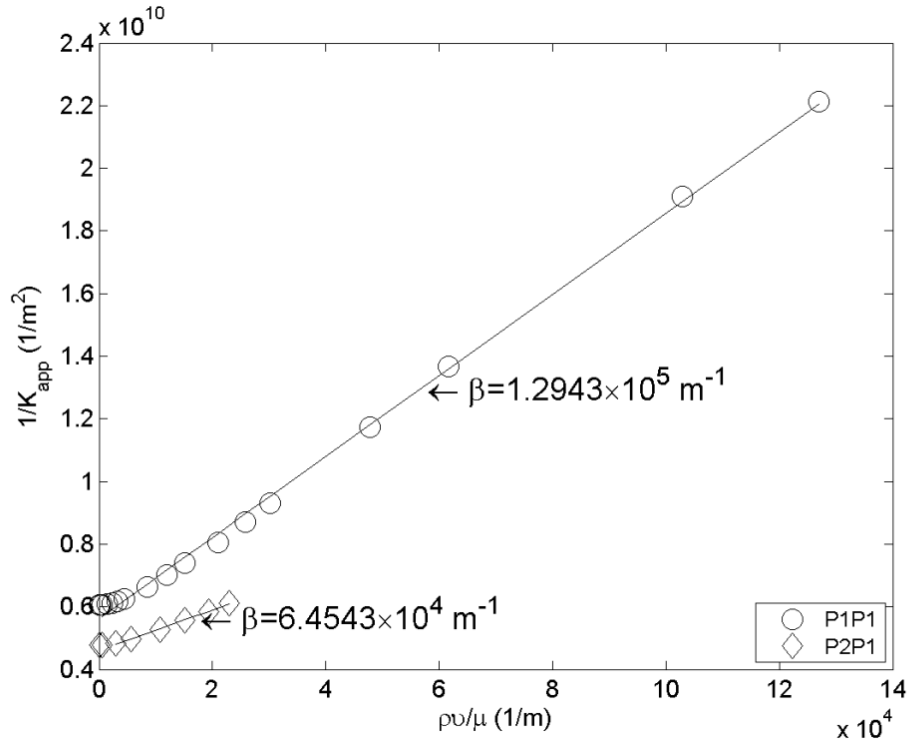
Figure 5-6: Forchheimer plot of 300^3-voxel bulk proppants at zero loading stress from FEM P2P1 and P1P1 simulations. The value β = 1.2943e-05 m^{-1} is predicted from the slope of the linear fit of the data from P1P1 and β = 6.4543e-04 m^{-1} is predicted from the slope of the linear fit of the data from P2P1.

The apparent permeability predicted from P2P1 results at all loading stresses (plotted in Figure 5-7) shows that the convergence limit for the 20k psi loading occurs at only at $Re \approx 5$. We believe this is caused by crushing of the proppant, which results in significantly smaller pore spaces, which have reduced numerical resolution (number of elements for a given gap size).

The velocity fields in the pore space predicted by P2P1 and P1P1 are also compared. Figure 5-8 indicates that both P2P1 and P1P1 predict qualitatively similar velocity fields for the same Reynolds number. The small differences that are observable include slightly higher velocity magnitudes for the P2P1 results. Quantitatively, (Lane, 2011) demonstrated that P2P1
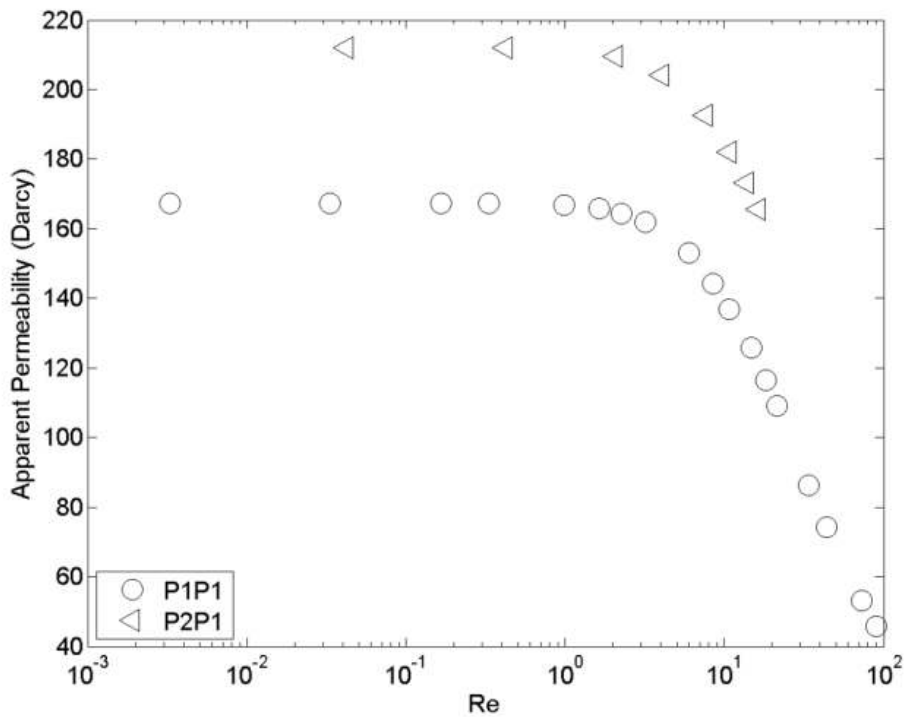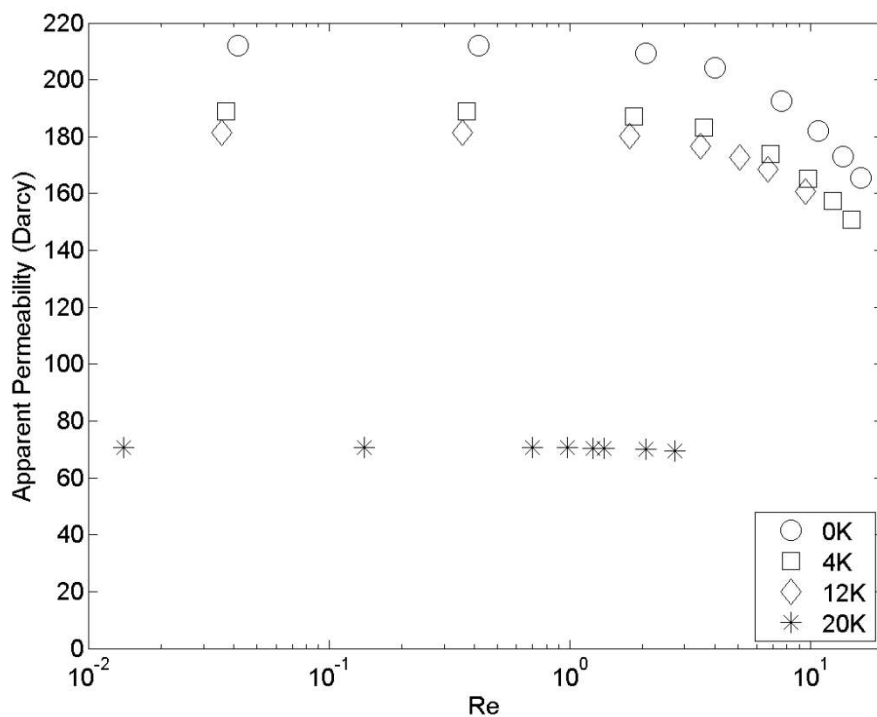
Figure 5-7: Apparent permeability at different Reynolds number obtained from FEM P2P1 of 300^3-voxel bulk proppants at 0, 4k, 12k and 20k psi loading stresses.

(a) (b)
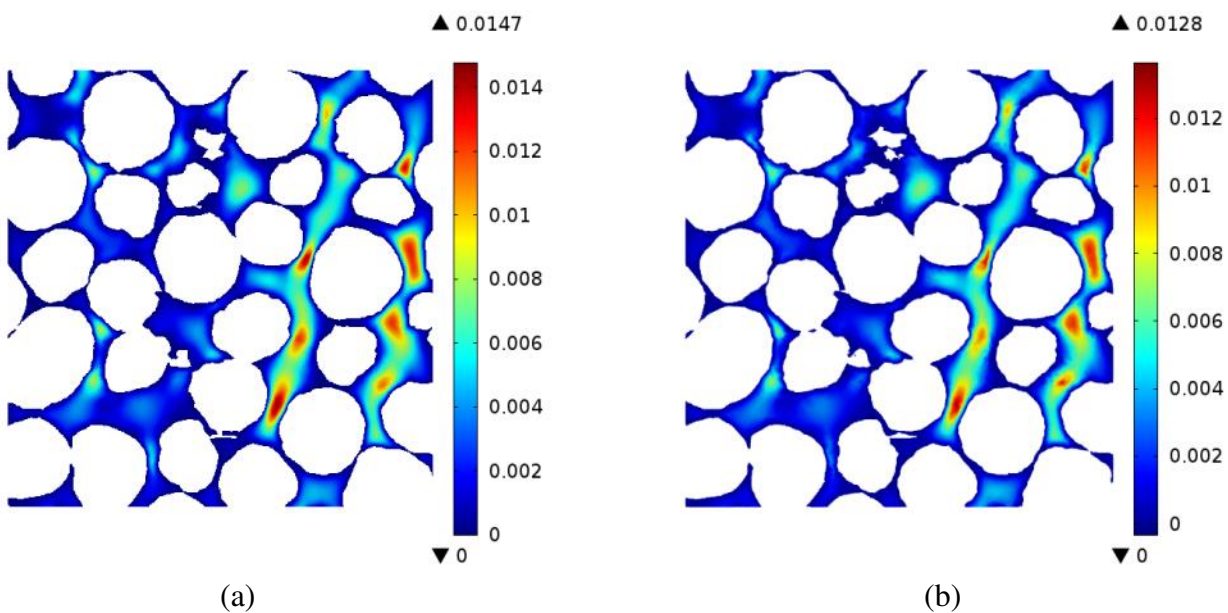
Figure 5-8: yz slice of velocity field at $Re \approx 0.3$ obtained from (a) FEM P2P1 (b) FEM P1P1 of 300^3-voxel bulk proppants at zero loading stress.

elements provide more accurate solutions for confined viscous flow by comparing computational versus analytical velocity fields in a square duct. We expect similar behavior to occur in the more complex interconnected pore spaces shown here. Hence, the FEM results for intrinsic permeability and non-Darcy flow coefficients reported in the following sections are obtained using P2P1 elements.

A close inspection of Figure 5-7 demonstrates that no linear relationship is found for $Re > 1$ at 12k psi and 20k psi loading in the bulk proppants. In order to correctly predict β from linear regression, it is necessary to obtain data at higher Reynolds numbers, which requires mesh refinement. Due to computational limitations and reasonable insensitivity of simulation results to domain size in this range, a 200^3-voxel domain is used for the refined simulations. The apparent permeability versus Reynolds number plot predicted from two mesh resolutions, shown in Figure 5-9, indicates that the convergence limit increased from $Re \approx 10$ to 40 as mesh resolution increased from 0.02 elements per voxel to 0.06 elements per voxel.

In order to check accuracy of the non-Darcy coefficients predicted from linear regression, a convergence analysis for β prediction is conducted. Table 5-3 shows an example for proppants at 12k psi loading stress: 13 simulation cases with various Re are performed and $1/k_{app}$ and $\rho v/\mu$ data are obtained from each simulation. Table 5-4 lists β predicted from regression of different data points. Three data points are used in each regression prediction. The difference of β predicted from regression of points (9, 10, 11), (10, 11, 12) and (11, 12, 13) are less than 1%, suggesting that the non-Darcy coefficient changes only slightly provided that higher Reynolds number data are included, and that the results reported here have converged with respect to Reynolds number.

69
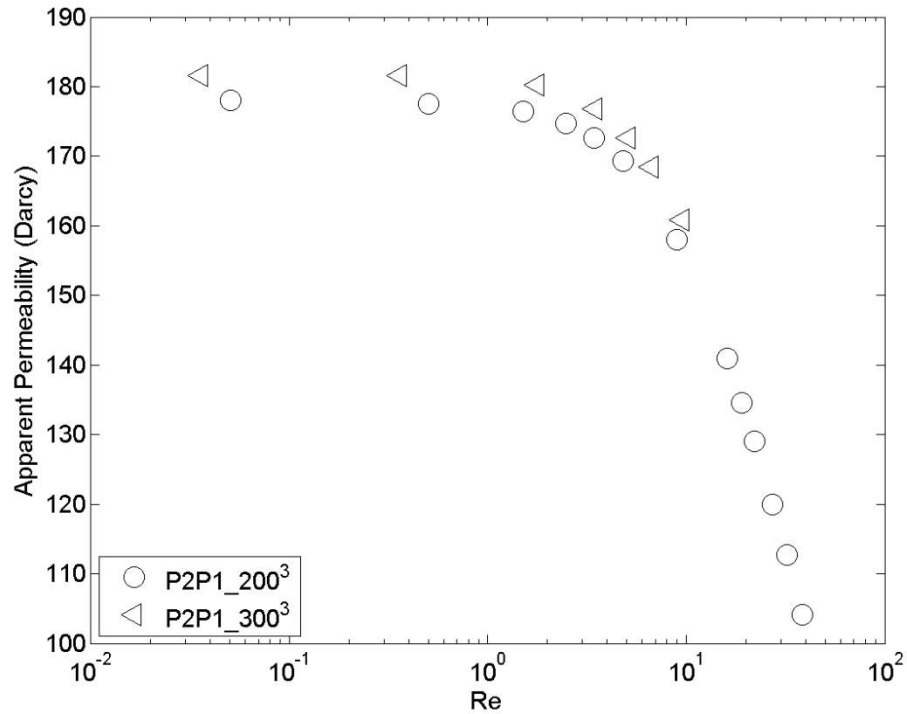
Figure 5-9: Bulk proppant apparent permeability at 12k psi for different Reynolds numbers obtained from FEM P2P1 for two cutouts: 300^3-voxel and 200^3-voxel.

Table 5-3: $1/k_{app}$ and $\rho v/\mu$ obtained from FEM P2P1 simulations with 13 cases of various Re of 200^3-voxel bulk proppants at 12k psi loading

Case	$\rho v/\mu$ (m)	$1/k_{app}$ (m^{-2})	Re
1	7.1406E+01	5.6934E+09	0.050555
2	7.1248E+02	5.7060E+09	0.504437
3	2.1231E+03	5.7446E+09	1.503147
4	3.5049E+03	5.7997E+09	2.481443
5	4.8496E+03	5.8681E+09	3.43349
6	6.7921E+03	5.9855E+09	4.808814
7	1.2677E+04	6.4141E+09	8.97503
8	2.2626E+04	7.1873E+09	16.01897
9	2.6991E+04	7.5312E+09	19.10936
10	3.1060E+04	7.8533E+09	21.99051
11	3.8502E+04	8.4471E+09	27.25961
12	4.5229E+04	8.9885E+09	32.02227
13	5.4329E+04	9.7279E+09	38.46472

Table 5-4: β predicted from different linear regression cases from data points in Table 5-3.

Case	Points Used	Re Range	β (m^{-1})	R^2	β Relative Difference (%)
1	6,7,8	4.80-16.01	7.61E+04	0.99971	N/A
2	7,8,9	8.97-19.10	7.80E+04	1	2.431174
3	8,9,10	16.01-21.99	7.90E+04	1	1.243526
4	9,10,11	19.10-27.25	7.96E+04	1	0.786482
5	10,11,12	21.99-32.02	8.01E+04	1	0.640385
6	11,12,13	27.25-38.46	8.09E+04	1	1.034035

5.2.3 Proppant Packing: Stress Effects

The intrinsic permeability calculated from the bulk proppant images is referred to as the

bulk permeability. From Figure 5-10, the bulk permeability value predicted from FEM P2P1 at
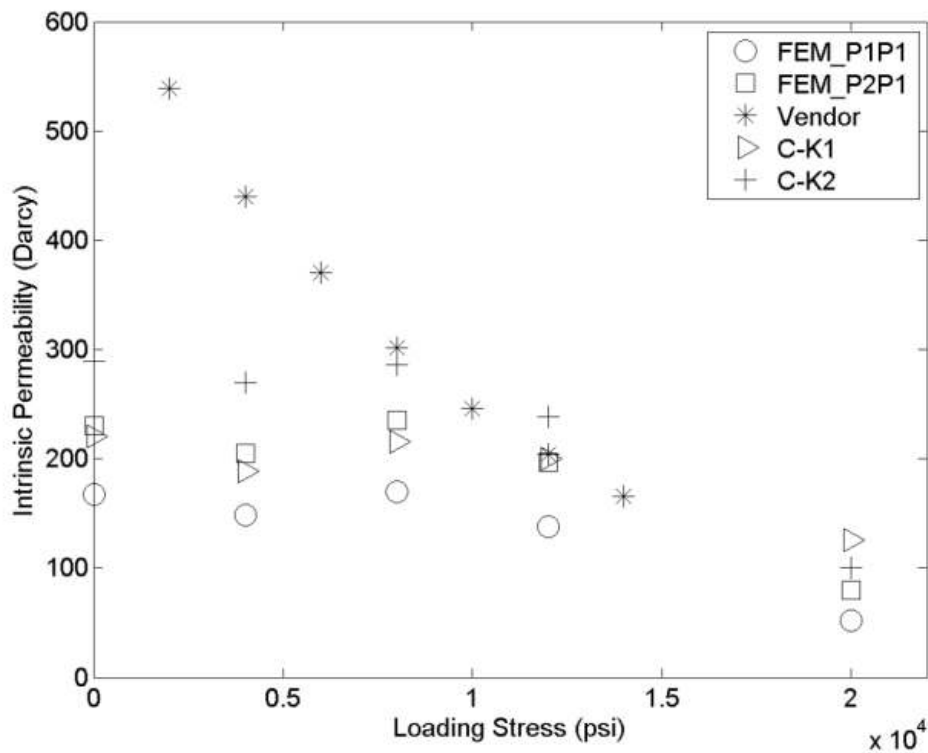
Figure 5-10: Intrinsic permeability of 300^3-voxel bulk proppants at different loading stresses predicted from FEM P1P1, FEM P2P1, empirical C-K1 equation (5-2) and C-K2 equation (5-3) and published by proppants manufactures CARBO Ceramics (Palisch, Duenckel, Bazan, Heidt, & Turk, 2007).

each loading stress indicates that from 0 to 8k psi loading, the permeability remains constant at approximately 225 Darcy. Minor rearrangements and embedding of proppants can be observed from the images between 0 and 8k psi, but these changes have only a minor effect on permeability. A 12% decline of permeability occurs from 8k to 12k psi, when crushing first begins to occur. A decline of 60% then occurs between 12k and 20k psi, when significant crushing occurred. The bulk permeability values obtained by simulations were compared with Modified API RP-61 (ISO 13503-3) experimental results published by CARBO Ceramics (Figure 5-10), the manufacturer of the proppants (Palisch et al., 2007). Their results are significantly different, showing a smooth, monotonic decrease in permeability as loading stress increases from 0 to 14k psi.

Permeability is closely related to pore structure, and image analysis can be used to characterize pore structure changes as loading increases, giving additional insight into the fundamental cause of permeability reduction. Porosity is computed as the ratio of void voxels to total voxels in the segmented image. Tortuosity is defined as the ratio of the length of the actual path of fluid motion to the linear distance traversed in the direction of the mean flow. A. Koponen, Kataja, and Timonen (1996) proposed the tortuosity can be calculated based on velocity values on grid points:

$$\tau = \frac{\sum_{i,j,k} u_{mag}(i,j,k)}{\sum_{i,j,k} |u_z(i,j,k)|} \tag{5-1}$$

where $u_{mag}(i, j, k)$ is the magnitude of velocity at location i, j, k, $u_z(i, j, k)$ is the z-direction (flow direction) velocity at location i, j, k and i, j, k is the location of a lattice point in the domain.

Table 5-5 lists the intrinsic permeability, porosity and tortuosity values for all loadings. From 0 to 8k psi, structural parameters porosity and tortuosity as well as permeability remain

Table 5-5: Porosity, tortuosity and intrinsic permeability value of 300^3-voxel bulk proppants packing at all loading stresses

Loading Stress (psi)	Porosity	Tortuosity	Permeability (Darcy)
0	0.33	1.26	230.43
4k	0.31	1.27	205.37
8k	0.32	1.26	235.65
12k	0.32	1.27	197.07
20k	0.28	1.36	79.73

relatively constant. At 12k psi, small crushing does not cause much change in porosity and tortuosity. At 20k psi, significant particle crushing causes tortuosity to increase approximately 5% and porosity to decrease around 25%.

Additional insight is gained by computing expected permeabilities using the Carman-Kozeny (C-K) equation, which is an empirical equation widely used to predict the permeability of sphere packing and other granular materials. Here it is expressed in two different forms as follows (Bear, 2013):

$$k = \frac{d_p^{\,2}\phi^3}{180(1-\phi)^2} \tag{5-2}$$

where d_p = 697 μm is the median particle diameter reported by the manufacturer and ϕ is the porosity (from Table 5-5).

The second form incorporates tortuosity (Wyllie & Spangler, 1952):

$$k = \frac{R_H^{\,2}\phi}{k_0\tau^2} \tag{5-3}$$

where R_H is the hydraulic radius, the ratio of void volume and surface area, k_0 is the shape factor of 2.5 and τ is the tortuosity (from Table 5-5).

Figure 5-10 shows that as loading stress increased from 0 to 12k psi, the discrepancy of permeability predicted from pore-scale simulations (FEM P2P1) and the C-K equation (5-2) was only ±8%. A larger discrepancy of 37% was observed at 20k psi, likely because the significant crushing causes the proppants packing to no longer resemble a uniform sphere packing. The

permeability predicted from C-K equation (5-3) is approximately 25% larger than values from pore-scale simulations.

Image-based pore-scale simulations also provide visual insights about how flow paths are modified as pore structures changes. Figure 5-11 shows, for each loading stress, the magnitude of velocity normalized by its maximum value in the middle *yz* cross sections of the domain. At lower loadings, there are wide-open pore spaces where particles are not packed tightly, and velocities are generally high in these spaces. As loading increases, the pore space becomes more compact and the velocity magnitude becomes more uniform throughout.

(a)   (b)

Figure 5-11: *yz* slices of velocity field normalized by its peak value obtained from FEM P2P1 of 300^3-voxel bulk proppants at loading stress: (a) 0 psi, (b) 4k psi. (continued)

Figure 5-11: (continued) *yz* slices of velocity field normalized by its peak value obtained from FEM P2P1 of 300^3-voxel bulk proppants at loading stress: (c) 8k psi, (d) 12k psi and (e) 20k psi.

Not surprisingly, the non-Darcy flow coefficient showed the opposite trend as bulk permeability, increasing with the increased loading stresses over the range where the pore structure was impacted. As shown in Figure 5-12, an average value 7.0×10^{-4} is observed from 0

to 8k psi. A small increase (10%) occurred from 8k psi to 12k psi and a significant increase (40%) occurred from 12k psi to 20k psi. In contrast, vendor results showed an almost linear trend versus the loading stress and the actual values of β were significantly lower than what is predicted from simulations.
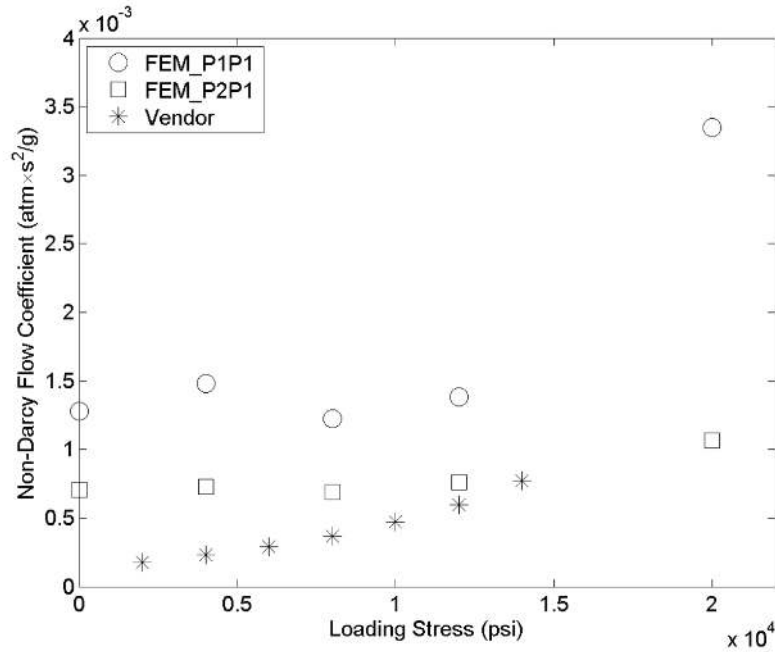
Figure 5-12: Non-Darcy flow coefficient of 200^3-voxel bulk proppants at different loading stresses predicted from FEM P1P1, FEM P2P1 and published by proppants manufactures CARBO Ceramics (Palisch et al., 2007).

In the non-Darcy flow regime, inertial effects cause a decrease in apparent permeability as Reynolds number increases. The pore-level changes caused by the onset of inertial flow are investigated by comparing velocity fields for different Reynolds numbers in Darcy and non-Darcy regimes. In Figure 5-13, velocity is scaled relative to its peak value, so a comparative study can be performed. The velocity fields at four different Reynolds numbers are compared. At low Reynolds number ($Re = 0.041$), viscous forces dominate momentum transport and the velocity increases symmetrically (in versus out) when flowing through narrower throats. As the

76

Reynolds number increases to 4.02, inertial effects start to become significant and fluid flow exhibits slightly more jet-like behavior, penetrating throats without changing velocity significantly and remaining high even after exiting pore throats into larger pore bodies. This behavior is even more evident at Reynolds numbers equal to 10.76 and 16.30.
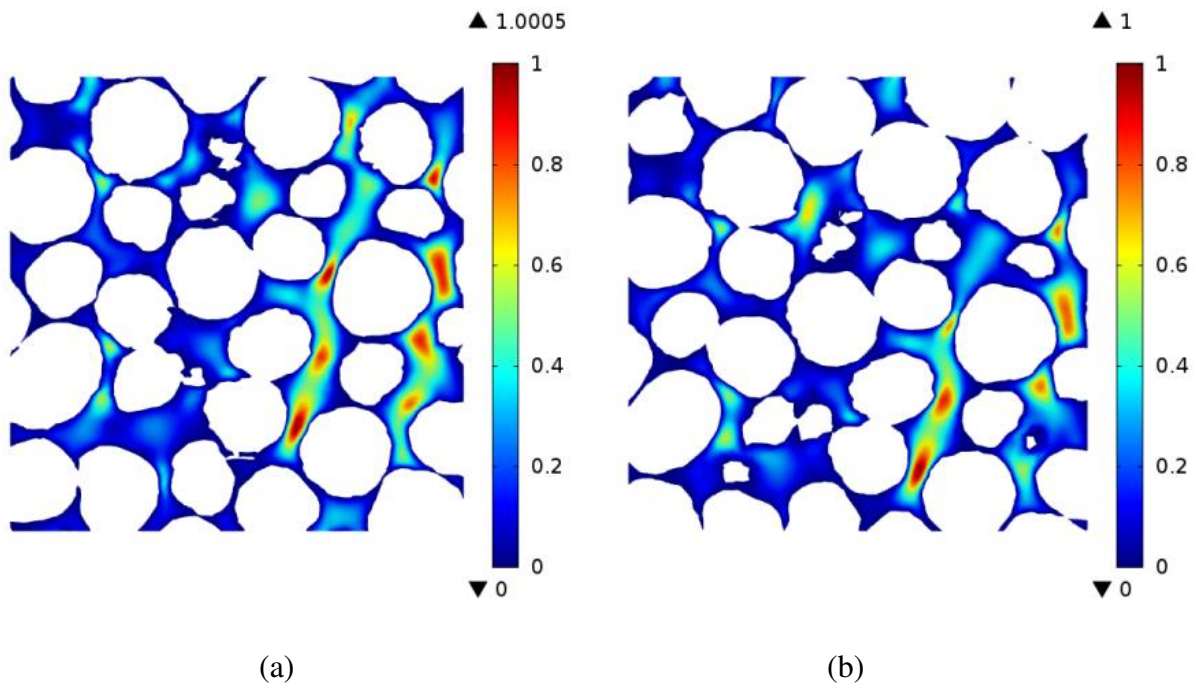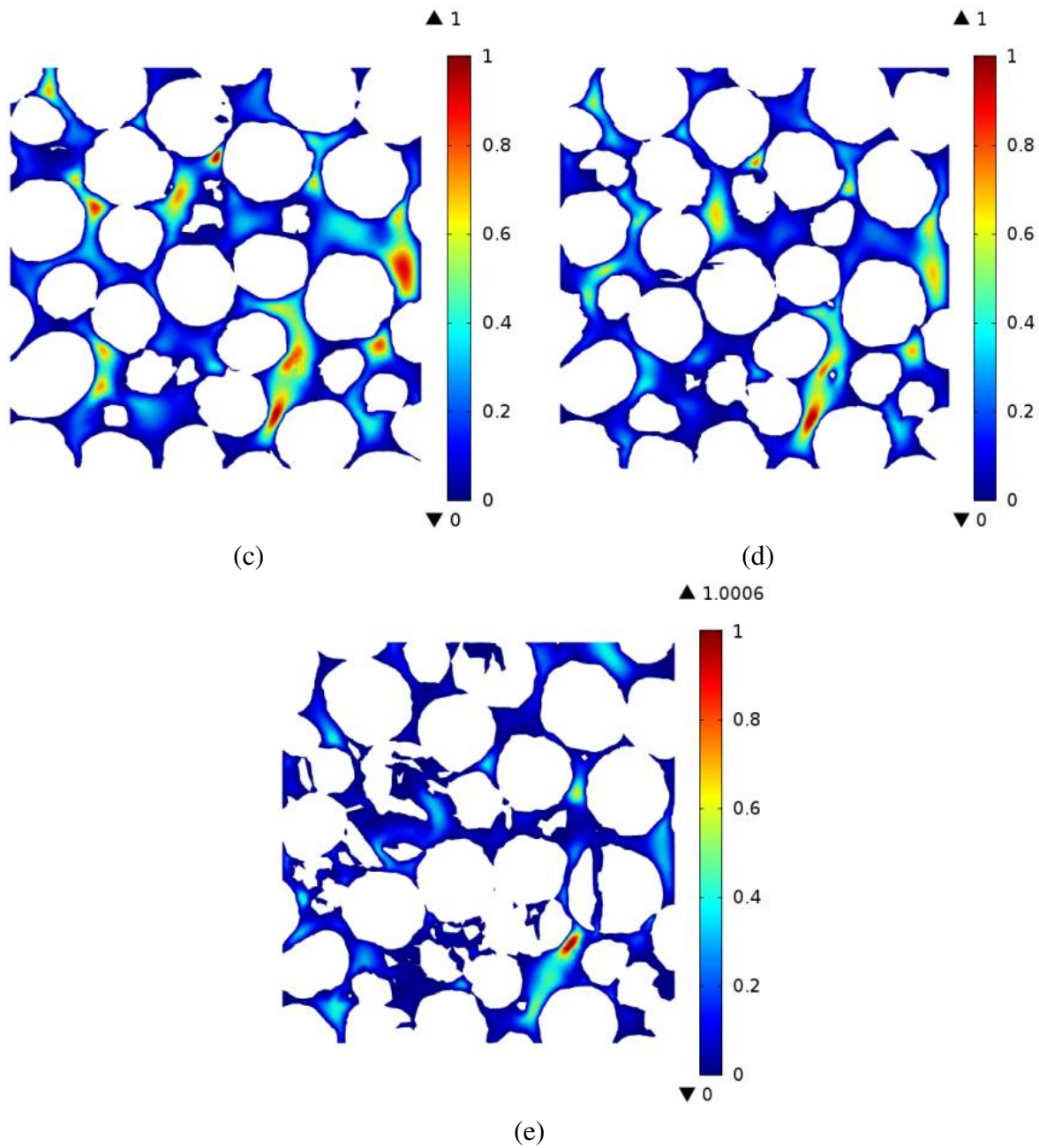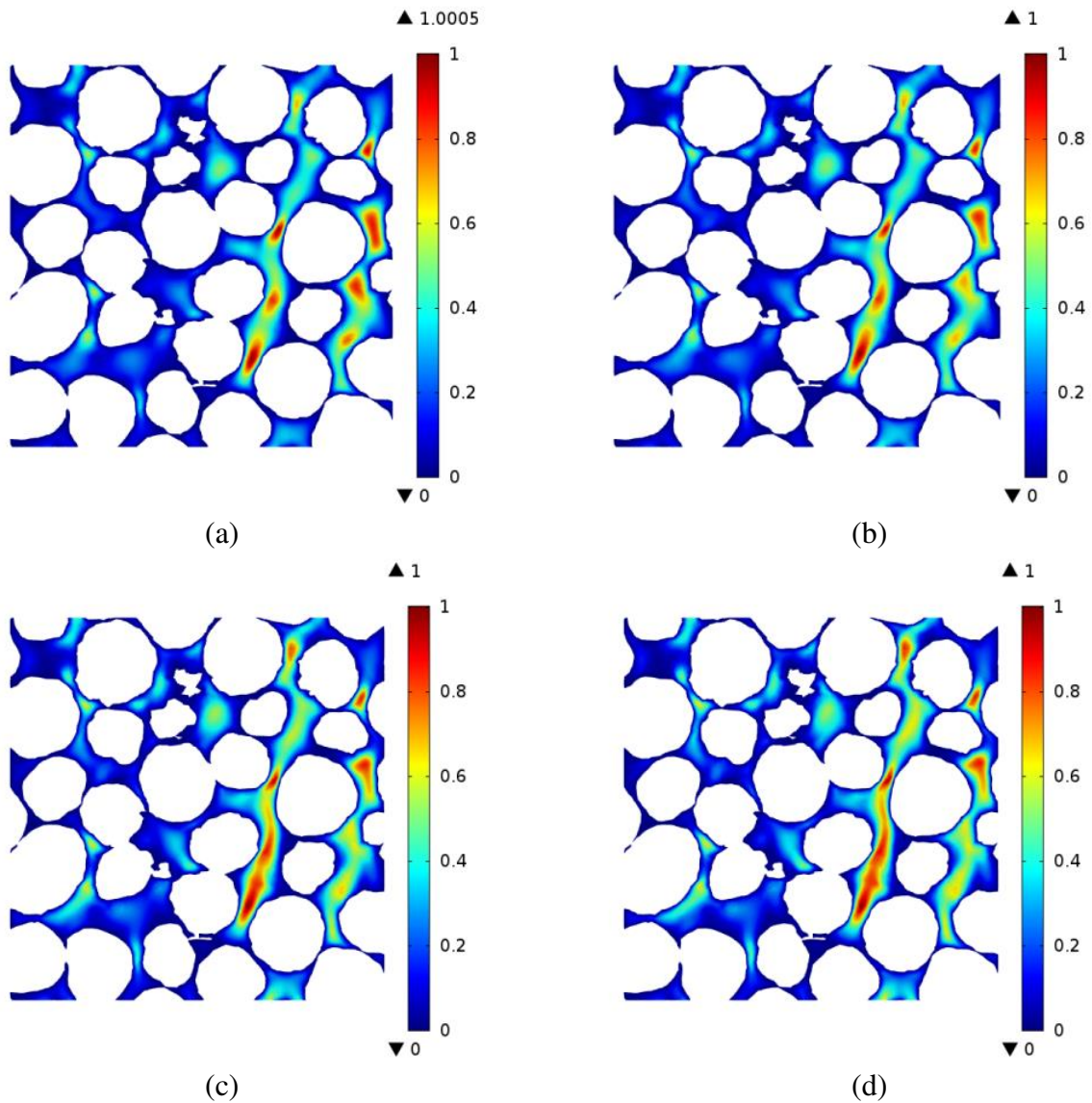

Figure 5-13: The *yz* slice of velocity field normalized by its peak value obtained from FEM P2P1 of 300^3-voxel bulk proppants at zero loading at Reynolds numbers: (a) *Re* = 0.041, (b) *Re* = 4.02, (c) *Re* = 10.76, (d) *Re* = 16.30.

5.2.4   Propped Fractures: Stress Effects

For the shale system, a 400×300-voxel rectangle inscribed by the cylinder is selected in the *xy* cross section. This cutout is 70 voxels thick in the vertical direction and includes the top and bottom shale. This cutout is represented by blue rectangles in the *yz* slice in Figure 5-4. The intrinsic permeability and conductivity are calculated and defined as the fracture permeability and conductivity, respectively. The cross sectional area of the fracture is the *xz* plane perpendicular to the flow direction (*y*). The opening width is not uniform along the cross-sectional area. Therefore it was approximated as the average opening width and was estimated by visual inspection of the segmented image at each loading stress. The width was measured 3 times at each cross section for 40 different *xz*-cross sections. The average of these 120 measurements was used as the fracture width for a given loading stress in both cross-sectional-area and conductivity calculations.

For transport in propped fractures, conductivity is often used instead of permeability so as to account for both the intrinsic permeability of the proppant as well as the fracture width, both of which contribute equally to the ability to transport fluid in a pressure or gravity driven flow. The fracture conductivity is calculated as:

$$c = kw \qquad\qquad (5\text{-}4)$$

where *k* is the fracture permeability and *w* is the opening width of the fracture.

The fracture permeability, opening width, conductivity and non-Darcy coefficient at all loading stresses are listed in Table 5-6. Permeability decreased around 25% from 4k to 8k psi and 15% from 8k to 12k psi. Similarly to bulk permeability, no significant reduction of fracture permeability occurs from 0 to 12k psi. Conductivity is reduced around 40% from 4k to 8k psi

and 25% from 8k to 12k psi. The decrease in conductivity is more pronounced than permeability because of the reduction in fracture width as the loading increases.

Table 5-6: Fracture permeability, opening length, conductivity and non-Darcy coefficient of shale fracture at different loading stresses

Loading Stress (psi)	Fracture Permeability (Darcy)	Fracture Opening Width(ft)	Fracture Conductivity (Darcy·ft)	Non-Darcy coefficient (atm·s^2·g^{-1})
0	142.31	0.0015	0.21	0.00046
4k	143.49	0.0015	0.21	0.00059
8k	107.10	0.0012	0.12	0.00077
12k	93.24	0.0010	0.09	N/A

The velocity fields at different Reynolds number (Figure 5-14) indicate that at low Reynolds number, high velocities occur only in narrow throats. As Reynolds number increases, high velocity flow also occurs in wide-open channels connected to narrow throats because flow penetrates through the pore and throat space without changing velocity.

(a)   (b)
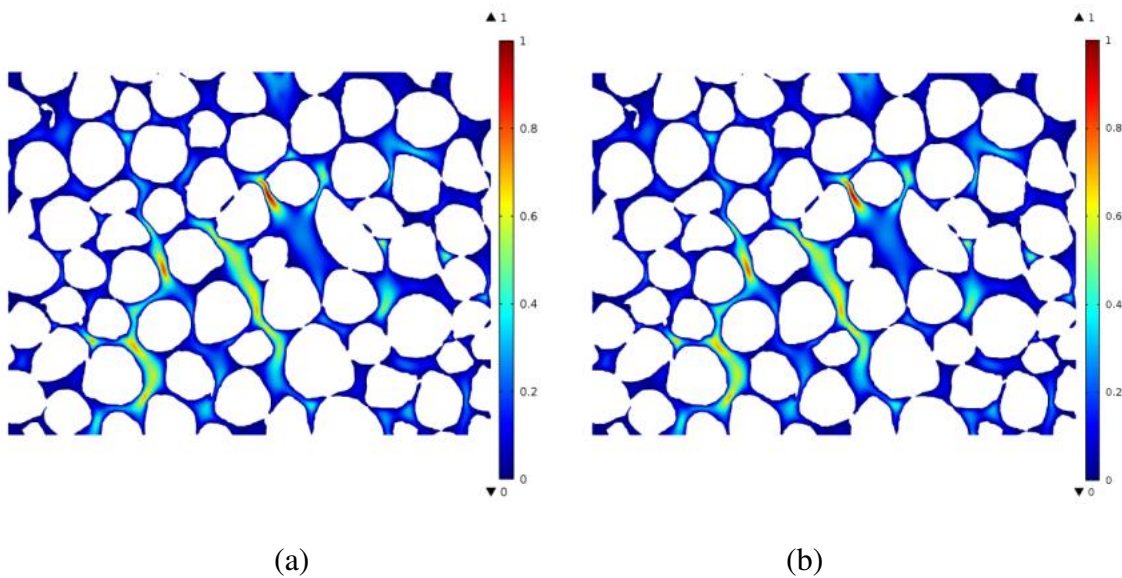
Figure 5-14: *xy* slice of velocity field normalized by its peak value obtained from FEM P2P1 of the propped fracture at 0 psi loading at Reynolds numbers: (a) *Re* = 0.016, (b) *Re* = 1.65. (continued)

79
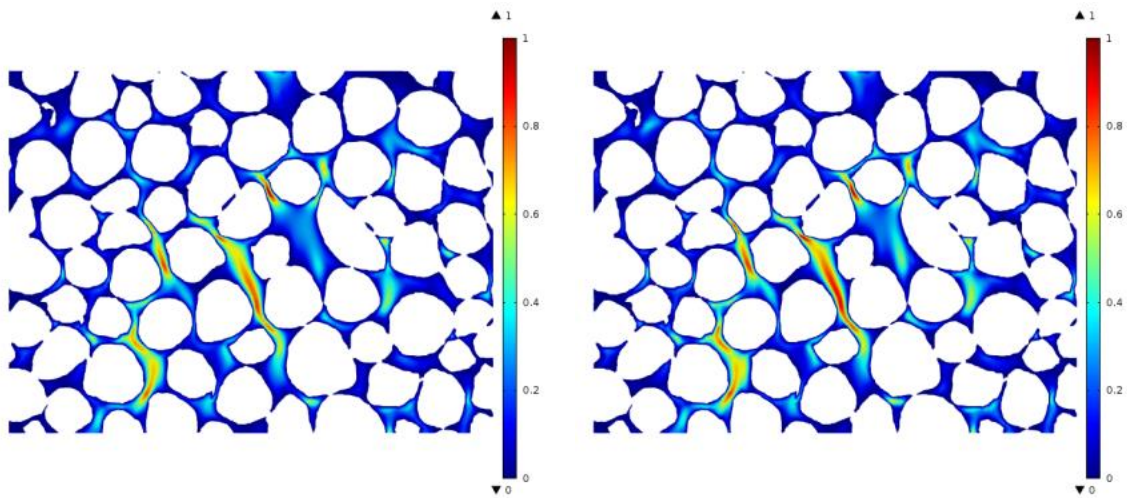
<div align="center">(c)   (d)</div>

Figure 5-14: (continued) *xy* slice of velocity field normalized by its peak value obtained from FEM P2P1 of the propped fracture at 0 psi loading at Reynolds numbers: (c) *Re* = 14.35, (d) *Re* = 25.03.

6.   Developing Network Modeling of Non-Darcy Flow

Direct simulation using methods such as the lattice Boltzmann method and finite element method are rigorous methods to predict non-Darcy flow and capture pore-scale fluid dynamics effects. However, the high computational cost limits the domain size used in these direct simulation methods. Hence, an appealing way to simulate non-Darcy flow behavior is to use network modeling. Network modeling can be used to represent the same digital image structure discussed above, but with much smaller data sets (10^3-10^5 pores), enabled through storing discrete pore and pore-throat approximations. This approximation significantly increases the computational efficiency and allows larger computational domain sizes by orders of magnitude. The hydraulic conductance in the governing equation is the key parameter to describe the flow dynamics in network models.

Significant past research has been devoted to estimating hydraulic conductance for Darcy flow. These include direct numerical simulations in realistic throat shapes and analytical solutions of the Stokes flow dynamics in idealized throat shapes, including circular, rectangular and triangular ducts. Due to the linear relationship between pressure drop and flowrate in the Darcy flow regime, the hydraulic conductance is a function of throat geometry, including factors such as throat radius, throat length, and pore radius.

To estimate the hydraulic conductance of non-Darcy flow is more challenging. The macroscopic nonlinear relationship between pressure drop and flowrate in non-Darcy flow is described by the Forchheimer equation, which uses a quadratic velocity term to represent the additional pressure drop caused by inertial effects. At the pore scale, the hydraulic conductance for non-Darcy flow must be a function of both throat geometry and fluid dynamics. Similar to earlier approaches for finding the hydraulic conductance in Darcy flow by solving the Stokes

equation, Balhoff and Wheeler (2009) solved the Naiver-Stokes equations using finite element simulations in a single duct with converging/diverging geometry. However, the nonlinear relationship between pressure drop and flow rate derived from this work does not fully represent the non-Darcy flow behavior in porous media for a couple of reasons. First, pore throat geometries are approximated as circular ducts with throat radius, throat length, aspect ratio variables that can be adjusted. Second, only effects of divergence/convergence geometry are considered for inertial flow effects; however, non-Darcy coefficient correlations with porous media properties and microscopic inertial flow behavior indicate that tortuosity of the flow paths is also a significant factor for inertial effects. It is important to consider multi-pore geometric effects when modeling inertial effects, because of the issue of tortuosity and the alignment of flow patterns. However, this has not been possible using traditional network modeling.

In this work, a new network modeling of non-Darcy flow is proposed. Rigorous results from pore-scale finite element simulation of non-Darcy flow are used to evaluate the throat flowrate distribution and pore pressure field in network models, and then hydraulic conductance is estimated from the mass conservation governing equation. The validity of hydraulic conductance values derived from FEM simulations is investigated. Throat flowrates and hydraulic conductance values in pore structures with a range of geometries are compared to assess whether network modeling can capture the shifts in flow pattern due to inertial effects.

6.1 Materials

In this work, several different types of porous media are used: 1. a standard cubic packing with eight additional spheres (60% radius of original spheres) added in the nearest origin of the domain to create heterogeneous flow path and there is no overlapping with spheres (computer generated, with the 3D pore structure image is shown in Figure 6-1); 2. a consolidated random

sphere packing (computer generated and described in more detail in section 4); 3. a proppant packing under 0 psi loading stress (described in more detail in section 5); 4. a monolalyer proppant pack with shale fractures under 0 psi loading stress (described in more detail in section 5).

Networks are generated using the voxel-based network extraction algorithm from XCT or computer generated digital images (Pradeep Bhattad et al., 2011). The image sizes and details of network structures of each porous material are listed in Table 6-1. The ball and stick schematics of network structures of each porous material are shown in the Figure 6-1, Figure 6-2 and Figure 6-3.

Unstructured meshes generated from digital images are used for finite element simulations. In the cubic packing sample, three different resolution meshes were created, the total number of elements being 1,341,274, 303,401 and 36,412 respectively. 2D slices of meshes are shown in Figure 6-4. Meshes with around 1.6 million elements, 1.4 million, and 1.2 million are used in random packing, proppant packing, and propped fractures respectively. See Sections 4 and 5 for more mesh details.

6.2 Results and Discussion

6.2.1 Throat Flowrate Calculation of Non-Darcy Flow

In network modeling, mass conservation is imposed in each pore of the network model. Hydraulic conductance of pore throats is the key parameter in the governing equation to estimate pore pressure fields, which are then used to compute throat flowrates along with pressure drop between pores. Typically, throat conductances are computed from geometric parameters. However, for this research we can also compute throat conductances from the known flowrates from FEM modeling. Details are explained in the following paragraphs.

Table 6-1: Details of images and network structures of each porous material

	Variables	Cubic Packing	Consolidated Random Packing	Proppant Packing	Propped Fracture
	Image Size (vox^3)	312^3	500^3	300^3	400×300×70
Pore	Number of Pores	141	3656	3018	842
	Porosity (%)	47.1	14.3	33.1	
	Pore Volume (vox^3) (min/ave/max)	14411.0/101355/132760	1.0/4899.9/203302.5	1/2958.5/177611.9	1.0,2429.4/96775.0
	Inscribed Radius (vox) (min/ave/max)	12.5/21.1/23.0	1/4.7/19.8	1.0/2.6/21.0	1.0/3.3/14.6
Throat	Number of Throats	988	13462	4955	3812
	Surface Area (vox^2) (min/ave/max)	41.1/3459.1/7638.9	3.9/810.5/6604.1	1.7/756.6/6748.1	2.8/345.3/3475.2
	Inscribed Radius (vox) (min/ave/max)	1.0/9.5/13.2	1.0/2.9/12.6	1.0/3.8/13.2	1.0/2.4/10.6
	Cross-Sectional Area (vox^2) (min/ave/max)	1.0/577.4/849.0	1.0/70.7/886.5	1.0/121.9/1424.6	1.0/49.0/597.6
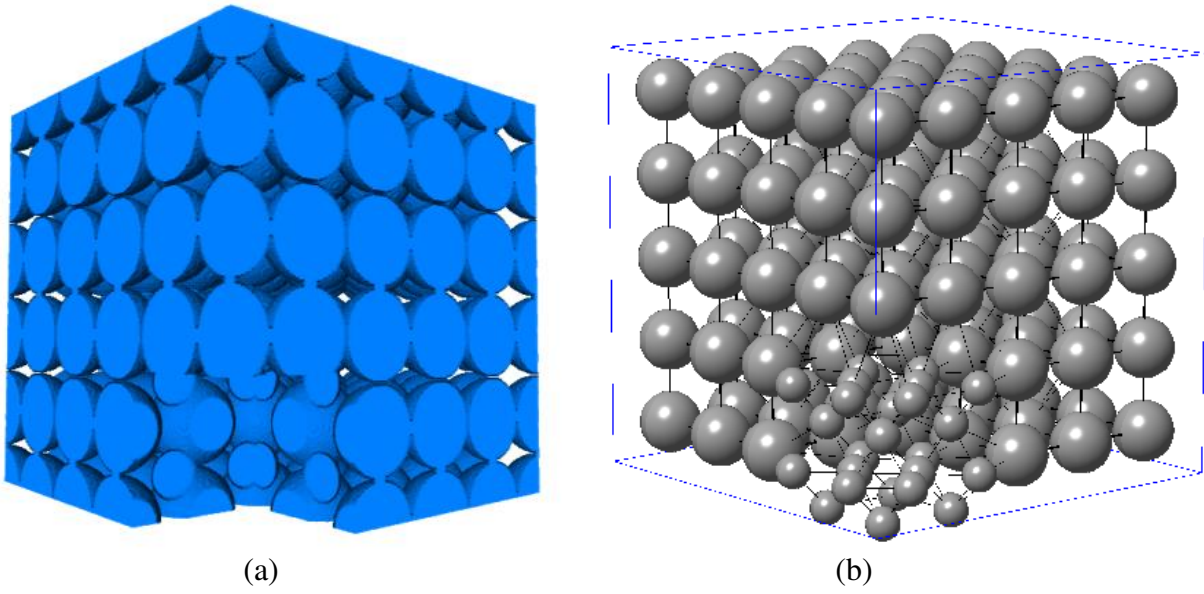
Figure 6-1: (a) 3D image of the 312^3-voxel cubic packing, and (b) the ball and stick schematic of network structure generated from (a).
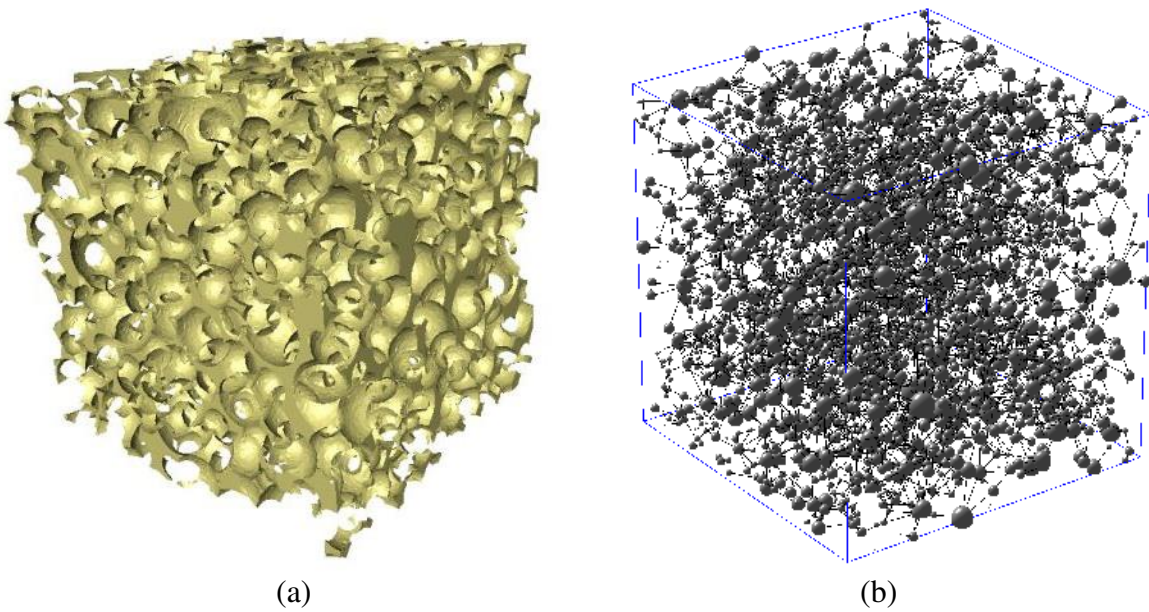
Figure 6-2: (a) 3D image of the 500^3-voxel conslidated random sphere packing, and (b) the ball and stick schematic of network structure generated from (a).

(a)   (b)
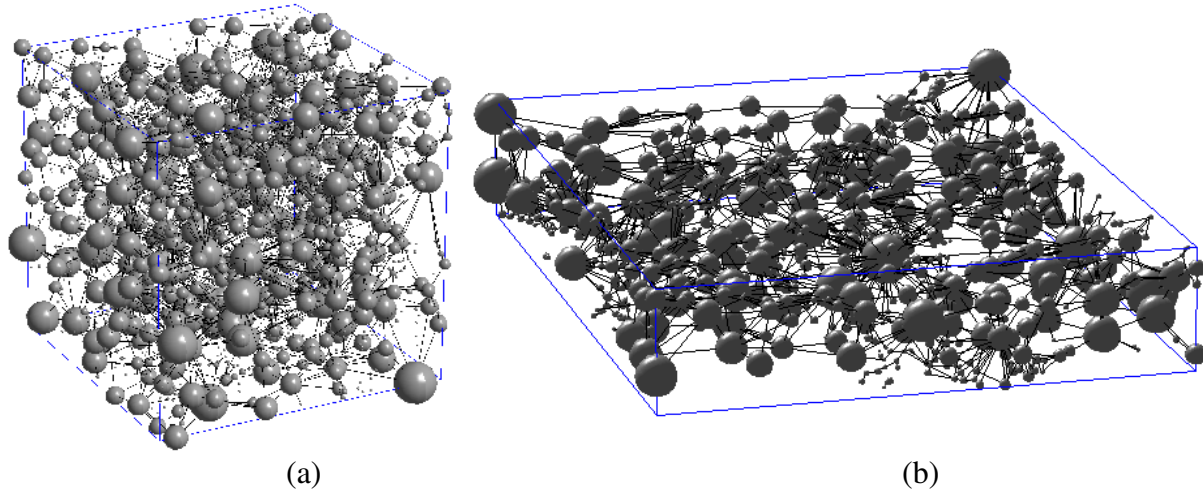
Figure 6-3: The ball and stick shematic of (a) proppant packing and (b) monolyer proppants with fractures.

(a)   (b)   (c)
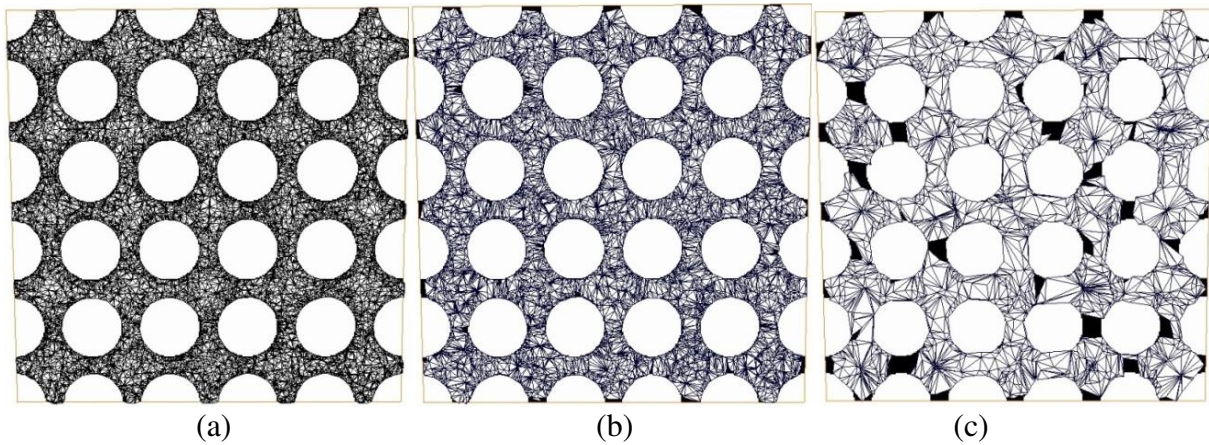
Figure 6-4: The 2D *xy* slice views of unstructured meshes of the cubic packing with different mesh refinement: (a) total elements = 1,341,274, (b) total elements = 303,401, and (c) total elements = 36,412.

The first step is to map elements and nodes to pores and pore-throats. The network generation process from voxelized digital images collects cluster of voxels for each pore. Network structures include a file which labels each voxel in the void space with a pore number. This is important information for mapping elements to pores because voxels provides a spatial link between elements and pores. There is no volume assigned to pore-throats in network

structures; pore-throats are considered as an interface surface between each pore. The integration of velocity over the interface surface area gives the pore-throat flowrate. Each element is labeled with a voxel number based on the location of the element center. Based on the elements-to-voxels and voxels-to-pores mapping information, as well as pore and pore-throat connectivity, we extract a cluster of element surfaces that comprise each throat. For any one element, this process is used to identify its pore number as well as the pore numbers of its four neighboring elements (connected with each face). If the pore number of a neighboring element is different from the element being examined, and pore numbers of these two elements are not zero, the shared face between these two elements is identified as part of the pore-throat surface between the two pores.

Secondly, after collecting surfaces of elements for each pore-throat, surface velocity, surface area and surface normal needs to be calculated. The surface velocity is calculated by interpolation of velocities from element nodes using shape functions. The flowrate through a pore-throat is calculated using:

$$q_{i,j} = \int \mathbf{v} \cdot \mathbf{n} dA \qquad (6\text{-}1)$$

It is important to point out several approximations used in mapping from elements to pores. First of all, the unstructured elements do not conform perfectly with the solid/void interface of the original image; thus, the central locations of a few elements are located in voxels assigned as the solid phase and these elements fail to map to any pores. Some adjustment is needed to correct this mapping. For an element initially tagged as the solid phase, one loop through its neighboring elements and the pore number of its neighboring elements is assigned as the pore number of the miss-assigned element. If pore numbers of neighboring elements are all zero (miss-assigned), the process is repeated several times moving outward in element layers.

Secondly, a pore and pore-throat connectivity map can be created from elements. If the pore number of one element is different than the pore number of its neighboring element, connectivity between these two pores is established (based on the element mapping). This pore and pore-throat connectivity map can be slightly different from the connectivity map defined by the network structure generated from the same digital image. Take the 500^3-voxel random packing sample used in this work as an example, along with the unstructured mesh having1.6 million elements for finite element simulations. This translates to an average of 78 voxels per element. Figure 6-5(a) is a plot of number of elements per pore versus pore volume of each pore (from network file data), which shows that there are some pores consist of no elements. Another reason for inconsistent connectivity (between network and mesh maps) is shown in Figure 6-5(b): in this void structure with a narrow throat, two pores are connected in the network model; however no elements exist in the throat area. These situations cause differences in pore-throat connectivity maps between elements and networks. Usually networks have more pore and pore-throat connection than elements.

(a)   (b)
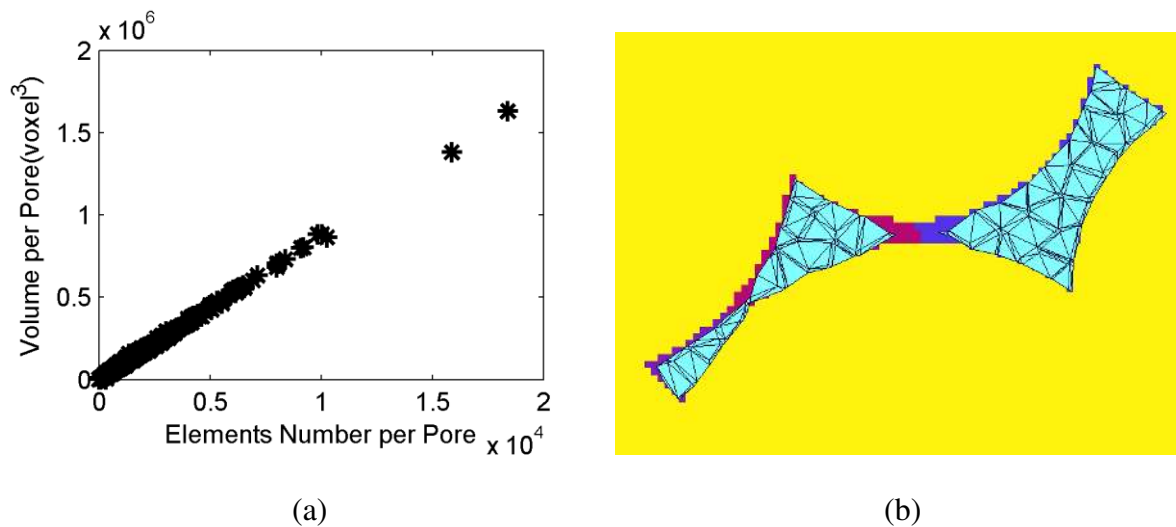
Figure 6-5: (a) Plot of volume per pore versus number of elements per pore in the consolidated random sphere packing with 1.6 million elements. (b) 2D cross-sectional pore structure image embedded with a mesh view.

6.2.2 Hydraulic Conductance Calculation

Besides throat flowrate, pore pressure also needs to be derived from finite element simulations in order to calculate the FEM-based throat hydraulic conductance using the following equation:

$$g_{i,j} = \frac{q_{i,j}\mu}{p_i - p_i} \tag{6-2}$$

The FEM-computed pressure at the network-based pore center is defined as the FEM pore pressure. The numeric value can be interpolated from nodal pressure fields from the finite element results. The first step of interpolation is to obtain the element number where the center of the pore is located. The pore pressure can then be interpolated from nodal pressure values and shape functions for this element. It is important to point out that there exist pore centers located outside of the mesh domain because the unstructured mesh does not conform to the computational domain perfectly. In this case, no pressure value can be obtained based on this interpolation. If these pores happen to be inlet/outlet pores, a constant pressure value is assigned (the same as the boundary condition in network modeling). If these pores are located in the interior, the pore pressure is calculated by averaging nodal pressure values inside this pore.

Based on finite element simulation results at different Reynolds number, throat hydraulic conductances for networking modeling can be obtained. These conductances will change as a function of Reynolds number. In the rest of the discussion, they are denoted as FEM_HCM (where HCM the array named used in network modeling for the Hydraulic Conductance Matrix).

6.2.3 Mass Conservation in Every Pore

Once the FEM-based network is created, one can verify the mass conservation in each pore based on the FEM results. In principle, this should be imposed by the continuity equation using tine FEM modeling. However, it is well known that the FEM does not ensure element-

level mass conservation. In this section, we quantify this behavior for the mesh-based networks described above.

Based on elements mapped to pores (described in the previous section), cluster of elements are collected for each pore. The inlet and outlet flowrate for each pore is calculated by integrating velocity over the element surfaces located on the pore boundaries using equation (6-1). Element surfaces on the pore boundary are identified by looping through all elements in a pore and checking whether the pore number of the element is different from the pore number of its neighboring element. If so, this element surface is identified as the pore boundary. Subsequently, the error in pore flowrate (or mass flow for a constant density fluid) is calculated as:

$$\text{Error of Pore Flowrate} = \frac{\text{Pore Inlet Flowrate} + \text{Pore Outlet Flowrate}}{\text{Pore Inlet Flowrate}} \qquad (6\text{-}3)$$

The mesh resolution impacts the error in pore flowrate, and this effect is quantified for the meshes tested. The unstructured meshes with total elements number 1,341,274, 303,401, and 36,412 are generated for the 312^3-voxel cubic packing (mesh view shown in Figure 6-4). Figure 6-6 are plots of pore flowrate error versus the inlet pore flowrate and the pore flowrate error versus number of elements per pore, calculated from FEM simulations for different mesh refinements. Most of the pores have similar numbers of elements, and as the mesh becomes coarser, the number of elements per pore is reduced accordingly. It is apparent from the comparison of Figure 6-1 (a) and (c) that the range of error increases from [-0.03, 0.03] to [-0.2, 0.15] as element numbers decrease from 1.3 million to 3.6k. As elements decrease from 1.3 million to 30.3k, the error range is relatively constant; however, the error for most pores is < 0.01 in the fine mesh, and errors become more scattered for the coarser mesh. The errors in pore flowrate versus inlet pore flowrate and number of elements calculated from the consolidated
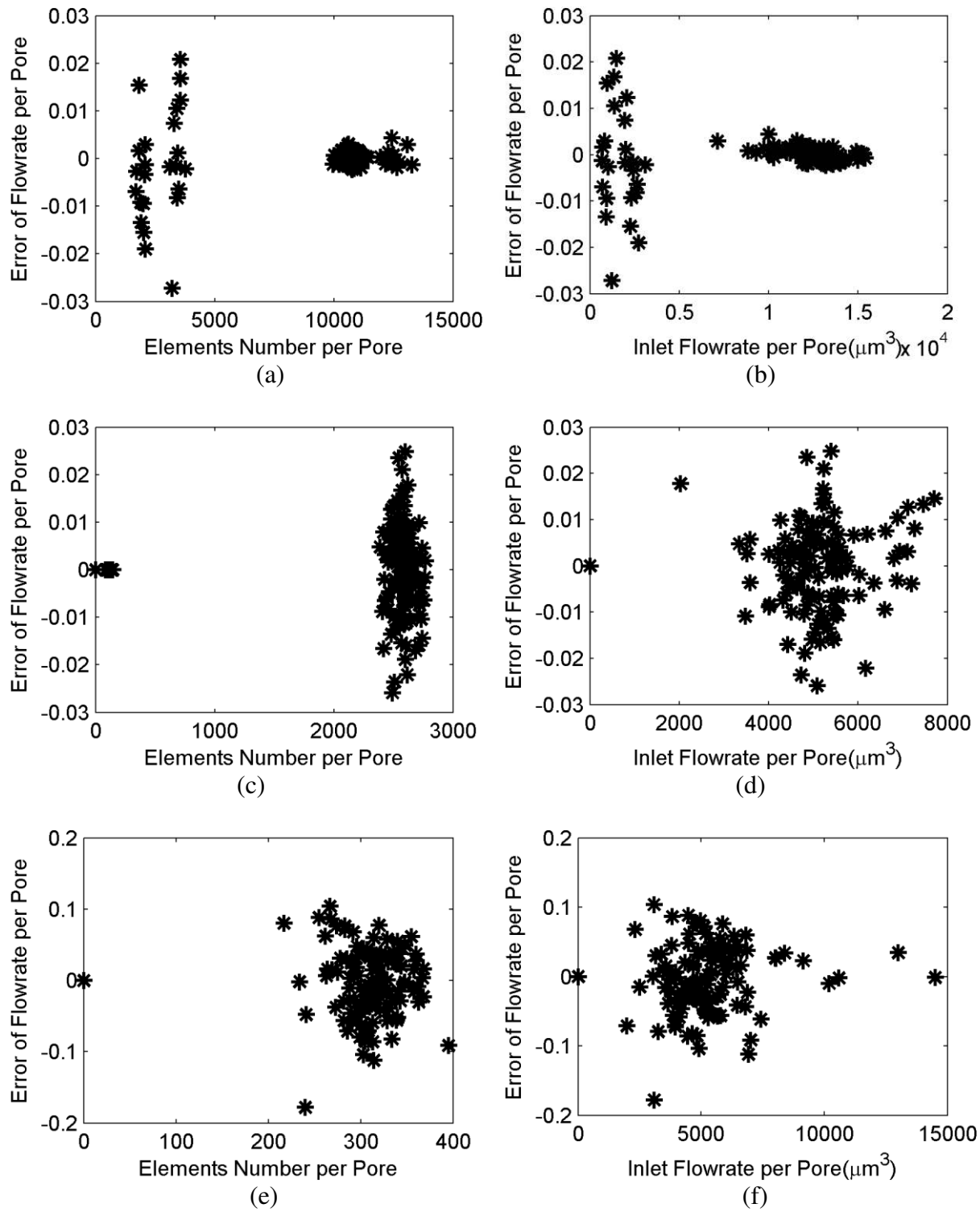
90

Figure 6-6: Plots of flowrate error per pore versus number of elements per pore and flowrate error per pore versus inlet flowrate per pore in the cubic packing with different mesh refinement: (a) (b) total elements = 1,341,274, (c) (d) total elements = 303,401, and (e) (f) total elements = 36,412.

91

random packing with 1.6 million elements number are plotted in Figure 6-7. Compared with the cubic packing, the pore-size distribution for the random packing is more spread. The plot shows that the error range reach up to [-1, 1], and large errors occur in small pores with low inlet/outlet flowrates. The error associated with pores with element numbers larger than 1×10^3 significantly reduces, to < 0.1.

6.2.4 The Validation of Network Models Using FEM_HCM

A rigorous method to validate network models is to use hydraulic conductance values calculated from finite element simulations (and/or to compare the throat flowrate distribution from network modeling versus finite element simulation). The approach used for this comparison is to obtain throat hydraulic conductances from the known FEM flow profile (i.e., the FEM_HCM values), and to update the network data accordingly and obtain a new pressure field and throat flowrate distribution. As mentioned in the previous section, the pore and pore-throat connectivity derived from the mesh is slightly different than from the original network structure. In order to eliminate mass conservation errors introduced from mismatched connectivity, a new network structure is created based on the connectivity derived from elements. In this new network model, pore number, pore location and pore volume are kept the same as in the original network structure generated from the digital image. Since the pressures of inlet/outlet pores are assigned constant values in the boundary condition for network modeling, no flowrate exists in throats connecting inlet/outlet pores. In order to be consistent with network models, nodes located on these throats surfaces are assigned as no-slip boundary condition for finite element simulations. The flowrate calculated from FEM of these throats are also zero.

A new pore pressure field is obtained by running this new network modeling with FEM_HCM values. Each throat flowrate is calculated by multiplying throat FEM_HCM values
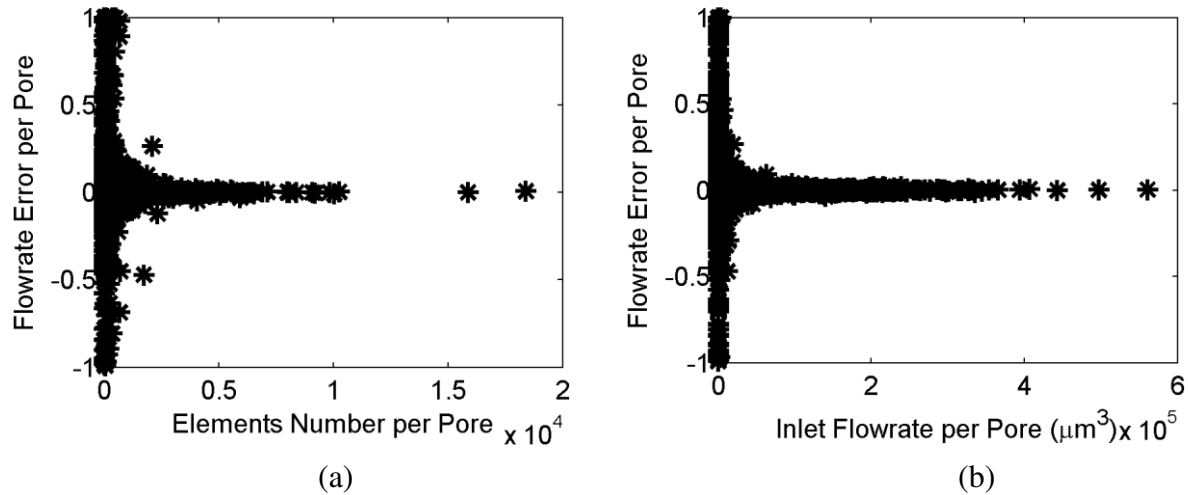
Figure 6-7: (a) Plot of error of flowrate per pore versus elements number per pore, (b) Plot of error of flowrate per pore versus inlet flowrate per pore in the consolidated random sphere packing.

with the pressure drop between the two adjoining pores obtained from the new pressure field. The throat flowrate distribution from network modeling is compared with throat flowrate distribution calculated from finite element simulations to check whether the new network model is able to predict the non-Darcy flow dynamics that are observed in the rigorous finite element simulations.

In the cubic packing sample, meshes with three different resolutions (the same meshes used in Section 6.2.2) are used to investigate mesh resolution effects on the throat flowrate prediction from network modeling. Figure 6-8 are plots of the flowrate distribution comparison between the network model (calculated with FEM_HCM conductances) and FEM model, at different mesh resolutions. A similar flowrate distribution as FEM can be predicted from network modeling for the finest mesh. As the number of elements is decreased, the deviation of flowrate data becomes more pronounced. At the coarser mesh, network using FEM_HCM predicts higher throat flowrate than FEM. The slope of trend line generated from the linear

regression of two flowrate data sets increases from 1.23 to 2.11 as the elements number reduce

from 1.3 million to 30.3k. The inability for the network and FEM results to agree, even when the

throat conductances are derived directly from FEM, is unfortunate, and can be traced back to the

errors in pore-scale mass balances (for the FEM results) that were shown in the previous section.

(a)

(b)

(c)

Figure 6-8: Plots of throat flowrate distribution calculated from network models using FEM_HCM versus throat flowrate distribution calculated from finite element simulation in the cubic packing with different mesh refinements: (a) total elements = 1,341,274, (b) total elements = 303,401, and (c) total elements = 36,412.

The mass conservation of each pore is an essential prerequisite to obtain a FEM_HCM value that can predict the same flowrate as from finite element simulations. As meshes become coarse, larger errors exist in the mass balance for each pore (shown in Figure 6-6). Therefore, network flowrates predicted using FEM_HCM values showed significant error relative to the flowrates from FEM.

The flowrates from network and FEM of the random sphere pack and proppant pack are compared at different Reynolds numbers in Figure 6-9 and Figure 6-10. Four Reynolds numbers (4×10^{-5}, 4×10^{-3}, 7.0 and 11.3) are chosen and from the permeability versus Reynolds number plot (Figure 6-11), one can determine that flow is in the Darcy flow regime when $Re = 4\times10^{-5}$ and 4×10^{-3} and non-Darcy flow regime when $Re = 7.0$ and 11.3. The flowrate distribution calculated from network modeling is compared to the FEM calculation. This is done using both FEM_HCM and the original HCM conductances, at each Reynolds number. Flowrates from FEM_HCM network computations fail to agree well with the same FEM flowrates due to the large mass balance error in the meshed pores (Figure 6-7). The original HCM values remain constant for different Reynolds numbers; therefore, throat flowrate increase linearly with pressure drop. Whereas, due to inertial effects, throat flowrates in the FEM simulations do not linearly increase with pressure drops. Therefore as the Reynolds number increases, the deviation of flowrate data becomes more pronounced. This shows that (as expected) flowrates predicted from original HCM values fails to predict the non-Darcy flow behavior. Although network models using FEM_HCM in this random packing do not predict the same flowrate as the FEM simulations, the flowrate differences between the network and FEM results do not have a significant change as the Reynolds number increases. This indicates that non-Darcy flow behavior is incorporated, at least to some extent, into the network flowrates predicted from FEM_HCM.
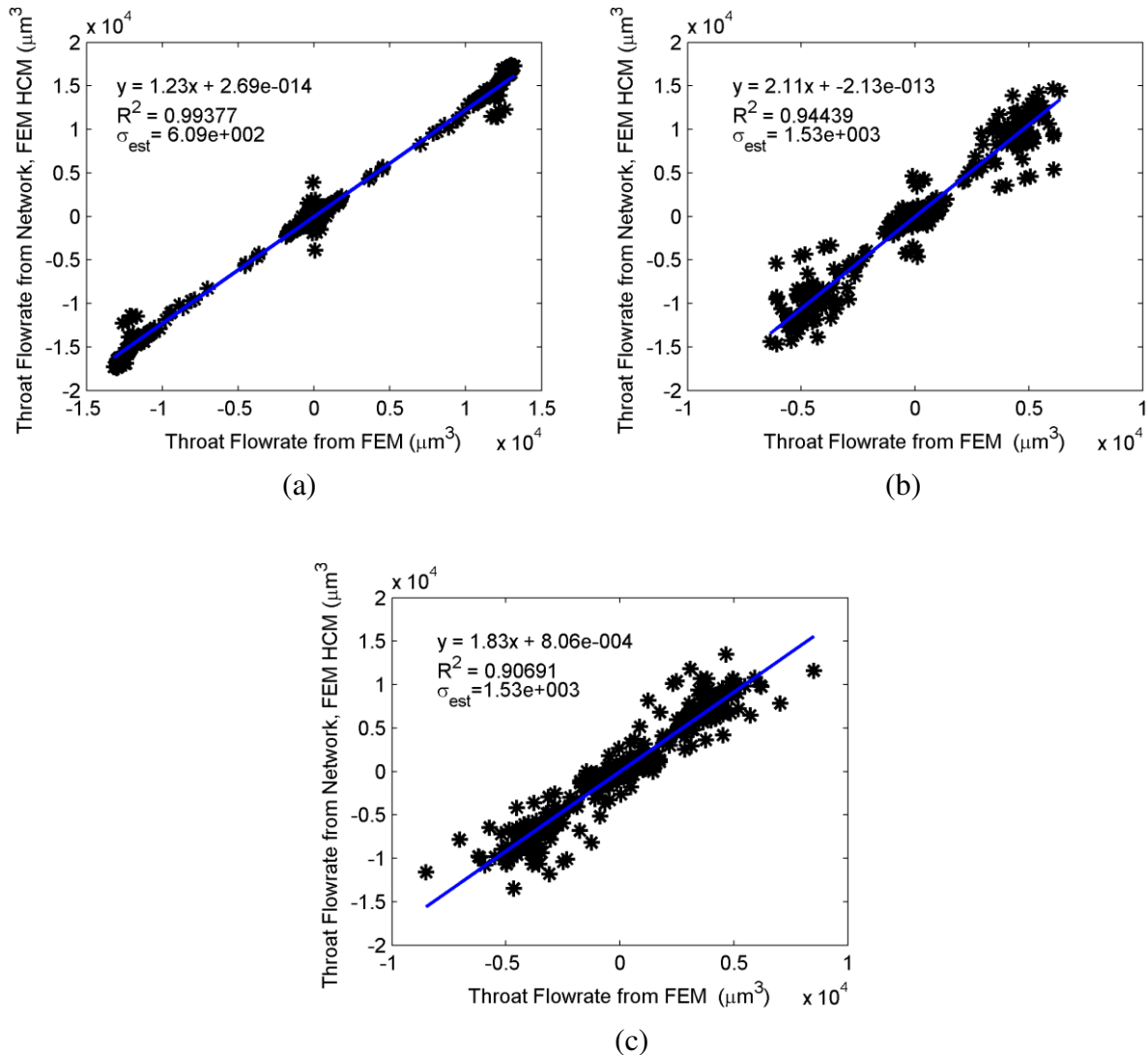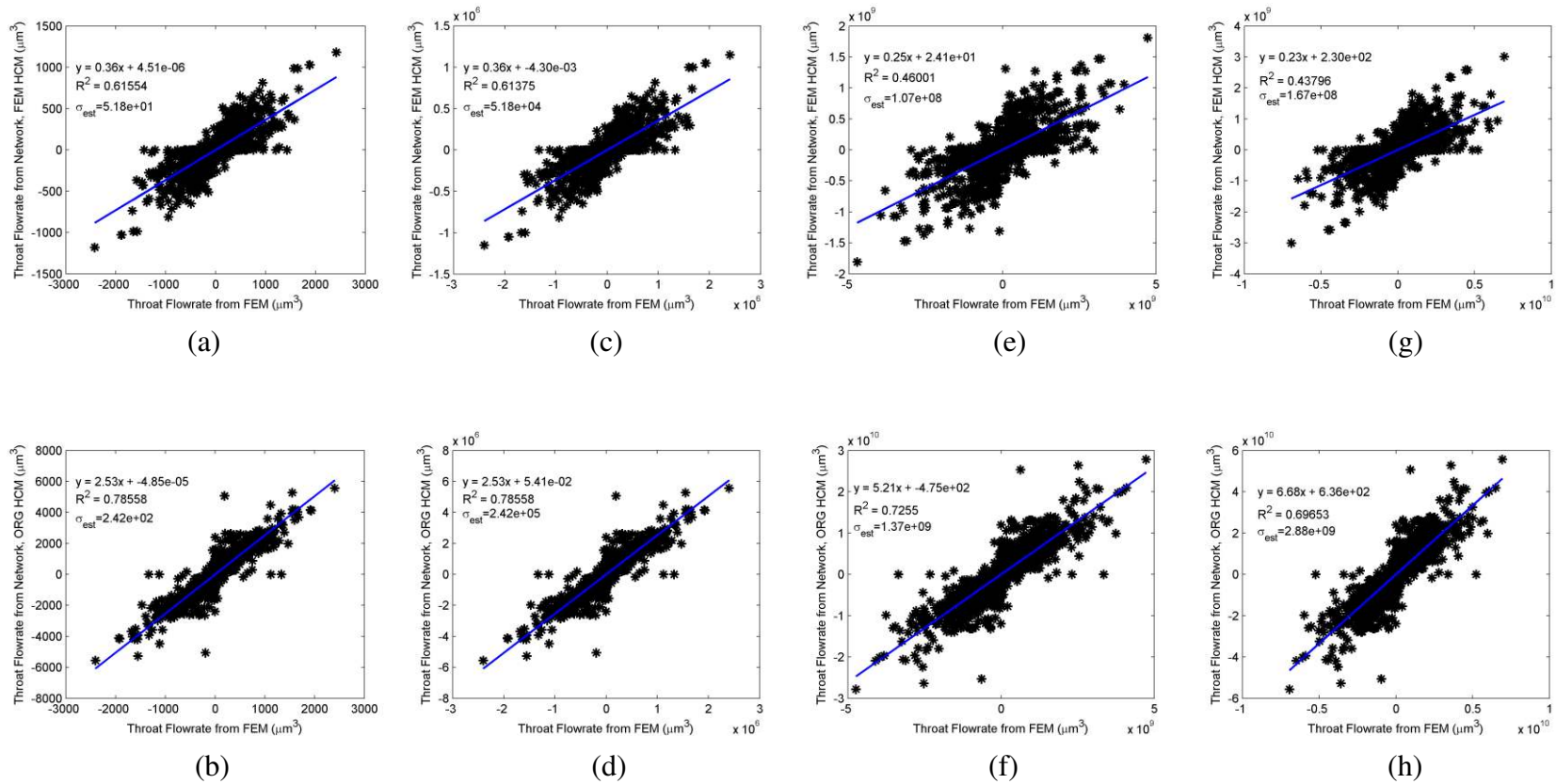
Figure 6-9: Plots of throat flowrate distribution calculated from network models using FEM_HCM versus throat flowrate distribution calculated from FEM (left column) and throat flowrate distribution calculated from network models using original HCM versus throat flowrate distribution calculated from FEM (right column): (a)(b) $Re = 4 \times 10^{-5}$, (c)(d) $Re = 4 \times 10^{-3}$, (e)(f) $Re = 7.0$, (g)(h) $Re = 11.3$.
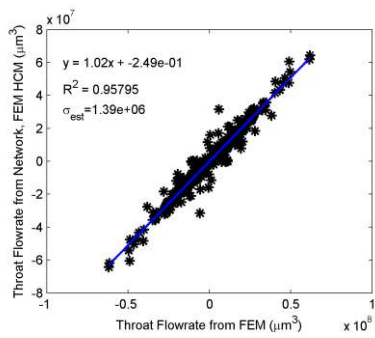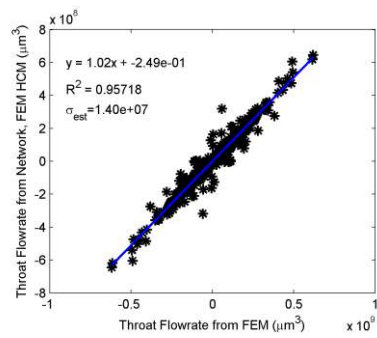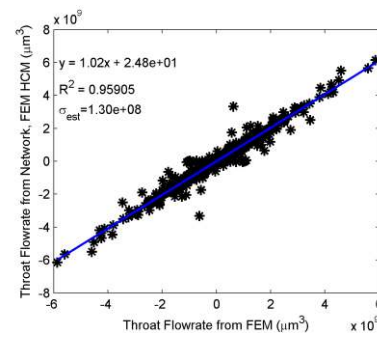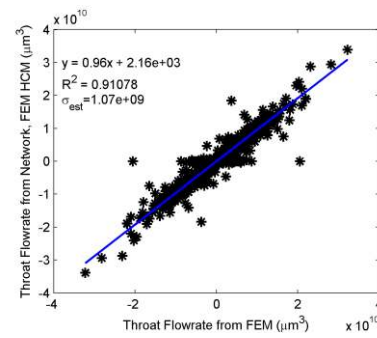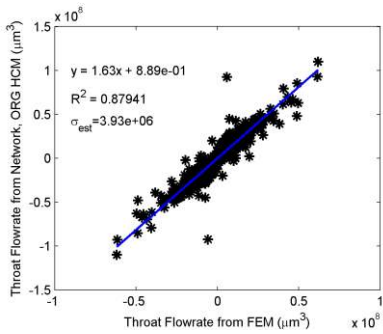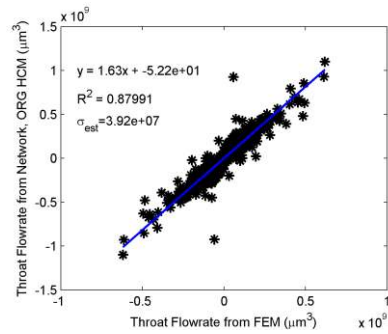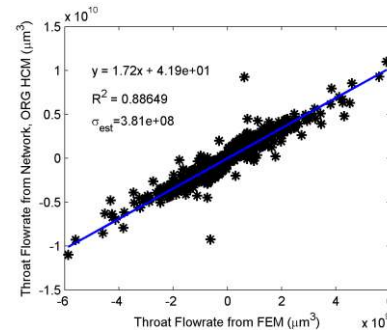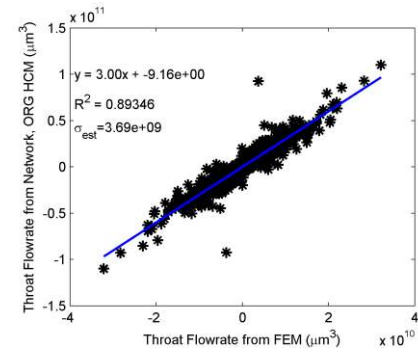
Figure 6-10: Plots of throat flowrate distribution calculated from network models using FEM_HCM versus throat flowrate distribution calculated from FEM (left column) and throat flowrate distribution calculated from network models using original HCM versus throat flowrate distribution calculated from FEM (right column): (a)(b) $Re = 5\times10^{-3}$, (c)(d) $Re = 5\times10^{-1}$, (e)(f) $Re = 18.1$, (g)(h) $Re = 28.6$.

97

The flowrate distribution calculated from the FEM_HCM values versus original HCM values are also compared to the FEM results for the proppant packing sample. Four Reynolds numbers (5×10^{-3}, 5×10^{-1}, 18.1 and 28.6) are simulated. As Figure 6-9 shows, compared to the random packing, the network that uses FEM_HCM provides a good prediction of flowrate. As Reynolds number is increased, the distribution becomes slightly more scattered, while the slope of the trend line derived from linear regression does not change significantly.

<div align="center">(a)   (b)</div>
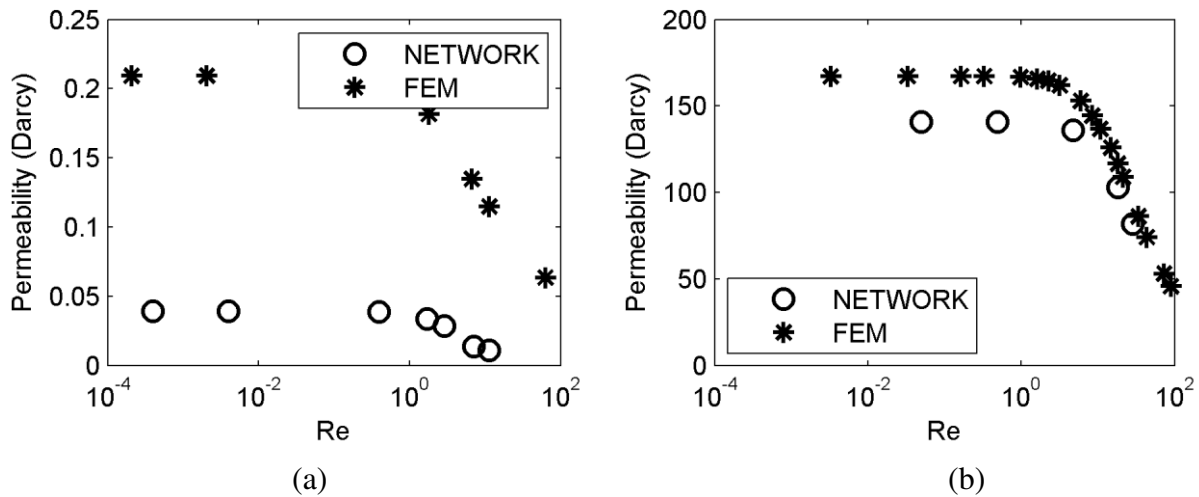
Figure 6-11: Apparent permeability obtained from network modeling using FEM_HCM and FEM at different Reynolds number in the (a) random packing and (b) proppant packing.

6.2.5 Pore-scale Investigation of Flowrate and Hydraulic Conductance

The original goal of this work was to model a priori non-Darcy flow using a network approach. A factor that has not been taken into account well is tortuosity of the flow paths, which is considered a significant factor in inertial effects. Hence, it is important to understand how the fluid dynamics changes in different flow path geometries in the non-Darcy flow regime. Two geometries are used to show this effect, as described below.

An artificial channel (10×10×300-voxel) is created in the random sphere packing. This straight channel is an idealized structure meant to mimic the geometry that occurs when a series of pores are aligned. Two different flow paths, one in the straight channel and another in a tortuous channel, are investigated to compare inertial effects on pore-scale flow fields (Figure 6-12).
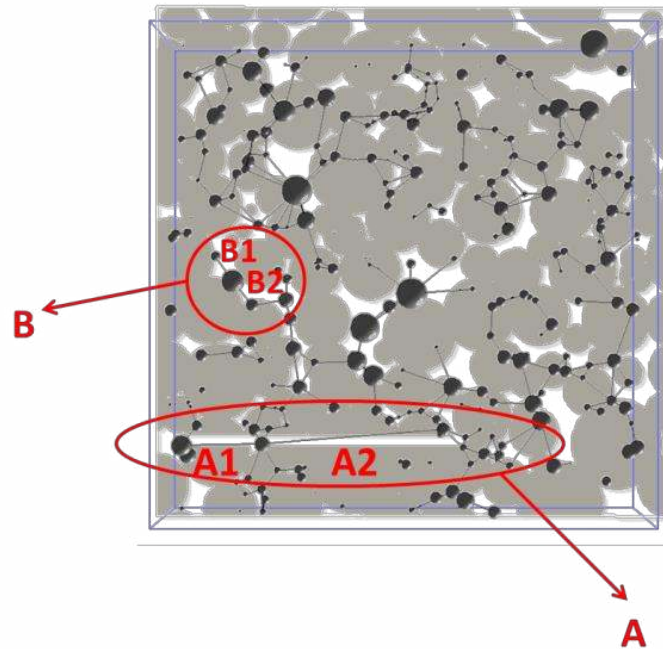
Figure 6-12: Illustration of location of throats A1, A2, B1, and B2 locations in 2D *zx* slice image embedded with network structures.

A set of 2D *zx* slices of the velocity fields normalized by peak value are shown in Figure 6-13 for pressure drops equal to 1, 1×10^2, 5×10^5 and 1×10^6, with *Re* equals to 4×10^{-6}, 4×10^{-4}, 1.7 and 3.0 accordingly. At the low Reynolds number (pressure drop), the highest velocity appears in a small throat area which is connected with a large pore. This throat area is defined as region B in the schematic of the network structure. It shows that there are three pores with throats B1 and B2 connecting these pores. However, as the Reynolds number increases, the high velocity also starts to appear in the straight channel, shown as region A in Figure 6-12. Region A also has

three pores with throats connecting them labeled A1 and A2. At the small Reynolds number, viscous forces dominates the momentum transport, and highest flow velocities occur where there is a large reduction of flow area connection fairly large pores. As the inertial forces become significant, the fluid flow starts to exhibit slightly more jet-like behavior.
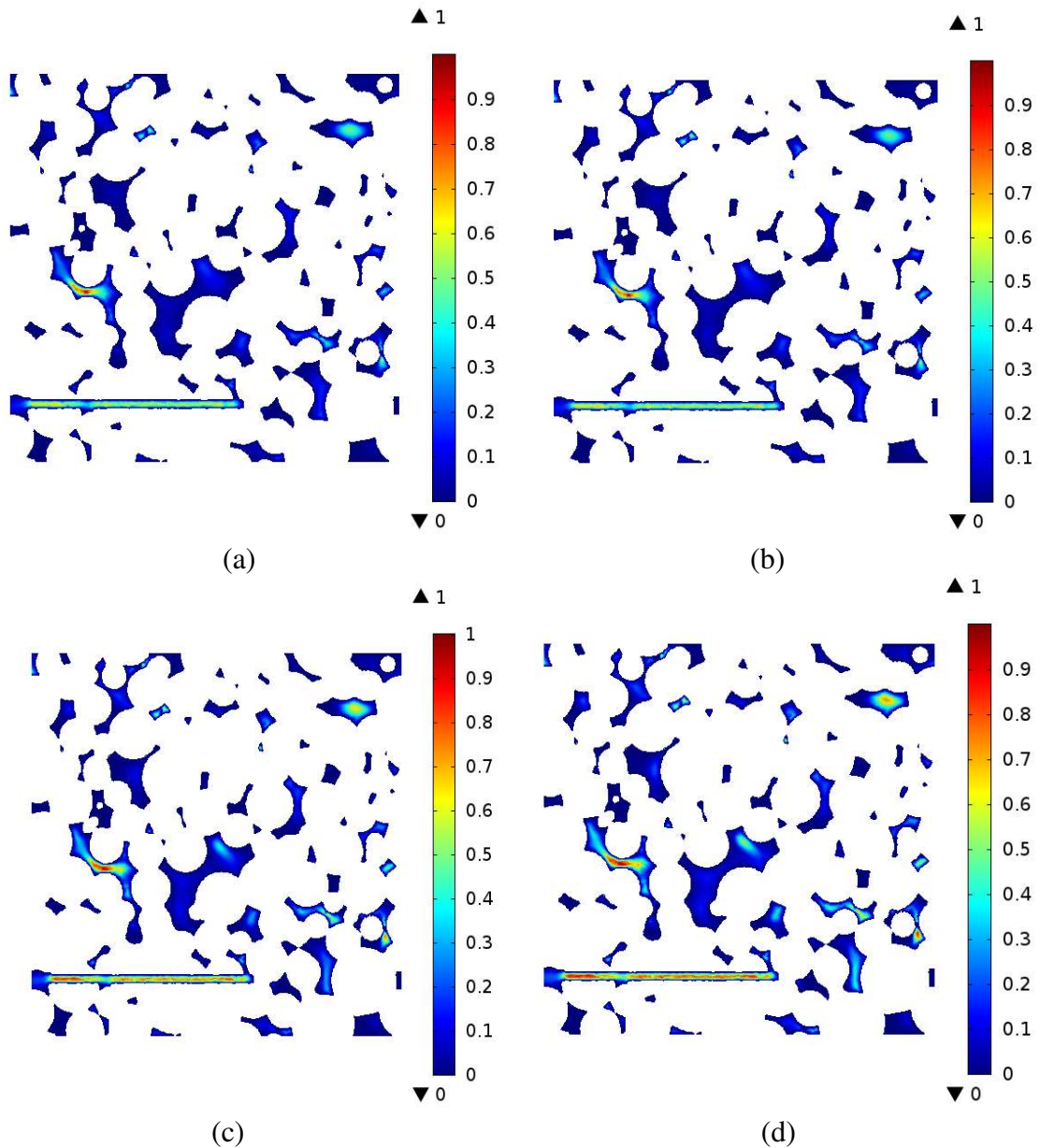
Figure 6-13: 2D zx slices of velocity field normalized by peak value of random sphere packing at different pressure drops: (a) $\Delta p = 1$ ($Re = 4 \times 10^{-6}$), (b) $\Delta p = 1 \times 10^4$ ($Re = 4 \times 10^{-4}$), (c) $\Delta p = 5 \times 10^5$ ($Re = 1.7$), (d) $\Delta p = 1 \times 10^6$ ($Re = 3.0$).

100

In order to quantify the inertial effects in a way that can be used in network modeling, FEM_HCM values and flowrates calculated from the network model (using FEM_HCM conductances) are listed in Table 6-2 and Table 6-3. We define a flowrate ratio variable FR, which quantifies the flowrate change scaled by the inverse of the pressure drop change, defined as:

$$FR = \frac{Flowrate(\Delta p_1)}{Flowrate(\Delta p_0)} \frac{\Delta p_0}{\Delta p_1} \tag{6-4}$$

For low-Reynolds number flows, FR should always equal one since flowrate scales linearly with pressure gradient. For inertial flows, this parameter can help define how the inertial effects shift the flow distribution. For the throats discussed above, FR_1, FR_2, and FR_3 are defined as follows:

$$FR_1 = \frac{Flowrate(\Delta p = 1 \times 10^2)}{Flowrate(\Delta p = 1)} \frac{\Delta p(1)}{\Delta p(1 \times 10^2)} \quad , \quad FR_2 = \frac{Flowrate(\Delta p = 5 \times 10^5)}{Flowrate(\Delta p = 1)} \frac{\Delta p(1)}{\Delta p(5 \times 10^5)} \quad ,$$

$$FR_3 = \frac{Flowrate(\Delta p = 1 \times 10^6)}{Flowrate(\Delta p = 1)} \frac{\Delta p(1)}{\Delta p(1 \times 10^6)}$$

FR_1, FR_2 and FR_3 values for throats A1, A2, B1, and B2 are listed in Table 6-4. When pressure drop increases from 1 ($Re = 4 \times 10^{-6}$) to 1×10^2 ($Re = 4 \times 10^{-4}$) the flowrate ratio remains unity in all throats, as suggested above. When pressure drop increases to 5×10^5 ($Re = 1.7$) and 1×10^6 ($Re = 3.0$), the flowrate ratio in all throats are less than one. Inertial effects in the non-Darcy flow cause a reduction of flowrate. The higher FR_2 and FR_3 values in throats A1 and A2 indicate that inertial effects lead to lower flowrate reduction in these highly aligned pores. In contrast, the more tortuous flow path in throats B1 and B2, correspond to inertial effects requiring more of the pressure drop to overcome the tortuous flow path, and thus a larger reduction of flowrate along the more tortuous flow path.

Table 6-2: Flowrate of throats A1, A2, B1 and B2 at different pressure drops

Throat	Flowrate ($\Delta p = 1$)	Flowrate ($\Delta p = 1\times10^2$)	Flowrate ($\Delta p = 5\times10^5$)	Flowrate ($\Delta p = 1\times10^6$)
A1	1.44×10^2	1.44×10^4	6.70×10^7	1.06×10^8
A2	0.27×10^2	2.75×10^3	1.25×10^7	2.28×10^7
B1	4.87×10^2	4.87×10^4	1.36×10^8	2.51×10^8
B2	4.87×10^2	4.87×10^4	1.36×10^8	2.51×10^8

Table 6-3: FEM_HCM of throats A1, A2, B1, and B2 at different pressure drops

Throat	FEM_HCM ($\Delta p = 1$)	FEM_HCM ($\Delta p = 1\times10^2$)	FEM_HCM ($\Delta p = 5\times10^5$)	FEM_HCM ($\Delta p = 1\times10^6$)
A1	4.288	4.288	3.179	2.413
A2	1.449	1.449	1.113	0.854
B1	62.25	62.24	34.04	25.47
B2	33.10	33.10	26.16	18.99

Table 6-4: Flowrate ratio FR and angle of throats A1, A2, B1 and B2

Throat	FR_1	FR_2	FR_3	Angle(degree)
A1	1.00	0.93	0.73	134
A2	1.00	0.91	0.83	112
B1	1.00	0.56	0.51	142
B2	1.00	0.56	0.51	112

The inertial effects on the pore-scale velocity field in propped fractures are also studied. From 2D xy slices of velocity fields shown in Figure 6-14, the highest velocity in the low-Re regime occurs at a narrow throat connected with a large pore, defined as region B. At higher Reynolds number, high velocities are observed in a straight and narrow channel created from several pores aligned together, defined as region A. Pores in the network structure are illustrated in Figure 6-15, as well as throats A1, A2, A3 and B1. The flowrate in four throats at four different pressure drops (1, 1×10^4, 2×10^5, and 5×10^5) with Re (5×10^{-5}, 5×10^{-1}, 8.3 and 16) accordingly are listed in Table 6-5. The flowrate ratio FR is also calculated. When pressure drop increases from 1 ($Re = 5\times10^{-5}$) to 2×10^5 ($Re = 8.3$) and then 5×10^5 ($Re = 16$), the FR value of throat A1 is smallest and this indicates that inertial effects cause a large reduction of flowrate. A closer look at the throat A1 location shows that it connects pores via a more tortuous flow path.

Flowrate has less reduction in A3 and even exceeds unity in A2 because throat A2, A3 are in a straight flow path. As discussed earlier with the random packing, the jet-like flow behavior in the straight flow channel carries more fluid in the non-Darcy flow regime.


(a)

(b)

(c)

(d)
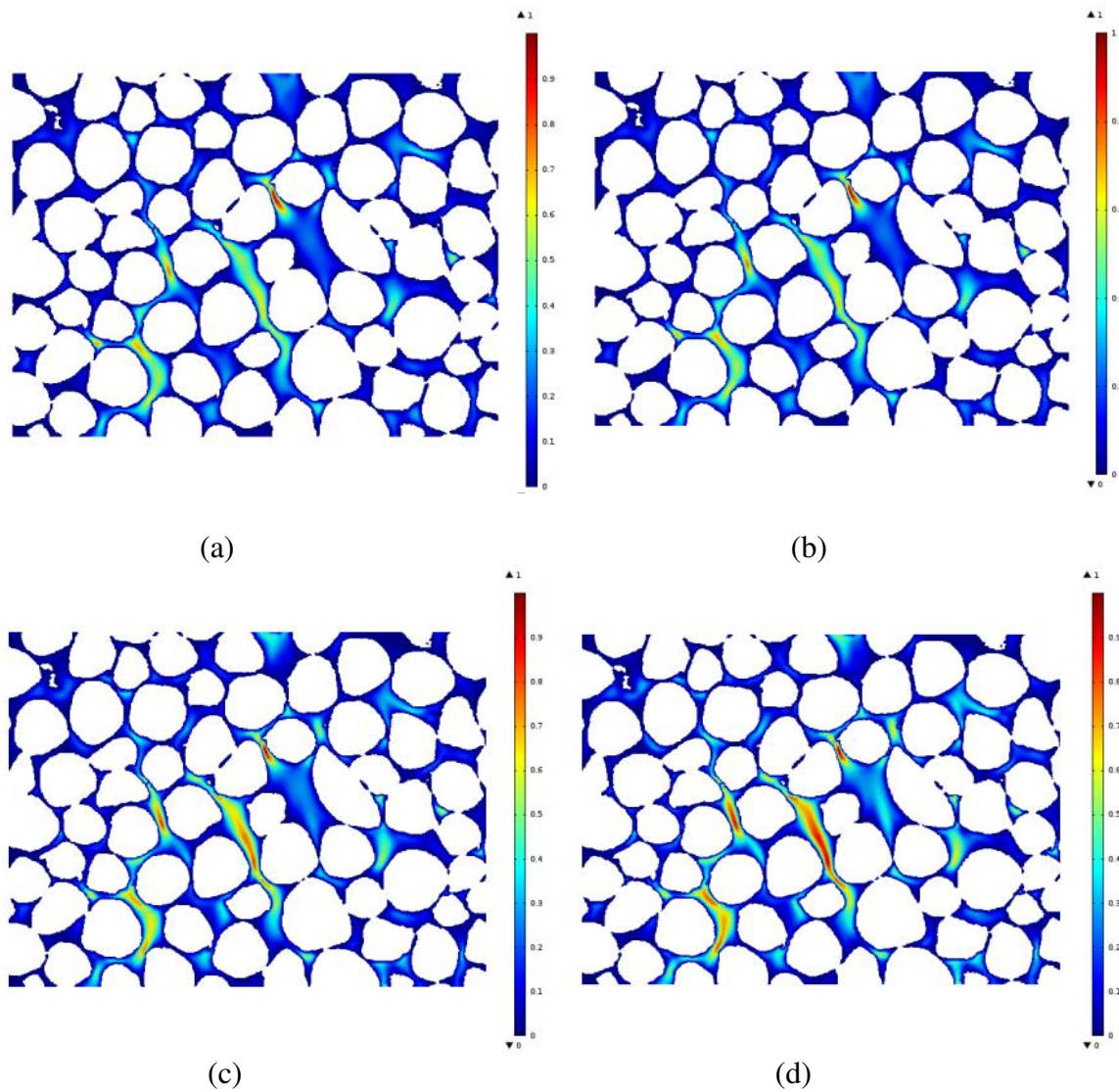
Figure 6-14: 2D *xy* slice of velocity field normalized by its peak value in propped fractures at different pressure drops: (a) $\Delta p = 1$ ($Re = 5\times10^{-5}$) (b) $\Delta p = 1\times10^{4}$ ($Re = 5\times10^{-1}$), (c) $\Delta p = 2\times10^{5}$ ($Re = 8.3$), (d) $\Delta p = 5\times10^{5}$ ($Re = 16$).
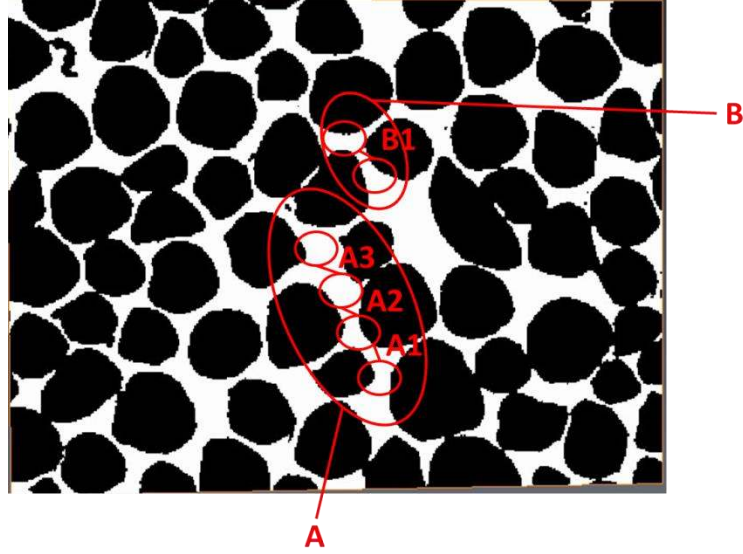
Figure 6-15: Illustration of location of throats A1, A2, A3 and B1 locations in 2D *xy* slice image

Table 6-5: Flowrate of throats A1, A2, A3 and B1 at different pressure drops

Throat	Flowrate ($\Delta p = 1$)	Flowrate ($\Delta p = 1\times10^4$)	Flowrate ($\Delta p = 2\times10^5$)	Flowrate ($\Delta p = 5\times10^5$)
A1	4.58×10^2	4.58×10^6	3.25×10^7	7.80×10^7
A2	0.78×10^2	8.34×10^5	1.97×10^7	3.67×10^7
A3	2.07×10^3	2.11×10^7	3.12×10^8	6.97×10^8
B1	0.34×10^2	3.57×10^5	5.87×10^6	1.16×10^7

Table 6-6: Flowrate ratio FR and angle of throats A1, A2, B1 and B2

Throat	FR1	FR2	FR3	Angle (degree)
A1	0.99	0.36	0.03	101
A2	1.06	1.25	0.94	108
A3	1.00	0.75	0.67	116
B1	1.00	0.84	0.67	96

The quantitative analysis of inertial effects on pore-scale flowrate shows that tortuosity of flow path has a significant effect on hydraulic conductance for non-Darcy flow. In order to quantify the tortuosity of flow in a network modeling framework, we have proposed a new variable throat angle α. The angle α of one throat connected by two pores is calculated based on the pore location, pore connectivity, and throat flowrate. Consider a throat with single

104

connectivity shown as Figure 6-16 as an example, the angle of throat connecting *ipore* and *jpore* is defined as:

$$\alpha = \frac{(\alpha_1 + \alpha_2)}{2} f_1 f_2 \qquad (6\text{-}5)$$

where α_1 is the angle between *npore* and *jpore*, α_2 is the angle between *ipore* and *mpore*, f_1 is the ratio of flowrate of the throat connecting *npore* and *ipore* to total flowrate entering *ipore*, f_2 is the ratio of flowrate of the throat connecting *jpore* and *mpore* to total flowrate leaving *jpore*. If there are multiple throats connecting with *ipore* and *jpore* respectively, the throat angle α equals to the weighted average of the angle from all connectivity.
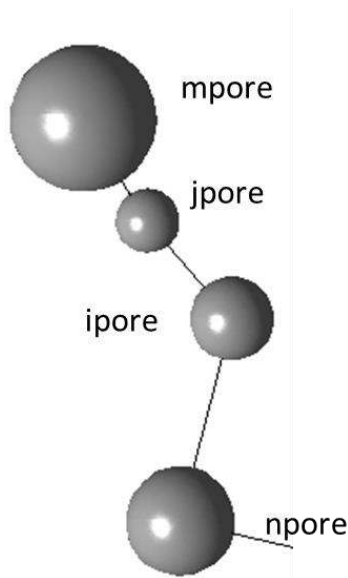
Figure 6-16: Schematic drawing of pore and pore-throat for the angle calculation

The angle of throats in random packing and propped fracture discussed in the above are reported in Table 6-4 and Table 6-6. The relationship between FEM_HCM at different Reynolds numbers and network parameters including throat radius to the fourth power, inverse of throat length, aspect ratio and angle are showing in the scatter plot of Figure 6-17. FEM_HCM from
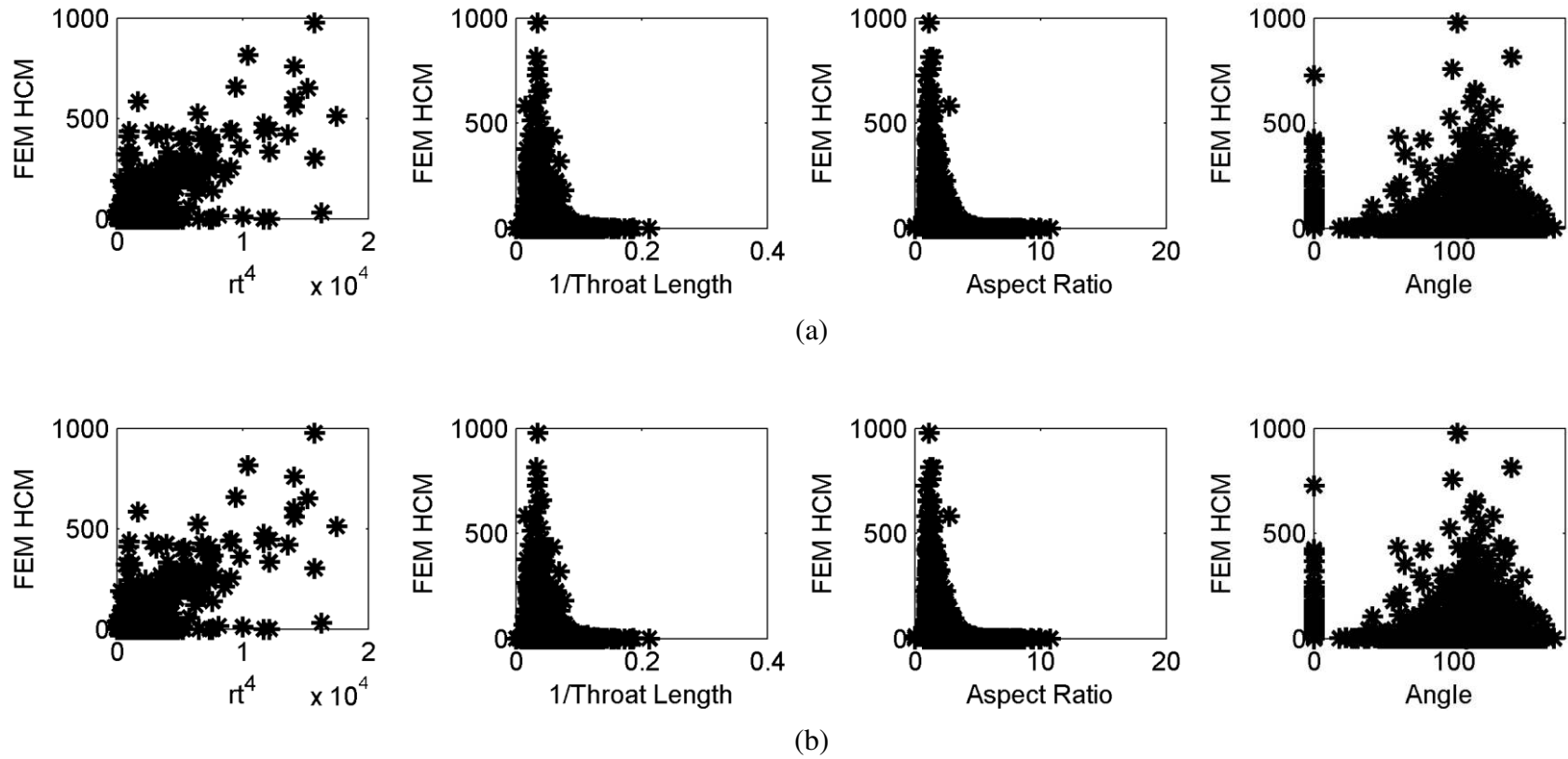
Figure 6-17: The scatter plot of throat radius to the fourth power, inverse of throat length, aspect ratio, and angle with FEM_HCM (from left to right) in the random sphere packing at: (a) $Re = 4\times10^{-5}$, (b) $Re = 4\times10^{-3}$. (continued)
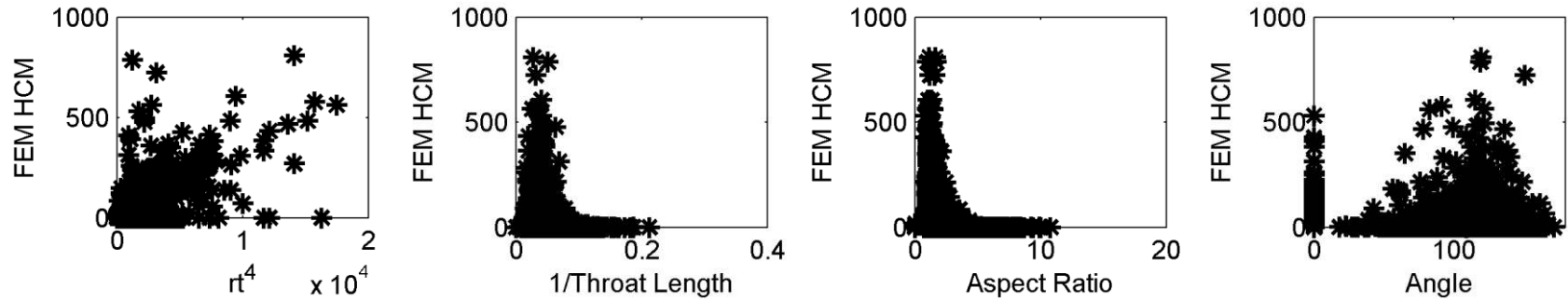
(c)
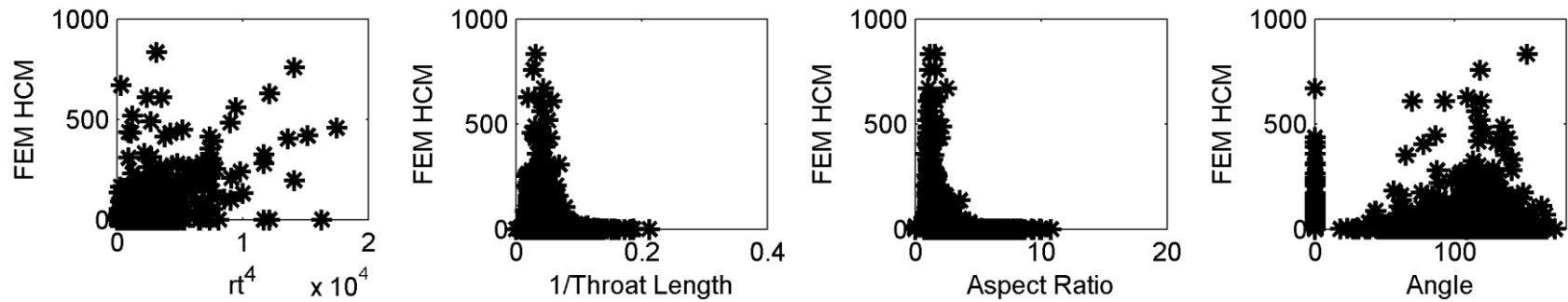
(d)

Figure 6-17: (continued) The scatter plot of throat radius to the fourth power, inverse of throat length, aspect ratio, and angle with FEM_HCM (from left to right) in the random sphere packing at: (c) *Re* = 7.0, (d) *Re* = 11.3.

different Reynolds number shows the similar relationship with network geometric parameters. A linear trend between FEM_HCM and throat radius to the fourth power, and polynomial trend between FEM_HCM and inverse of throat length, exponential trend between FEM_HCM and aspect ratio are shown. We have not yet yielded correlations for a-priori prediction of HCM based on geometric parameters (for inertial flows), but that we remain hopeful that this is something that could be done with additional work.

7.   Conclusions and Future Work

This work is focused on developing pore-scale finite element and network modeling of non-Darcy flow in porous media. The ultimate goal of this research is to predict and fundamentally understand non-Darcy flow behavior in the pore scale.

Chapter 4 compares the macroscopic permeability and microscopic velocity field from pore-scale LBM and FEM simulations (both are rigorous modeling). Chapter 5 implements image-based pore-scale FEM simulations of non-Darcy flow in the segmented image of proppant packing and propped fractures. The stress effects on pore structures, macroscopic properties and microscopic velocity fields are investigated. Chapter 6 develops a network modeling of non-Darcy flow using FEM simulation results.

In this final Chapter, the goal is to summarize the results from each part of the research and provide recommendations for the future research regarding pore-scale finite element modeling and network modeling of non-Darcy flow.

7.1 Conclusions

7.1.1 FEM and LBM Comparison

3D consolidated random sphere packing with image resolutions between 2-10 microns are generated by computer simulation. Different image resolutions results in different pore structures because of the inability of the voxel structure to capture the spherical surfaces exactly. Both LBM and FEM simulations of Stokes flow are performed on the samples. Macroscopic permeability and microscopic velocity fields in the pore space are analyzed and compared.

The change in permeability with image resolution has opposite trends for these two approaches. FEM simulations show an increasing trend in permeability with increasing image resolution while LBM simulations are showing a decreasing trend. LBM simulations using

different relaxation time result in different permeability results. Lower relaxation time results in higher permeability. Both FEM and LBM simulations predict similar permeability value in the highest-image resolution (2 micron) sample. The voxel size effects in LBM simulations are also investigated by dividing the voxel in 10 micron resolution image to 2, 3, 4, and 5 times. Reducing the voxel size decreases the permeability value and helps to reduce the numerical errors associated with voxel size in LBM simulations. When voxel size is divided by 3, 4 or 5 times, LBM simulations predict similar permeability with FEM simulations.

Even though similar permeability are predicted from FEM and LBM simulations, a point-by-point comparison of the microscopic velocity fields is performed to quantify whether differences exist at the pore scale that may be averaged out in the permeability value. Local pore spaces are chosen to plot velocity values from FEM and LBM. Velocity difference is higher at the regions away from the void-solid interfaces. Also FEM calculates higher local velocity than LBM in regions with higher velocity, and shows a wider range of velocity values.

7.1.2 FEM Modeling of Non-Darcy Flow

Image-based pore-scale FEM modeling of non-Darcy flow is applied in segmented microCT image of Berea-proppant-berea and shale-proppant-shale system. Different loading stresses are applied on two systems while imaged.

FEM simulations using two different types of tetrahedral elements P2P1 and P1P1 are compared. The additional velocity nodes in P2P1 elements significantly increase the degree of freedom in the linear system. For the same number of elements, the degree of freedom for P2P1 elements is five times larger and the memory requirement is 8 times larger than P1P1 elements. The permeability predicted from P2P1 elements is around 30% higher compared to P1P1, however the non-Darcy coefficient predicted from P2P1 elements is approximately half of the

value predicted from P1P1 elements. This suggests that the numerical differences associated with element type are more pronounced in the inertial flow regime than for Darcy permeability. As Reynolds number increases, both P2P1 and P1P1 predict a similar value for the onset of non-Darcy flow; however, the convergence limit of P2P1 is significantly lower than P1P1 and increasing mesh refinement will help to increase the convergence limit of P2P1 results.

The stress effects on permeability and non-Darcy coefficient are studied and transport flow behavior is correlated with pore structures. In the Berea system, pore structure exhibits little change from 0 to 4k psi. Embedment of proppants into the rock wall starts to happen at 8k psi. Minor particle crushing occurs at 12k psi and then significant crushing occurs at 20k psi. The permeability remains constant at approximately 225 Darcy from 0 to 8k psi loading. A 12% decline of permeability occurs from 8k to 12k psi and a decline of 60% then occurs from 12k to 20k psi. Not surprisingly, the non-Darcy coefficient shows an opposite trend as permeability. An average value 7.0×10^{-4} is observed from 0 to 8k psi. A small increase (10%) occurred from 8 k to 12k psi and a significant increase (40%) occurred from 12k to 20k psi. The investigation of pore-scale velocity fields indicates that at low Reynolds number, velocity increases through narrower throats because of the dominant viscous forces. As Reynolds number increases, the inertial effects cause fluid flow to exhibit more jet-like behavior, penetrating throats without changing velocity significantly.

In the shale system, loading stress causes the embedment of proppants, thus narrowing or closing the pathways between proppants and the walls and reducing the fracture width. Permeability was reduced by approximately 25% from 4k to 8k psi and 15% from 8k to 12k psi. The reduction of conductivity is more pronounced than permeability.

7.1.3 Network Modeling of Non-Darcy Flow

Rigorous results from pore-scale finite element results of non-Darcy flow are used to evaluate the throat flowrate distribution and pore pressure fields in network models. Hydraulic conductance values for non-Darcy flow are then estimated from the mass conservation governing equation. The non-Darcy network models are validated by using hydraulic conductance values calculated from finite element simulations and comparing the throat flowrate distribution from network modeling versus finite element simulation. The inability for the network and FEM flowrate results to agree can be traced back to the errors in pore-scale mass balances (FEM results). Mesh resolutions effects on mass balances of network pores are discussed. The mass conservation of each pore is an essential prerequisite to obtain a FEM_HCM value that can predict the same flowrate as from finite element simulations. As meshes become coarser, larger errors exist in the mass balance for each pore. The tortuosity of flow path is considered as a way to predict inertial effects in the network models. Two different geometries (straight and tortuous channels) are used to compare inertial flow behavior quantitatively. A new variable (throat angle) is proposed to quantify the tortuous of flow path for each throat in network structure. The network geometric parameters including throat radius, throat length, aspect ratio and throat angle are plotted with hydraulic conductance of non-Darcy flow and a statistical correlation between hydraulic conductance and network geometric parameters is expected to be derived in the future.

7.2 Future Work

7.2.1 Pore-Scale FEM Modeling

The significant computational cost for FEM simulations limits the computational domain size of the problem to solve, especially for P2P1 elements. There are several options to reduce the memory cost of FEM simulations. Solving sparse linear system equations is the most

computational expensive step in FEM simulations. In this work, a direct solver is used to solve the linear system, which requires much more memory than iterative solver. Changing to an iterative solver is an appealing way to reduce the memory cost. Another option is to implement a parallel solver.

7.2.2 Mesh Generation with Local Refinement

Adaptive meshing with local refinement strategies is important for pore-scale simulations of non-Darcy flow in porous media. The void space of porous media usually varies over a large range of pore size distribution. The local mesh refinement option enables the coarse mesh to represent large pore structures and the fine mesh to represent small pore structures. This provides an efficient mesh with different mesh refinement levels in one sample, to accurately represent the complex pore geometry. It also helps to reduce numerical errors in simulations without significantly increasing the computational cost. As the increase of Reynolds number in non-Darcy flow regime, the pore-scale velocity fields show strong inertial effects in some critical regions. Refining the mesh in these regions will present more accurate inertial flow behavior.

7.2.3 Network Modeling of Non-Darcy Flow

Different mesh resolution effects on the mass balance of pores and validity of throat hydraulic conductance from FEM simulations have been compared in cubic packings. The unconsolidated cubic packing has very different pore geometry with the consolidated random sphere packing. In the future, mesh resolutions effects on random packing should be conducted. Network models using FEM_HCM values fails to predict the same flowrate distribution as the original FEM in random packings with 1.6 million elements. Using meshes with higher resolution will help to improve the validity of FEM_HCM values based on our study of mesh resolution effects in cubic packings. It is interesting to investigate whether consolidated pore

structure requires higher mesh resolution to predict the correct hydraulic conductance of non-Darcy flow. Using FEM simulations from P2P1 and P1P1 elements to predict FEM_HCM should be compared. Several different network extraction algorithms from digital images have been developed. In the future, different network structures from different extraction algorithms should be used to compare the validity of hydraulic conductance values.

After obtaining the correct hydraulic conductances for non-Darcy flow, the ultimate goal of this work is to predict the hydraulic conductance using network structure properties. We expect that, in addition to pore and pore-throat geometry, the extent of tortuosity of flow path also brings significant effects on inertial flow behavior. The pore and pore-throat geometry can be quantified by pore inscribed radius, throat inscribed radius, throat length, aspect ratio and etc. Angle has already been used to quantify the tortuosity of flow path for each throat. Statistical analysis needs to be conducted to derive a correlation with non-Darcy hydraulic conductance with these structures parameters.

References

Akanji, L. T., & Matthai, S. K. (2010). Finite element-based characterization of pore-scale geometry and its impact on fluid flow. *Transport in Porous Media, 81*(2), 241-259.

Al-Kharusi, A. S., & Blunt, M. J. (2008). Multiphase flow predictions from carbonate pore space images using extracted network models. *Water resources research, 44*(6).

Alvarez, C., Holditch, S., & McVay, D. (2002). *Effects of Non-Darcy Flow on Pressure Transient Analysis of Hydraulically Fractured Gas Wells.* Paper presented at the SPE Annual Technical Conference and Exhibition.

Arns, C. H., Knackstedt, M. A., Pinczewski, W. V., & Garboczi, E. J. (2002). Computation of linear elastic properties from microtomographic images: Methodology and agreement between theory and experiment. *Geophysics, 67*(5), 1396-1405.

Bakke, S., & Øren, P.-E. (1997). 3-D pore-scale modelling of sandstones and flow simulations in the pore networks. *SPE JOURNAL-RICHARDSON-, 2*, 136-149.

Balhoff, M. T., & Wheeler, M. F. (2009). A predictive pore-scale model for non-Darcy flow in porous media. *SPE Journal, 14*(04), 579-587.

Barree, R., & Conway, M. (2004). *Beyond Beta Factors: A Complete Model for Darcy Forchheimer and Trans-Forchheimer Flow in Porous Media.* Paper presented at the SPE Annual Technical Conference and Exhibition.

Bear, J. (2013). *Dynamics of fluids in porous media*: DoverPublications. com.

Bhattad, P. (2010). *Transient study of the wetting films in porous media using 3D x-ray computed micro-tomography: Effect of imbibition rate and pore geometry.* (Doctor of Philosophy), Louisiana State University, Baton Rouge, LA.

Bhattad, P., Willson, C. S., & Thompson, K. (2010). Segmentation of Low-contrast Three-phase X-ray Computed Tomography Images of Porous Media. *Advances in Computed Tomography for Geomaterials: GeoX 2010*, 254-261.

Bhattad, P., Willson, C. S., & Thompson, K. E. (2011). Effect of network structure on characterization and flow modeling using X-ray micro-tomography images of granular and fibrous porous media. *Transport in Porous Media, 90*(2), 363-391.

Blunt, M., King, M. J., & Scher, H. (1992). Simulation and theory of two-phase flow in porous media. *Physical Review A, 46*(12), 7680.

Borouchaki, H., Hecht, F., Saltel, E., & George, P. (1995). *Reasonably efficient Delaunay based mesh generator in 3 dimensions.* Paper presented at the Proceedings 4th International Meshing Roundtable.

Borujeni, A. T. (2013). *Multi-scale Modeling of Inertial Flows through Propped Fractures*. Ph. D. thesis, Louisiana State University.

Bosl, W. J., Dvorkin, J., & Nur, A. (1998). A study of porosity and permeability using a lattice Boltzmann simulation. *Geophysical Research Letters, 25*(9), 1475-1478.

Brannon, H., Wood, W., & Wheeler, R. (2006, 15-17 February). *Large Scale Laboratory Investigation of the Effects of Proppant and Fracturing Fluid Properties on Transport*. Paper presented at the International Symposium and Exhibition on Formation Damage Control, Lafayette, LA.

Breuer, M., Bernsdorf, J., Zeiser, T., & Durst, F. (2000). Accurate computations of the laminar flow past a square cylinder based on two different methods: lattice-Boltzmann and finite-volume. *International Journal of Heat and Fluid Flow, 21*(2), 186-196.

Bryant, S. L., King, P. R., & Mellor, D. W. (1993). Network model evaluation of permeability and spatial correlation in a real random sphere packing. *Transport in Porous Media, 11*(1), 53-70.

Bryant, S. L., Mellor, D. W., & Cade, C. A. (1993). Physically representative network models of transport in porous media. *AIChE Journal, 39*(3), 387-396.

Chai, Z., Shi, B., Lu, J., & Guo, Z. (2010). Non-Darcy flow in disordered porous media: A lattice Boltzmann study. *Computers & Fluids, 39*(10), 2069-2077.

Chukwudozie, C. (2011). *Pore-scale Lattice Boltzmann simulations of inertial flows in realistic porous media: a first principle analysis of the forchheimer relationship*. Ph. D. thesis, Louisiana State University.

Cipolla, C. (2009). Modeling production and evaluating fracture performance in unconventional gas reservoirs. *Journal of Petroleum Technology, 61*(9), 84-90.

Coker, D. A., Torquato, S., & Dunsmuir, J. H. (1996). Morphology and physical properties of Fontainebleau sandstone via a tomographic analysis. *Journal of Geophysical Research: Solid Earth (1978–2012), 101*(B8), 17497-17506.

Comiti, J., Sabiri, N., & Montillet, A. (2000). Experimental characterization of flow regimes in various porous media—III: limit of Darcy's or creeping flow regime for Newtonian and purely viscous non-Newtonian fluids. *Chemical Engineering Science, 55*(15), 3057-3061.

Cooke, C. (1973). Conductivity of fracture proppants in multiple layers. *Journal of Petroleum Technology, 25*(9), 1101-1107.

Cooper, J., Wang, X., & Mohanty, K. (1999). Non-Darcy-flow studies in anisotropic porous media. *SPE Journal, 4*(04), 334-341.

Costa, U., Andrade, J. J., Makse, H., & Stanley, H. (1999). The role of inertia on fluid flow through disordered porous media. *Physica A: Statistical Mechanics and its Applications, 266*(1), 420-424.

Darcy, H. Les fontaines publiques de la ville de Dijon, 1856. *Dalmont, Paris, 70.*

Dong, H., & Blunt, M. J. (2009). Pore-network extraction from micro-computerized-tomography images. *Physical Review E, 80*(3), 036307.

Du, Q., & Wang, D. (2006). Recent progress in robust and quality Delaunay mesh generation. *Journal of Computational and Applied Mathematics, 195*(1), 8-23.

Ewing, R. P., & Gupta, S. (1993). Percolation and permeability in partially structured networks. *Water resources research, 29*(9), 3179-3188.

Fatt, I. (1956). The network model of porous media 1. Capillary pressure characteristics. *Transactions of the American Institute of Mining and Metallurgical Engineers, 207*(7), 144-159.

Fenwick, D. H., & Blunt, M. J. (1998). Three-dimensional modeling of three phase imbibition and drainage. *Advances in water resources, 21*(2), 121-143.

Flannery, B. P., Deckman, H. W., Roberge, W. G., & D'amico, K. L. (1987). Three-dimensional X-ray microtomography. *Science, 237*(4821), 1439-1444.

Forchheimer, P. (1901). Wasserbewegung durch boden. *Z. Ver. Deutsch. Ing, 45*(1782), 1788.

Fourar, M., Radilla, G., Lenormand, R., & Moyne, C. (2004). On the non-linear behavior of a laminar single-phase flow through two and three-dimensional porous media. *Advances in water resources, 27*(6), 669-677.

Fredd, C., McConnell, S., Boney, C., & England, K. (2001). Experimental study of fracture conductivity for water-fracturing and conventional fracturing applications. *SPE Journal, 6*(3), 288-298.

Friedel, T., & Voigt, H.-D. (2006). Investigation of non-Darcy flow in tight-gas reservoirs with fractured wells. *Journal of Petroleum Science and Engineering, 54*(3), 112-128.

Geller, S., Krafczyk, M., Tölke, J., Turek, S., & Hron, J. (2006). Benchmark computations based on lattice-Boltzmann, finite element and finite volume methods for laminar flows. *Computers & Fluids, 35*(8), 888-897.

Graham, H. L., & Kiel, O. M. (1968). USA Patent No. 3,399,727. U. S. P. Office.

Gresho, P. M., Sani, R. L., & Engelman, M. S. (1998). *Incompressible flow and the finite element method: advection-diffusion and isothermal laminar flow*: Wiley New York.

Guéziec, A. (1996). *Surface simplification inside a tolerance volume*: IBM TJ Watson Research Center.

Guo, Z., & Zhao, T. (2002). Lattice Boltzmann model for incompressible flows through porous media. *Physical Review E, 66*(3), 036304.

Handren, P., Pearson, C., Kullman, J., Coleman, R., Foreman, J., Froebel, K., & Caron, J. (2001). *The Impact of Non-Darcy Flow on Production from Hydraulically Fractured Gas Wells*. Paper presented at the SPE Production and Operations Symposium.

Hart, B., Sayers, C. M., & Jackson, A. (2011). An introduction to this special section: Shales. *The Leading Edge, 30*(3), 272-273.

Hassanizadeh, S. M., & Gray, W. G. (1987). High velocity flow in porous media. *Transport in Porous Media, 2*(6), 521-531.

Hazlett, R. (1995). Simulation of capillary-dominated displacements in microtomographic images of reservoir rocks. *Transport in Porous Media, 20*(1-2), 21-35.

Hill, R. J., Koch, D. L., & Ladd, A. J. (2001). The first effects of fluid inertia on flows in ordered and random arrays of spheres. *Journal of Fluid Mechanics, 448*, 213-241.

Huang, H., & Ayoub, J. A. (2008). Applicability of the Forchheimer equation for non-Darcy flow in porous media. *SPE Journal, 13*(01), 112-122.

Huebner, K. H., Dewhirst, D. L., Smith, D. E., & Byrom, T. G. (2008). *The finite element method for engineers*: John Wiley & Sons.

Irmay, S. (1958). On the theoretical derivation of Darcy and Forchheimer formulas. *Transactions, American Geophysical Union, 39*, 702-707.

Ito, Y., Shih, A. M., & Soni, B. K. (2004). *Reliable Isotropic Tetrahedral Mesh Generation Based on an Advancing Front Method*. Paper presented at the IMR.

Jin, G., Patzek, T. W., & Silin, D. B. (2004). *Direct prediction of the absolute permeability of unconsolidated and consolidated reservoir rock*. Paper presented at the SPE Annual Technical Conference and Exhibition.

Jolls, K., & Hanratty, T. (1966). Transition to turbulence for flow through a dumped bed of spheres. *Chemical Engineering Science, 21*(12), 1185-1190.

Jones, S. (1987). *Using the inertial coefficient B to characterize heterogeneity in reservoir rock*. Paper presented at the SPE Annual Technical Conference and Exhibition.

Kandhai, D., Vidal, D., Hoekstra, A., Hoefsloot, H., Iedema, P., & Sloot, P. (1999). Lattice-Boltzmann and finite element simulations of fluid flow in a SMRX Static Mixer Reactor. *International journal for numerical methods in fluids, 31*(6), 1019-1033.

Kaufman, P., Penny, G., & Paktinat, J. (2008, 16-18 November). *Critical Evaluation of Additives Used in Shale Slickwater Fracs.* Paper presented at the SPE Shale Gas Production Conference, Fort Worth, TX.

Knackstedt, M., Arns, C., Sheppard, A., Senden, T., Sok, R., Cinar, Y., . . . Padhy, G. (2007). *Archie's exponents in complex lithologies derived from 3D digital core analysis.* Paper presented at the 48th Annual Logging Symposium.

Koponen, A., Kataja, M., & Timonen, J. (1996). Tortuous flow in porous media. *Physical Review E, 54*(1), 406-410. doi: 10.1103/PhysRevE.54.406

Koponen, A., Kataja, M., Timonen, J., & Kandhai, D. (1998). Simulations of single-fluid flow in porous media. *International Journal of Modern Physics C, 9*(08), 1505-1521.

Lane, N. M. (2011). *Numerical Studies of Flow in Porous Media Using an Unstructured Approach.* Ph. D. thesis, Louisiana State University.

Langaas, K., & Papatzacos, P. (2001). Numerical investigations of the steady state relative permeability of a simplified porous medium. *Transport in Porous Media, 45*(2), 241-266.

Langtangen, H. P., Mardal, K.-A., & Winther, R. (2002). Numerical methods for incompressible viscous flow. *Advances in water resources, 25*(8), 1125-1146.

Lindquist, W. B., Lee, S. M., Coker, D. A., Jones, K. W., & Spanne, P. (1996). Medial axis analysis of void structure in three-dimensional tomographic images of porous media. *Journal of Geophysical Research: Solid Earth (1978–2012), 101*(B4), 8297-8310.

Lopez-Hernandez, H., Valko, P., & Pham, T. (2004). *Optimum fracture treatment design minimizes the impact of non-Darcy flow effects.* Paper presented at the SPE Annual Technical Conference and Exhibition.

Lopez, X., Valvatne, P. H., & Blunt, M. J. (2003). Predictive network modeling of single-phase non-Newtonian flow in porous media. *Journal of colloid and interface science, 264*(1), 256-265.

Lorensen, W. E., & Cline, H. E. (1987). *Marching cubes: A high resolution 3D surface construction algorithm.* Paper presented at the ACM Siggraph Computer Graphics.

Ma, H., & Ruth, D. (1993). The microscopic analysis of high Forchheimer number flow in porous media. *Transport in Porous Media, 13*(2), 139-160.

Maddison, J., Marshall, D., Pain, C., & Piggott, M. (2011). Accurate representation of geostrophic and hydrostatic balance in unstructured mesh finite element ocean modelling. *Ocean Modelling, 39*(3), 248-261.

Manwart, C., Aaltosalmi, U., Koponen, A., Hilfer, R., & Timonen, J. (2002). Lattice-Boltzmann and finite-difference simulations for the permeability for three-dimensional porous media. *Physical Review E, 66*(1), 016702.

Marcum, D. L., & Weatherill, N. P. (1995). Unstructured grid generation using iterative point insertion and local reconnection. *AIAA journal, 33*(9), 1619-1625.

Marušić-Paloka, E., & Mikelić, A. (2000). The derivation of a nonlinear filtration law including the inertia effects via homogenization. *Nonlinear Analysis: Theory, Methods & Applications, 42*(1), 97-137.

Mei, C., & Auriault, J.-L. (1991). The effect of weak inertia on flow through a porous medium. *Journal of Fluid Mechanics, 222*, 647-663.

Mohan, J., Pope, G., & Sharma, M. (2009). Effect of Non-Darcy Flow on Well Productivity of a Hydraulically Fractured Gas-Condensate Well. *SPE Reservoir Evaluation & Engineering, 12*(4), 576-585.

Much, M., & Penny, G. (1987). *Long-Term Performance of Proppants Under Simulated Reservoir Conditions.* Paper presented at the Low Permeability Reservoirs Symposium.

Newman, M. S., & Yin, X. (2013). Lattice Boltzmann simulation of non-Darcy flow in stochastically generated 2D porous media geometries. *SPE Journal, 18*(01), 12-26.

Oh, W., & Lindquist, B. (1999). Image thresholding by indicator kriging. *Pattern Analysis and Machine Intelligence, IEEE Transactions on, 21*(7), 590-602. doi: 10.1109/34.777370

Okabe, H., & Blunt, M. J. (2004). Prediction of permeability for porous media reconstructed using multiple-point statistics. *Physical Review E, 70*(6), 066135.

Øren, P.-E., & Bakke, S. (2002). Process based reconstruction of sandstones and prediction of transport properties. *Transport in Porous Media, 46*(2-3), 311-343.

Palisch, T., Duenckel, R., Bazan, L., Heidt, J., & Turk, G. (2007). *Determining Realistic Fracture Conductivity and Understanding its Impact on Well Performance-Theory and Field Examples.* Paper presented at the SPE Hydraulic Fracturing Technology Conference.

Pascal, H., & Quillian, R. G. (1980). *Analysis of vertical fracture length and non-Darcy flow coefficient using variable rate tests.* Paper presented at the SPE Annual Technical Conference and Exhibition.

Patzek, T., & Silin, D. (2001). Shape factor and hydraulic conductance in noncircular capillaries: I. One-phase creeping flow. *Journal of colloid and interface science, 236*(2), 295-304.

Ronfard, R., & Rossignac, J. (1996). *Full-range approximation of triangulated polyhedra.* Paper presented at the Computer Graphics Forum.

Rossignac, J., & Borrel, P. (1993). *Multi-resolution 3D approximations for rendering complex scenes*: Springer.

Ruth, D., & Ma, H. (1992). On the derivation of the Forchheimer equation by means of the averaging theorem. *Transport in Porous Media, 7*(3), 255-264.

Scheidegger, A. E. (1958). The physics of flow through porous media. *Soil Science, 86*(6), 355.

Schure, M. R., Maier, R. S., Kroll, D. M., & Ted Davis, H. (2004). Simulation of ordered packed beds in chromatography. *Journal of Chromatography A, 1031*(1), 79-86.

Shewchuk, J. R. (2002). *Constrained Delaunay Tetrahedralizations and Provably Good Boundary Recovery.* Paper presented at the IMR.

Silin, D., & Patzek, T. (2006). Pore space morphology analysis using maximal inscribed spheres. *Physica A: Statistical mechanics and its applications, 371*(2), 336-360.

Sok, R. M., Knackstedt, M. A., Sheppard, A. P., Pinczewski, W., Lindquist, W., Venkatarangan, A., & Paterson, L. (2002). Direct and stochastic generation of network models from tomographic images; effect of topology on residual saturations. *Transport in Porous Media, 46*(2-3), 345-371.

Sok, R. M., Varslot, T., Ghous, A., Latham, S., Sheppard, A. P., & Knackstedt, M. A. (2010). Pore Scale Characterization of Carbonates at Multiple Scales: Integration of Micro-CT, BSEM, FIBSEM. *Petrophysics, 51*(6), 379.

Sondergeld, C., Newsham, K., Comisky, J., Rice, M., & Rai, C. (2010, 23-25 February). *Petrophysical considerations in evaluating and producing shale gas resources.* Paper presented at the SPE Unconventional Gas Conference, Pittsburgh, PA.

Stephen, S., & David, M.-T. (2004). *Investigating How Proppant Packs Change Under Stress.* Paper presented at the SPE Annual Technical Conference and Exhibition.

Succi, S., Foti, E., & Higuera, F. (1989). Three-dimensional flows in complex geometries with the lattice Boltzmann method. *EPL (Europhysics Letters), 10*(5), 433.

Suekane, T., Yokouchi, Y., & Hirai, S. (2003). Inertial flow structures in a simple-packed bed of spheres. *AIChE journal, 49*(1), 10-17.

Sukop, M. C., Huang, H., Lin, C. L., Deo, M. D., Oh, K., & Miller, J. D. (2008). Distribution of multiphase fluids in porous media: Comparison between lattice Boltzmann modeling and micro-x-ray tomography. *Physical Review E, 77*(2), 026710.

Thauvin, F., & Mohanty, K. (1998). Network modeling of non-Darcy flow through porous media. *Transport in Porous Media, 31*(1), 19-37.

Thompson, K. E. (2007). Computing Particle Surface Areas and Contact Areas from Three-Dimensional Tomography Data of Particulate Materials. *Particle & Particle Systems Characterization, 24*(6), 440-452.

Thompson, K. E., & Fogler, H. S. (1997). Modeling flow in disordered packed beds from pore-scale fluid mechanics. *AIChE Journal, 43*(6), 1377-1389.

Thompson, K. E., Willson, C. S., & Zhang, W. (2006). Quantitative computer reconstruction of particulate materials from microtomography images. *Powder Technology, 163*(3), 169-182.

Turner, M., Knüfing, L., Arns, C., Sakellariou, A., Senden, T., Sheppard, A., . . . Knackstedt, M. (2004). Three-dimensional imaging of multiphase flow in porous media. *Physica A: Statistical mechanics and its applications, 339*(1), 166-172.

Umnuayponwiwat, S., Ozkan, E., Pearson, C., & Vincent, M. (2000). *Effect of non-Darcy flow on the interpretation of transient pressure responses of hydraulically fractured wells.* Paper presented at the SPE Annual Technical Conference and Exhibition.

van Batenburg, D., & Milton-Tayler, D. (2005). Discussion of SPE 89325,'Beyond beta factors: a complete model for Darcy, Forchheimer, and Trans-Forchheimer flow in porous media'. *J. Pet. Tech, 57*(8), 72-73.

Vincent, M., Pearson, C., & John, K. (1999). *Non-Darcy and multiphase flow in propped fractures: case studies illustrate the dramatic effect on well productivity.* Paper presented at the SPE Western Regional Meeting.

Wang, Y., Uchida, T., Westferro, F., Rivers, M. L., Nishiyama, N., Gebhardt, J., . . . Sutton, S. R. (2005). High-pressure x-ray tomography microscope: Synchrotron computed microtomography at high pressure and temperature. *Review of scientific instruments, 76*, 073709.

Wardlaw, N., Li, Y., & Forbes, D. (1987). Pore-throat size correlation from capillary pressure curves. *Transport in Porous Media, 2*(6), 597-614.

Warpinski, N., Mayerhofer, M., Vincent, M., Cipolla, C., & Lolon, E. (2008, 10-12 February). *Stimulating unconventional reservoirs: maximizing network growth while optimizing fracture conductivity.* Paper presented at the SPE Unconventional Reservoirs Conference, Keystone, CO.

Wen, Q., Zhang, S., Wang, L., Liu, Y., & Li, X. (2007). The effect of proppant embedment upon the long-term conductivity of fractures. *Journal of Petroleum Science and Engineering, 55*(3), 221-227.

Whitaker, S. (1986). Flow in porous media I: A theoretical derivation of Darcy's law. *Transport in Porous Media, 1*(1), 3-25.

Wu, K., Van Dijke, M. I., Couples, G. D., Jiang, Z., Ma, J., Sorbie, K. S., . . . Zhang, X. (2006). 3D stochastic modelling of heterogeneous porous media–applications to reservoir rocks. *Transport in Porous Media, 65*(3), 443-467.

Wyllie, M., & Spangler, M. (1952). Application of electrical resistivity measurements to problem of fluid flow in porous media. *AAPG Bulletin, 36*(2), 359-403.

Youssef, S., Bauer, D., Bekri, S., Rosenberg, E., & Vizika, O. (2009). *Towards a better understanding of multiphase flow in porous media: 3D in-situ fluid distribution imaging at the pore scale.* Paper presented at the International Symposium of the Society of Core Analysts, Noordwijk, The Netherlands 27–30 September.

Zhan, X., Schwartz, L. M., Toksöz, M. N., Smith, W. C., & Morgan, F. D. (2010). Pore-scale modeling of electrical and fluid transport in Berea sandstone. *Geophysics, 75*(5), F135-F142.

Vita

Yijie Shen was born in Hangzhou, Zhejiang Province, China. After she completed high school in Hangzhou No.2 high school, she went to Zhejiang University of Technology. She graduated with degrees in Bachelor of Science in Biochemical Engineering and second major in International Trade in June 2008. In August 2008, she was accepted as a doctoral candidate by Department of Chemical Engineering in Louisiana State University.